Improving the Structural and Magnetic Properties of Yttrium Iron Garnet

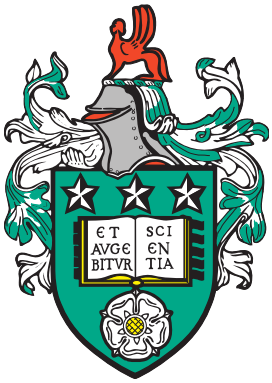

Mohammed Alyami

School of Physics and Astronomy

University of Leeds

Submitted in accordance with the requirements for the degree of

Doctor of Philosophy

May 2021

This thesis is dedicated to my parents, my wife, and my children.

Intellectual Property Statement

The candidate confirms that the work submitted is his own, except where work which has formed part of jointly authored publications has been included. The contribution of the candidate and the other authors to this work has been explicitly indicated below. The candidate confirms that appropriate credit has been given within the thesis where reference has been made to the work of others.

Acknowledgements

I would like to acknowledge the people that have contributed to this work and assisted me during my PhD. This thesis would not have been possible without the support and help out over the course of this project from many people. Firstly, I would like to thank my supervisor Prof B J Hickey for guiding me through my PhD and for his advice and motivation. Also, I would like to give thanks to my co-supervisor Dr Oscar Cespedes for all his help and support, all the academic staff, the experimental officers, post doctoral researchers. I am especially thankful to Dr. Mannan Ali for his continuous advice and for all his help and support during my PhD. I wish also to thank all PhD students for their help and advice during my PhD. Many of them provided advice and assistance and cooperation as well as the training required on all the equipment used to conduct this work. Great appreciation goes to the technical staff including cryogenic team. I am grateful to all the members of the Condensed Matter Group for their help and providing such a great working environment. Particularly thanks to Prince Sattam bin Abdulaziz University that provided the funding for this work. Finally, I am eternally thankful to my parents and my wife for their support and encouragement and for being always by my side.

Abstract

Both gadolinium gallium garnet (GGG) and yttrium aluminium garnet (YAG) substrates are used to grow thin YIG films. It is known that substrates of GGG are associated with reduced lattice strain ($\varepsilon = 0.016\%$) relative to YAG substrates ($\varepsilon = 1.12\%$) for YIG lattices. In addition, it was found that the structural and magnetic properties of thin YIG films are influenced by oxygen contents. For instance, we found in this work that the lattice constant for YIG/GGG films with 6.2% of the Oxygen content is similar to bulk value of YIG lattice constant (12.376 Å) and the magnetic properties are similar to those of bulk YIG that have a coercive field (H_c) < 1 Oe and saturation magnetisation ($M_{s=}143\mathrm{emu/cm^3}$).

The current study concerns all of the features of good quality nm-thin sputtered YIG films with the identification of interfacial diffusion and the impact it has in terms of suppressing magnetisation. The structural and magnetic properties of nm-thin YIG films deposited on GGG and YAG substrates by RF magnetron sputtering. A combination of X-ray diffraction (XRD), X-ray reflectivity (XRR) and atomic force microscopy (AFM) were employed to assess the films' morphology and structural characterisation. Meanwhile, both a VSM and SQUID magnetometer were employed to determine the associated magnetic qualities. The YIG films have a 111 crystalline orientation and a 1-3 Å surface roughness. The YIG films have a coercive field of 0.30 ± 0.05 Oe, saturation magnetisation of 140 ± 6 emu/cc. Furthermore, the saturation magnetic moment's thickness dependence has a dead layer. The dead layer thickness can be changed by changing the Oxygen contents during sputtering. The thinnest dead layer was 2.35nm in YIG film with 6.2% of Oxygen and the thickest dead layer was 6 nm in YIG film with 5% of Oxygen.

When a normal metal (NM) makes contact with a magnetic material, this can result in spin Hall magnetoresistance (SHMR). Insulating magnetic materials help to avoid magnetic effects because they are able to effectively restrict electrons from leaving the NM. To help analyse this, an

innovative means of producing YIG has been devised that utilises sputtering methods, thereby enabling applications to be created in less time and at lower cost relative to the liquid phase epitaxy (LPE) approach. The magnetic qualities of the YIG material have been specified at varying thicknesses. For thin samples, it is known that magnetisation is lower than the bulk value and this is understood to be attributable to the substrate interface having a layer that is interdiffused. Owing to the fact that the SHMR is an interface effect, it is necessary to employ AFM and XRR to examine how rough the films are.

The first measurements of SHMR were made using platinum and the results achieved broadly matched those reported in the empirical literature. A cryostat is used to measure angular dependence with four probe resistance measures and a split pair magnet which enables the sample to be positioned in all conceivable directions relative to the applied field. This concurs with the established theory and research was conducted across various temperatures from 2K to 300K. A range of models were then applied to fit the data for the spin diffusion length and it was found that the temperature dependence is best explained by the Elliot-Yafet mechanism (EY). The research is conducted into magneto-transport with bilayers of platinum and YIG using different interfaces (2 nm of Pt on 40 nm of YIG with different Oxygen contents) . Measuring resistivity as a function of temperature, conventional magnetoresistance and angle-dependent magnetoresistance reveals that there is considerable reliance on the interface. Consequently, it is necessary to develop the methods for preparing interfaces so as to observe a pure SHMR from enhanced spin mixing conductance.

Abbreviations

AC	Alternating Current	DC	Direct Current
MR	Magnetoresistance	AMR	Anisotropic Magnetoresistance
DP	D'yakonov-Perel	EY	Energy Dispersive X-ray Spectroscopy
EY	Elliot-Yafet	FIB	Focused Ion Beam
FM	Ferromagnet	FMR	Ferromagnetic Resonance
FWHM	Full Width Half Maximum	GGG	Gadolinium Gallium Garnet
HAADF	High Angle Annular Dark Field	IPA	Isopropyl Alcohol
WL	Weak localisation	LPE	Liquid Phase Epitaxy
MOKE	Magneto-optical Kerr Effect	AFM	Atomic Force Microscopy
NM	Normal Metal	PLD	Pulsed Laser Deposition
RF	Radio Frequency	RMS	Root Mean Square
SHE	Spin Hall Effect	ISHE	Inverse Spin Hall Effect
SHMR	Spin Hall Magnetoresistance	SQUID	Superconducting Quantum Interference Device
SSE	Spin Seebeck Effect	STEM	Scanning Transmission Electron Microcopy
TEM	Transmission Electron Microscopy	UHV	Ultra High Vacuum
VSM	Vibrating Sample Magnetometer	VTI	Variable Temperature Insert
XRD	X-ray Diffraction	XRR	X-ray reflectivity
YAG	Yttrium Aluminium Garnet	YIG	Yttrium Iron Garnet

Common Symbols

B	Applied Magnetic Field ($\mu_0 H$)
M	Magnetisation
G	Spin Mixing Conductance
λ	Spin Diffusion Length
D	Diffusion Constant
d	Thickness
θ_{sh}	Spin Hall Angle
e	Elementary Charge
m_e	Electron Mass
h	Planck's Constant
$\hbar$	$h/2\pi$
ρ	Resistivity
σ	Conductivity
T	Temperature
j_e	Charge Current
j_s	Spin Current
τ_{sf}	Spin Relaxation Time
τ_p	Momentum Relaxation Time

CONTENTS

CHAPTER 1

Introduction

Magnetic oxides offer useful magnetic properties and structural qualities that make them particularly well-suited for a range of electronic applications including in telecommunications, radar and microwave appliances [1]. There are three types of magnetic oxides: garnets, spinels and hexaferrites. What distinguishes each of these is their crystal structure and this feature enables large numbers of cations to be accommodated across various sites [2; 3].

Yttrium iron garnet (YIG) was discovered in 1956 by Geller and Gilleo [4] and because it serves as a ferrimagnetic insulator, it is regarded as the oxide with the largest number of practical applications [3]. In addition, relative to the other oxides, YIG offers excellent chemical stability, a high Curie temperature and minimal magnetic damping. The spin waves persist in YIG owing to its excellent crystal properties, the absence of carriers and minimal magneto-crystalline anisotropy [5]. Consequently, YIG is well-suited to propagating spin waves [6] which result from the disorder associated with local magnetic ordering. These spin waves were initially identified in 1929 by Bloch [7] and are associated with the spin excitations that occur in magnetic materials [8]. A practical application of these spin waves is in computers where they serve as potential data carriers with a wavelength of below 1m, thereby offering a low frequency. This low frequency is important because it enables spin information to be transferred across greater distances (macroscopic) [9]. It is the manner in which spin coupling interact that determines the features of spin waves; for instance, the interaction can be a weak long-range dipole-dipole or it could be a strong short-range exchange interaction [8]. Spin waves are required in various appliances that use microwave signals (e.g. circulators) [10]. YIG film insulators measuring just a nanometre in thickness are employed in magnonics and spintronics [11; 12].

The purpose of spintronics is to either generate or influence spin currents to serve a purpose in practical applications. Moreover, spintronics concerns the study of how solid state and electron spin environments interact with the resulting knowledge being used to create innovative devices. Research in this area has been responsible for technological advances in terms of the rate and performance of data processing; data storage; and energy efficient dissipation. This experimental research will therefore contribute to the existing body of knowledge regarding spintronics.

Mott was a pioneer of spin polarised transport, establishing a knowledge base by providing explanations for the unusual way in which the electrical resistance of ferromagnetic materials behaves and it is this that gives rise to magneto-resistive effects [13; 14]. During the late-1980s, Fert [15] and Grünberg [16] discovered a previously unobserved phenomenon referred to as giant magnetoresistance (GMR) in epitaxial Fe | Cr multilayers. Subsequent research confirmed that GMR could also be observed in alternative multilayer structures that are suitable for application in non-volatile memory applications [17; 18]. The first commercial magnetic sensor making use of GMR was made available during 1994 [19] and this was followed by IBM creating magnetic hard disks that incorporated GMR read heads [20]. Tunnel magnetoresistance (TMR) superseded GMR in the early 2000s [21; 22] and magnetic tunnel junctions (MTJ) comprised the base element in a wide range of magnetic random-access memory (MRAM) appliances.

MTJs with a crystalline MgO tunnel barrier are required to achieve a high TMR (200%). Whilst working separately, Berger and Slonczewski both proposed the spin transfer torque effect during 1996 whereby a spin-polarised current transfers angular momentum to a ferromagnet and influences the direction of its magnetisation in the absence of a magnetic field [23; 24]. A notable advance in spintronics was the realisation of non-volatile MRAM for magnetic hard disks [25; 26]. Spin transfer torque-based magnetisation switching [23; 24; 27] and magnetic domain wall racetrack memory [28] offer alternative opportunities for the scaling of MRAM.

Datta and Das developed a model for electron spin-based field effect transistor (SFET) during 1990 in which the spins are controlled by the gate electrode's electric field [29]. The ferromagnets in a SFET are the source and drain and these serve as the injector and detector for electronic spins. The SFET has been demonstrated experimentally [30; 31] but not in ambient conditions. If this could be fully realised, it could afford considerable practical benefits in fast programmable logic appliances and could eradicate the time lag associated with data processing. Moreover, it is possible that it could one day supplant electron charge-based conventional electronics. Conventional spintronics offer a range of benefits but it is limited in the sense that the transfer and

processing of information requires electrons to be transferred. In contrast, magnon spintronics utilises spin waves to transfer and process information, thereby offering an alternative approach [32–36]. Magnons are magnetic moments' collective excitations in materials that are magnetically ordered. It is possible for magnons to propagate over a distance of several centimetres [33]. Information is transferred by means of spin angular momentum and this is advantageous because there is not a flow of charge current, thereby avoiding Joule heating dissipation. The microwave method is arguably the classic form of magnon excitation and it continues to offer an effective means of managing the wavelength, phase and frequency of injected magnons. Alternative means of excitation include spin waves being parametrically amplified from thermal fluctuations [37]; femtosecond laser methods whereby the magnetic system becomes excited by a very short laser pulse [38]; and spin-transfer-torque-based (STT-based) magnon injection [39–41]. Magnons provide the potential for innovative wave-based computing technologies to be devised. Moreover, by the geometry of magnetic structures and proper selection of magnetic material, it is possible to achieve magnon properties on a large scale. Essentially, this opens up opportunities to produce magnetic insulators for highly energy-efficient applications. Insulator-based devices require converters that are highly efficient to be able to convert charge current into spin currents and spin currents into charge currents. It is the exchange interaction concerning insulator electrons and conduction electron spins that produces the spin current transfer in the ferromagnetic insulator/metal bilayers.

The generation and transfer of spin-polarized current to the normal metal layer from the ferromagnetic layer, this is referred to as the spin pumping effect [42; 43]. It is possible to switch the spin current to become a charge current in normal metal by means of the inverse spin Hall effect (ISHE) [44; 45]. The spin Hall effect (SHE) has the ability to transform a direct current in the paramagnetic layer into a spin current in heterostructures [44; 46]. This spin current could then excite the ferromagnetic layer's magnetisation dynamics by means of spin transfer torque (STT), thereby resulting in spin waves. It was during 2010 that Kajiwara et al. became the first to confirm the full cycle of conversion process whereby a charge current in normal metal is converted to achieve pure spin current before returning to a charge current in the magnetic insulator/normal metal (YIG/Pt) bilayer [47]. During the same year, Slonczewski suggested

the notion of using the thermal transport of magnons to produce STT [48]. Subsequently, there has been considerable interest in researching STT and spin pumping in relation to the magnetisation dynamics in YIG/Pt bilayer structures. In 2010, Uchida et al. demonstrated the presence of the spin Seebeck effect (SSE) in magnetic insulators including $Y_3Fe_5O_{12}$ and $LaY_2Fe_5O_{12}$(La: YIG) [49]. This is a promising area of research that could potentially yield innovations in thermoelectric generation that could result in new energy saving technologies.

Considerable efforts have been made by researchers to improve our understanding of YIG as a means of producing efficient insulator-based magnetic devices based on spin currents. YIG offers a high Curie temperature, low damping ($\alpha \approx 3 \times 10^{-5}$) [50], excellent chemical stability [51], good synthesis of single crystalline material, and effective electrical insulation (band gap = 2.85 eV) [52]. In terms of its insulation qualities, YIG experiences no parasitic heating effects as a result of conduction electrons. YIG is utilised in a wide range of microwave appliances including delay lines, microwave filters and magneto-optical equipment and, for this reason, it has been the subject of considerable research efforts. Recently, YIG has proven influential in various areas of innovation including spin transfer torque, spin pumping, thermally driven spin caloritronics, and spin Hall magnetoresistance [53–60]. Meanwhile, theoretical research has been conducted into a spin torque transistor comprising two lateral thin-film spin valves linked by YIG via STT [61].

Research into magnonics and oxide spintronics has generated a demand for exceptionally thin YIG films of just a nanometre in thickness and offering good crystalline quality along with minimal Gilbert damping. Various methods have been used to grow YIG with the best quality being achieved when employing Liquid Phase Epitaxy (LPE) [62–64], albeit that these films are relatively thick (measured in microns). Several studies have indicated that pulsed laser deposition (PLD) [6; 65–69] and laser molecular beam epitaxy [70; 71] can be employed to produce nanometre-thick films of YIG. However, it is Hauser et al. who have achieved the best results in terms of PLD samples with damping of just 7×10^{-5} when using a film 20 nm thick [72]. In addition, researchers have devoted considerable efforts investigating RF sputtering followed by

post-growth annealing [73–75] or in situ annealing [60; 76]. Research has also confirmed that materials offering good crystalline qualities as well as acceptable magnetic qualities in ambient conditions can be achieved using off-axis sputtering [58; 74]. Spin Hall magnetoresistance (SHMR) was reported in 2012 and it is recent addition to the known spin based effects [77]. The SHMR has been confirmed showing the effect in platinum but there was argument about how to fit the experimental data to prove the theory [78–83].

In this thesis, we have done detailed investigation of the structural and magnetic properties of YIG films sputtered by RF for a better understanding of its properties and optimisation. We have improved the YIG properties by changing the oxygen content during sputtering. Also, in this thesis the work presented has been undertaken to understand more about SHMR phenomenon and modelling the fundamental parameters of spin transport in the materials.

1.1 Thesis structure

Chapter Two presents an introduction to spintronics and its underlying principles with reference to the progress that has been made in this area in the empirical literature. Not only does this give background information regarding the contribution of the current study but it also provides details of the science that has effectively shaped the current research. Several spin transport effects will be reviewed along with the processes by which they can be measured. Particular emphasis is placed on spin Hall magnetoresistance and there is a discussion of the theoretical model that can be used to explain it. From the empirical literature emerges a model against which the experimental results can be tested. YIG is at the centre of this study and explanations are offered for why this is so. In addition, the qualities of YIG are discussed, as are the methods used in its deposition.

Chapter Three provides details of the experimental methods employed, including the set-up applied. This includes details of the sample deposition, the ferromagnetic resonance methods, as well as the structural and magnetic characterisation. The chapter starts by discussing how RF magnetron sputtering is used for the deposition of the

YIG samples. Subsequently, details are provided of the annealing conditions required to produce a single crystal YIG that has a 1-3Å surface roughness. It is described how DC sputtering will be used to deposit Pt, as well as how the crystallinity and structural qualities of YIG are examined by means of x-ray diffraction and x-ray reflectivity. Atomic force microscopy (AFM) is applied to analyse the film's morphology. Meanwhile, a vibrating sample magnetometer (VSM) as well as a superconducting quantum interference device (SQUID) VSM are used to examine the magnetic qualities. Descriptions are then offered of the SHMR measuring methods that utilise cryogenic and magnetic equipment to investigate metals' spin transport qualities across a wide temperature range.

Chapter Four provides a detailed account of the tests conducted to establish YIG's features and qualities. Full details are provided of the data used to establish the optimal conditions for creating the material with the preferred features. Comparisons will be made with the results in the empirical literature to help demonstrate how successful the new sputtering method is. Furthermore, this chapter systematically investigates the nanometre-thick films of YIG produced using on-axis sputtering with magnetic and structural characterisation. The interfacial source of YIG film magnetisation reduction is explored and it is these outcomes that provide details of YIG's structural properties. From this it is apparent that the interface of YIG and GGG has an interdiffusion. Particular attention is paid to the magnetic qualities and especially the magnetic information at the interface that has improved in this work compares to the previously results.

Chapter Five provides details of the SHMR results, paying particular attention to the efforts made concerning the platinum wires used to study the effect. It is demonstrated how the angular rotations tally with the theory and details are provided for temperature dependence. Platinum's additional transport properties are described, emphasising how resistivity is affected by different oxygen contents in YIG films. Details are provided for YIG films of varying oxygen content with a description of how the experiments changed over time to achieve the anticipated size of the effect by improving the method for preparing the sample. The data are subsequently fitted with the existing theory based on various assumptions to arrive at conclusions. In addition, the problems encountered and the factors that influenced the measuring process are described.

Finally, Chapter Six concludes by drawing together the research findings from the various aspects of the investigation. These conclusions are then compared to those in the empirical literature and subjected to a critical discussion. It is explained why the results remain open to a degree of interpretation and suggestions are made to advise researchers conducting similar work in future. It is apparent that there is a need for further research into the YIG surface quality which could yield a better appreciation of the SHMR effect and the practical applications for which it could be deployed.

CHAPTER 2

Background

2.1 Introduction

The qualities of various magnetic materials are utilised for a range of purposes including microwave technology, medical equipment, data storage, transport and generating electricity [84; 85]. The theoretical underpinnings are discussed in this chapter along with the importance of interface effects. The first section offers a description of yttrium iron garnet's magnetic qualities and crystal structure. This is followed by consideration of the principles associated with the associated magnetisation features and spin Hall effect, the method for identifying spin currents, and the inverse spin Hall effect. Finally, the chapter rounds off by addressing the spin Hall magnetoresistance and magnetoresistance in thin films.

2.2 YIG's magnetic properties and crystal structure

Bertaut and Forrat discovered the ferrimagnetic insulator YIG ($Y_3Fe_5O_{12}$) during 1956 [4; 86] and Kittel referred to it as the fruit fly of magnetism [87]. YIG has a complex crystal structure, a definite composition and almost perfect cubic symmetry with a density of $5.17\mathrm{g/cm}^3$ [88] and magnetisation damping of just $\alpha \approx 3 \times 10^{-5}$ [89]. Furthermore, YIG's Curie temperature is approximately 560K and its band gap is 2.85eV [88].

The lattice constant of the YIG unit cell is 12.376 ± 0.004 Å and its most likely space group is $O_h^{10} - Ia3d$ [4]. As can be seen in the figure below, YIG's unit cell's cubic structure comprises 160 ions and 8 chemical formula units of $\mathrm{Y_3Fe_5O_{12}}$. Each individual YIG formula unit comprises 3 dodecahedral (c site), 2 octahedral (a site) and 3 tetrahedral sites (d site) comprising 24 Y^{3+}, 40 Fe^{3+} ions and 96 O^{2-} ions. The Y^{3+} ions are located at the dodecahedral (c) sites with each of these sites having 8 O^{2-} ions which create a 12-sided polyhedron with 8 corners. 24 Fe^{3+} are found at tetrahedral (d) sites with 4 O^{2-} ions to achieve tetrahedral symmetry. It is at the octahedral (a) sites that the 16 Fe^{3+} are found and these are encircled by 6 O^{2-} ions to achieve octahedral symmetry. Meanwhile, it is on the h sites that the O^{2-} ions are found with a single ion at the junction between 1 tetrahedron, 1 octahedron and 2 polyhedrons. As such, every O^{2-} ion is encircled by 1 a site Fe^{3+} ion, 1 d site Fe^{3+} ion and 2 c site Y^{3+} ions.

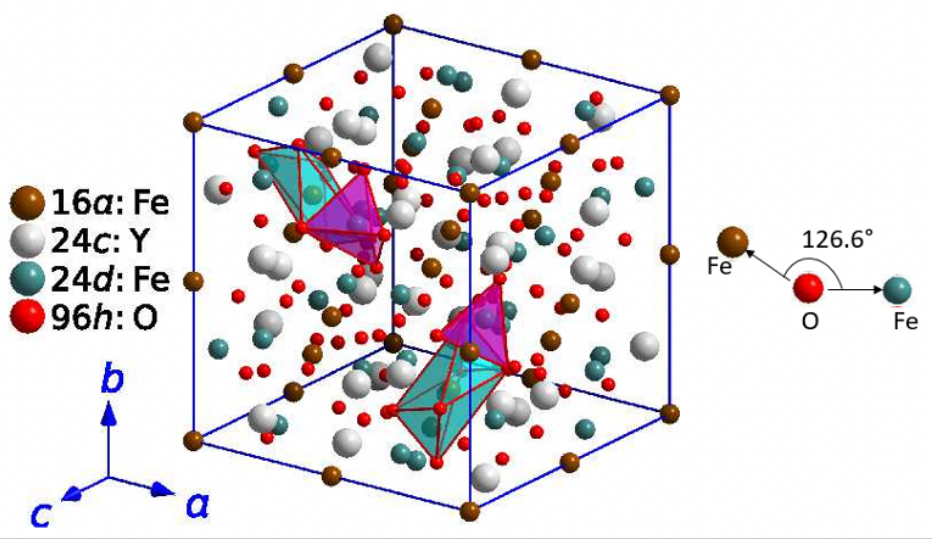

Figure 2.1: YIG crystal structure [90]. YIG derives its magnetisation from the 16 Fe^{3+} ions on a sites and 24 Fe^{3+} ions at d sites experiencing super-exchange interactions.

Y^{3+} ions are diamagnetic owing to the fact that they exhibit a closed shell electronic configuration $\left([\mathrm{Kr}]4\ \mathrm{d}^0 5\ \mathrm{s}^0\right)$. YIG derives its magnetisation from the 16 Fe^{3+} ions on a sites and 24 Fe^{3+} ions at d sites experiencing super-exchange interactions. There are substantial distances separating the tetrahedral and octahedral sites from the common oxygen ion of 2 Å and 1.88 Å super-exchange interactions. As a result of this engagement, the a site Fe^{3+} ions' and the d site Fe^{3+} ions' magnetic moments experience antiparallel alignment. It is because the Fe^{3+} ions each have a five Bohr magneton $(5\mu_B)$ that the YIG exhibits spontaneous magnetisation. Because d sites have 3 Fe^{3+} ions for every 2 Fe^{3+} ions at a sites, at $\mathrm{T} = 0\ \mathrm{K}$ there will be a magnetic moment per formula unit of $5 \times 3(d \text{ site }) - 5 \times 2(a \text{ site }) = 5\mu_B$. This closely reflects the value of 4.96 μ_B that was recorded when conducting an experiment [91]. YIG has cubic magneto-crystalline anisotropy and an easy axis in the (111) direction. At room temperature, the first-order cubic anisotropy constant is $K_1 = -6000\mathrm{erg/cc}$ and the second-order cubic anisotropy constant is $K_2 = -260\mathrm{erg/cc}$ [88]. Furthermore, saturation magnetisation at room temperature is $M_s = 140\mathrm{emu/cc}(298\ \mathrm{K})$, whilst Ms at $\mathrm{T} = 0\ \mathrm{K}$ is196 emu/cc [88]. A film of (111) YIG offers an out-of-plane effective anisotropy field $(2K_1/M_s)$ of approximately 85 Oe as well as a threefold in-plane

effective anisotropy field below 85 Oe. These are smaller fields than the external magnetic fields typically employed when conducting experimental research.

It is only the ferric ions that are magnetic in YIG and the ferric ions have a state of L = 0 with spherical charge distribution. Consequently, they have only weak engagement with lattice deformation and phonons and this means that YIG has particularly narrow linewidths when conducting experiments into ferro-magnetic resonance (FMR). Intrinsic damping in YIG crystals results in a FMR linewidth of approximately 0.2 Oe at 10 GHz [89]. At this linewidth, the intrinsic Gilbert damping constant (α) is approximately 3×10^{-5} and this is approximately two orders of magnitude lower than is associated with ferromagnetic metals [92]. Whereas permalloy has a magnon lifetime of just a few nanoseconds, the fact that YIG has the narrowest FMR linewidth means that its magnon lifetime extends to several hundred nanoseconds. YIG also experiences limited damping and this means that it is possible to propagate spin currents across distances of several centimetres [33]. It is for this reason that YIG is the preferred material when researching spin waves or magnetic insulator-based spintronics.

It is typically the case that thin YIG films will be grown on substrates of (111) gadolinium gallium garnet (GGG). GGG's cubic crystalline structure has 8 formula units to each unit cell and the lattice constant is 12.383 Å. In addition, they have a similar thermal expansion coefficient of $1.04 \times 10^{-5}/^{\circ}\mathrm{C}$ which enables nanometre-thick YIG films to grow epitaxially on substrates of GGG.

2.3 Electrical conductivity

When a conductor is subjected to an electric field, the result is a flow of charge current that is governed by electron mobility. Electron mobility experiences scattering events resulting from a range of sources. When temperatures are held down, a metal's impurities and defects are responsible for the majority of the resistivity. This is because impurities and defects are responsible for scattering events as well as residual resistivity whereby at 0K there is finite resistivity. In practical terms, these are additional sources of scattering events which have the effect of diminishing the electrons' mean free path. The Bloch-Grueneisen formula in equation 2.1 can be used for the resistivity of a NM:

$$\rho(T) = \rho(0) + \rho_{el-ph}(T) \tag{2.1}$$

Reducing a material's spatial dimensions has the result of shortening the electrons' mean free path. The Fuchs-Sondheimer relation is used to model this and is presented in equation 2.2 [93]:

$$\frac{\rho}{\rho_0} = 1 + \frac{3}{8}\frac{l_0}{d}(1-p) \tag{2.2}$$

where, ρ_0 represents bulk resistivity, l_0 is the bulk mean free path of the electrons, d is the thickness of the film and p is a specularity parameter which models the way in which electrons scatter from the surface.

2.4 Spin currents and spin diffusion

As a result of spin of the electron, there is an internal angular momentum associated with each electron. Spin current is the term used to refer to the flow of spin and this behaves much like the flow of charge associated with electrical currents. Conservation law is used as the basis for defining a charge current. Meanwhile, the charge current density $(\mathbf{j_c})$ is defined using the continuity equation of charge [94; 95]:

$$\dot{\rho_q} = -\nabla \cdot \mathbf{j_c} \tag{2.3}$$

It is possible to inject a spin current into a normal metal (NM) from a ferromagnet (FM) if there is a bi-layer structure of ferromagnet and normal metal. Figure 2.2 illustrates a spin current in a junction of FM and NM where a charge current crosses the interface. In a scenario where there is a diffusion or a drift spin current, the force is the gradient derived from the discrepancy between the spin dependent electrochemical potential associated with spin down $(\mu_\downarrow)$ and spin up $(\mu_\uparrow)$. In this scenario, it is possible to depict the spin current density $\mathbf{j_s}$ and the charge current density $\mathbf{j_c}$ as follows [96; 97]:

$$\mathbf{j_c} = j_\uparrow + j_\downarrow = \frac{1}{e}\nabla(\sigma_\uparrow\mu_\uparrow + \sigma_\downarrow\mu_\downarrow) \tag{2.4}$$

$$\mathbf{j_s} = j_\uparrow - j_\downarrow = \frac{1}{e}\nabla(\sigma_\uparrow\mu_\uparrow - \sigma_\downarrow\mu_\downarrow) \tag{2.5}$$

whereby $(\sigma_\uparrow)$ depicts spin up conductivity and $(\sigma_\downarrow)$ represents spin down conductivity, respectively.

The following are the continuity equations for steady state charge and spin:

$$\nabla.(j_\uparrow + j_\downarrow) = 0 \tag{2.6}$$

$$\boldsymbol{\nabla} \cdot (\mathbf{j}_\uparrow - \mathbf{j}_\downarrow) = -e\frac{\delta n_\uparrow}{\tau_{\uparrow\downarrow}} + e\frac{\delta n_\downarrow}{\tau_{\downarrow\uparrow}} \tag{2.7}$$

whereby $\delta\mathbf{n}\uparrow(\downarrow)$ signifies spin up (down) deviation from carrier density equilibrium; $(\tau_{\uparrow\downarrow})$ represents an electron's scattering time either from spin state up to spin state down or from spin state down to spin state up. Applying the balance principle

and continuity equations $\frac{N\uparrow}{\tau_{\uparrow\downarrow}} = \frac{N\downarrow}{\tau_{\uparrow\downarrow}}$and this confirms that there is an absence of net spin scattering in equilibrium. The fundamental equations used when describing charge and spin transport are as follows [96; 97]:

$$\nabla^2(\sigma_\uparrow\mu_\uparrow + \sigma_\downarrow\mu_\downarrow) = 0 \tag{2.8}$$

$$\nabla^2(\mu_\uparrow - \mu_\downarrow) = \frac{1}{\lambda_{sd}^2}(\mu_\uparrow - \mu_\downarrow) \tag{2.9}$$

In the spin diffusion equation 2.9, $\lambda_{sd} = \sqrt{D\tau_{sf}}$ signifies the length of the spin diffusion, D represents the spin-averaged diffusion constant, whilst τ_{sf} denotes the spin relaxation time.

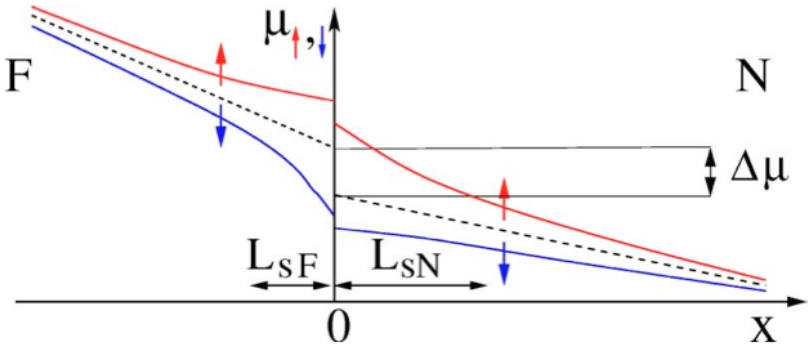

Figure 2.2: This figure represents a ferromagnet/normal metal (FM/NM) junction and illustrates the spin dependent electrochemical potentials' spatial variation across a current-carrying interface. The L_{sF} and L_{sN} in spin diffusion lengths characterise spin accumulation decay when not at the interface, where L_{sF} refers to the FM region and L_{sN} in refers to the NM region. [98].

At junctions of FM and NM, when the NM experiences a spin polarised current passing into it, there is a short-range disparity in the spin up and spin down chemical potentials and the result is that NM experiences spin accumulation. The electrical conductivity of metals that are not magnetic is not dependent on spin and there is no spin polarisation associated with the charge current. Therefore, the spin accumulation disappears by spin flip scattering over a distance called the spin diffusion length.

2.5 Spin relaxation mechanisms

An electron's spin experiences relaxation along a timeframe of τ_{sf}. In this timeframe, the distance travelled the electron is referred to as the diffusion length λ. The ability to gauge the length scale is important because it is a factor that effectively constrains the practical application of spintronic appliances.

Meanwhile, the following equation demonstrates that the diffusion constant (D) and momentum scattering time (τ_p) are related [98]:

$$D \propto \tau_p \tag{2.10}$$

Equation 2.11 shows how the product of the spin diffusion time and the diffusion constant gives the spin diffusion length:

$$\lambda = \sqrt{D\tau_{sf}} \tag{2.11}$$

It is the way in which the spin relaxation time responds to the momentum scattering time that governs the behaviour of the spin diffusion length. Numerous mechanisms have been advocated with regards to this and these are discussed below.

2.5.1 Elliot-Yafet

It was Elliot [99] in 1954 who was the first to suggest that momentum scattering was responsible for the relaxation of conduction electron spins via the spin-orbit interaction. Yafet amended this by making allowance for phonons, thereby resulting in the Elliot-Yafet mechanism [100]. We may write

$$\frac{1}{\tau_{sf}} = \frac{\eta}{\tau_p} \tag{2.12}$$

Where η is the probability of a spin-flip event occurring during electron - phonon scattering.

$$D = 1/3 v_F l = 1/3 v_F^2 \tau_p \tag{2.13}$$

Where l is the mfp :

$$\lambda = \sqrt{\frac{1}{3} v_F^2 \tau_p^2 \tau_{sf}} = \sqrt{\frac{1}{3} v_f^2 \tau_p^2 / \eta} = v_F \tau_p \sqrt{1/3\eta} \tag{2.14}$$

Since $\rho \propto \frac{1}{\tau_p}$ and ρ approximately linear in T above the T^5 region we have

$$\lambda \propto \frac{1}{T} \tag{2.15}$$

Which we will use in the theory of the spin Hall magnetoresistance (SHMR).

2.6 Spin wave current

It is possible for spin waves to transport spin currents in a process that entails spins in close proximity to each other coupling and dissipating angular momentum. When the materials involved are magnetic, the spin on electrons that are close by move in the same direction as a result of exchange interaction, this can be represented by the Heisenberg Hamiltonian:

$$E_i = -2J \sum_j \mathbf{s_i} \cdot \mathbf{s_j} \tag{2.16}$$

In Equation2.16, J is the exchange integral that results from the overlap of the electrons' wave function. The spins may be either ferromagnetic or anti-ferromagnetic and this is determined by the exchange integral's sign.

Each dipole's magnetic moment is exposed to a torque which attempts to ensure it becomes aligned to the direction of the field being applied. Having established a magnetic moment, the angular momentum of the dipole results in a situation whereby the torque acts upon the moment, causing it to precess in the same direction as the field being applied, in much the same way as gravity affects an object when it is spinning. Equation2.17 is the Landau-Lifschitz equation and refers to the relationship between the magnetisation vector's time derivative, the gyromagnetic ratio (γ) and the field being applied (H)..

$$\frac{d\mathbf{M}}{dt} = \gamma \mathbf{M} \times \mathbf{H} \tag{2.17}$$

Multiplying the applied field and the gyromagnetic ratio gives the precession's angular frequency. The moment of the dipole experiences damping and, consequently, it relaxes to achieve a low-energy parallel to the field being applied. This occurs because of interactions with lattice vibrations and environmental degrees of freedom which causes angular momentum to be transferred. Incorporating the Gilbert term into Equation2.17 produces the Landau-Lifschitz-Gilbert equation, thereby accounting for the relaxation (see Equation2.18):

$$\frac{d\mathbf{M}}{dt} = -\gamma \mathbf{M} \times \mathbf{H} + \frac{\alpha}{M_s} \mathbf{M} \times \frac{d\mathbf{M}}{dt} \tag{2.18}$$

Where α represents the parameter of Gilbert damping. This is especially low for YIG ($< 10^{-4}$), thereby enabling the long-distance transport of spin waves (>1mm) [101; 102]. In magnetic materials, the different spins are coupled as a result of exchange interaction. As such, if one spin is disturbed, the result is a wave that affects the surrounding spins, creating movement similar to that of a spring. This may be triggered by thermal energy or alternatively by microwaves being absorbed in FMR. With

regard to the exchange spin current, the electrons experience successive excitations and this results in a spin wave with angular momentum (see Figure2.3 [47].

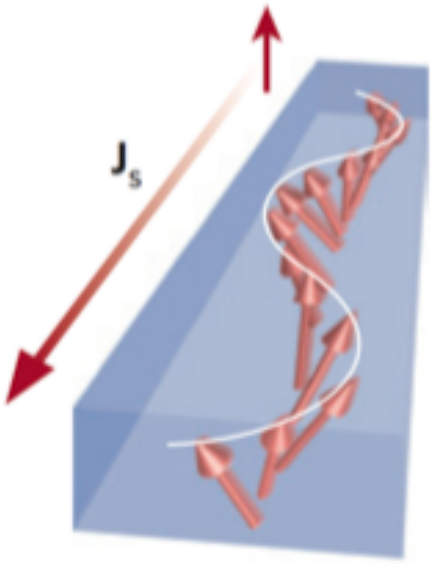

Figure 2.3: Depiction of a spin wave in which exchange coupled spins undergo propagation. The image represents the spin currents that occur in magnetic insulators [47].

Magnons are spins waves that are thermally derived. Moreover, magnons are able to explain the loss of a material's saturation magnetisation at finite temperatures when the magnetic order experiences disruption. It is possible for a spin current to be injected into metal by means of such spin waves using the process of spin pumping. This is still possible if the magnetic material has insulating properties (e.g. YIG). In spintronics, spin pumping effectively does the job performed by batteries in standard electronics. The spin wave has angular momentum and this wave passes over to a NM in which spin transfer torque brings about spin accumulation. The accumulation then experiences spin relaxation. There is a need for spin pumping conductance $A_{\uparrow\downarrow}$ to be applied in order to introduce a spin current across a FM/NM interface in this way. The conductance is effectively the discrepancy between the spin mixing conductance

transmitted ($g^t_{\uparrow\downarrow}$) and the spin mixing conductance reflected ($g^r_{\uparrow\downarrow}$) (see Equation2.19) [103; 104]

$$A_{\uparrow\downarrow} = g^t_{\uparrow\downarrow} - g^r_{\uparrow\downarrow} \tag{2.19}$$

This refers to the spin current passing into normal metal as well as the spin current that is reflected and is associated with the contact area. It is usually the case that quotes of the spin mixing conductance ($G_{\uparrow\downarrow}$) are made in reference to it as the product of spin mixing conductance and quantum conductance (see Equation2.20).

$$G_{\uparrow\downarrow} = \frac{e^2}{h} g_{\uparrow\downarrow} \tag{2.20}$$

$G_{\uparrow\downarrow}$ units are $\Omega^{-1}\mathrm{m}^{-2}$ to indicate conductance per unit area. In order to remain consistent with practices in the empirical literature, this will be referred to as the spin mixing conductance (G). In the case of a magnetic insulator, spin mixing conductance is the rate at which spin polarisation is absorbed by NMs as a result of spin torque transfer due to the fact that conduction electrons are incapable of passing into YIG [105].

2.7 Ordinary Hall effect

Hall was the first to demonstrate the ordinary Hall effect in 1879 [106]. This effect results from the conduction electrons experiencing the Lorentz force:

$$\mathbf{F} = q(\mathbf{E} + \mathbf{v} \times \mathbf{B}) \tag{2.21}$$

where, $\mathbf{F}$ is the force that the conduction electrons experience, q represents the charge, $\mathbf{E}$ is the electric field that is experienced, $\mathbf{v}$ represents velocity and $\mathbf{B}$ is the magnetic field. It is the application of a magnetic field perpendicular to a sample's plane that brings about the ordinary Hall effect, resulting in electrons being deflected to a particular side of the conductor. In turn, this causes a charge to build up, resulting in a Hall potential along the conductor's transverse direction. It is possible to position probes alongside the sample to measure the Hall voltage which is calculated using the following equation:

$$V_H = \frac{IB}{net} \tag{2.22}$$

where, V_H represents the Hall voltage, I is the charge current's magnitude, B signifies the magnetic field, n is the charge carriers' density, e is the electron's charge, and t is the sample's thickness. The ordinary Hall coefficient characterises the ordinary Hall effect as follows:

$$R_H = \frac{E_y}{j_x B} = \frac{V_H t}{IB} = \frac{1}{ne} \tag{2.23}$$

where R_H signifies the ordinary Hall coefficient, E_y is the transverse electric field, and j_x is the current density. The geometry of the sample has no bearing on this quantity, thereby making it suitable for a standard coefficient [106–108]. The following equation is used to calculate Hall resistivity:

$$\rho_{xy} = \frac{V_H t}{I} = R_H B \tag{2.24}$$

where ρ_{xy} signifies Hall resistivity. By plotting Hall resistivity against B (applied field), the result is a linear gradient that gives R_H (the Hall coefficient).

2.8 Spin Hall effect and inverse spin Hall effect

The spin Hall effect (SHE) is a term used to refer to the process of transverse spin current production by an electric charge current whereby spins are polarised along an axis perpendicular to the plane containg the charge and spin current [109]. Figure 2.4a illustrates how electrons with spin up are scattered in a particular direction that is orthogonal to the flow of electric charge current. In contrast, electrons with spin down are scattered in the opposite direction (see Figure 2.4a). There is no need for a magnetic field in this process. D'yakonov and Perel [110; 111] were the first to suggest that this may be the case back in 1971. However, it was not until Hirsch [44] and Zhang [46] re-examined this theoretical work in 1999 that it started to attract the attention it deserved from those with an interest in spintronics. The inverse spin Hall effect (ISHE) is the term used to refer to the opposite effect whereby a spin current is injected with the result being a transverse electric charge current produced in a NM (see Figure 2.4b). Researchers have made considerable efforts to study the SHE and ISHE across various

systems including semiconductors such as ZnSe [112], GaAs [113–115] as well as metals such as Al [116] and Pt [117; 118].

It is spin orbit interactions that bring about the SHE [119]. The following equation denotes the spin orbit interaction that occurs in a vacuum [120] :

$$H_{SO} = -\frac{\lambda_0^2}{4\hbar}[\mathbf{p} \times \nabla V(\mathbf{r})] \cdot \sigma \tag{2.25}$$

whereby $\lambda_0 = \frac{\hbar}{mc} \simeq 3 \times 10^{-3}$ Å signifies the electron's Compton wavelength divided by 2π, p represents momentum, $V(\mathbf{r})$ is the potential experienced by the electron and σ is the Pauli spin matrix. Conventionally, this particular form would be described as being the electric field's ∇V relativistic transformation to the electron's rest frame [120]. The result is spin-orbit coupling:

$$H_{SO}(\mathbf{k}) = -\frac{1}{2}\sigma \cdot \mathbf{B}(\mathbf{k}) \tag{2.26}$$

whereby $\mathbf{B}(\mathbf{k})$ signifies a k-dependent magnetic field associated with the specific electron band under consideration. Consequently, the conduction electron momentum experiences a spin dependent perturbation.

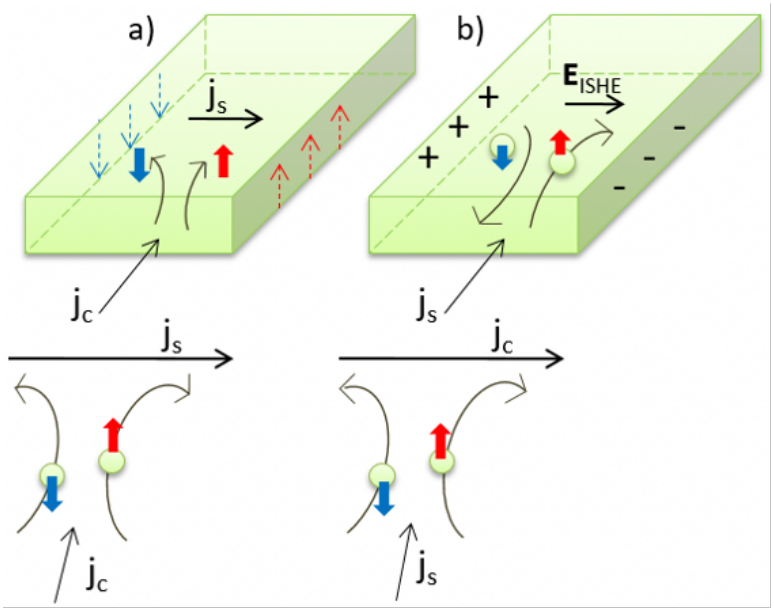

Figure 2.4: (a)The SHE concerns the creation of a spin current (j_s) from a NM that is vertical relative to the charge current (j_c). (b) The ISHE concerns the creation of a j_c in a NM that is vertical relative to a j_s ($j_c = j_s \times \sigma$). [121].

Based on the mechanisms associated with the SHE, it is possible to categorise the SHE as either intrinsic SHEs or extrinsic SHEs. The mechanism of the intrinsic SHE is associated with the material's spin-dependent band structure [122].

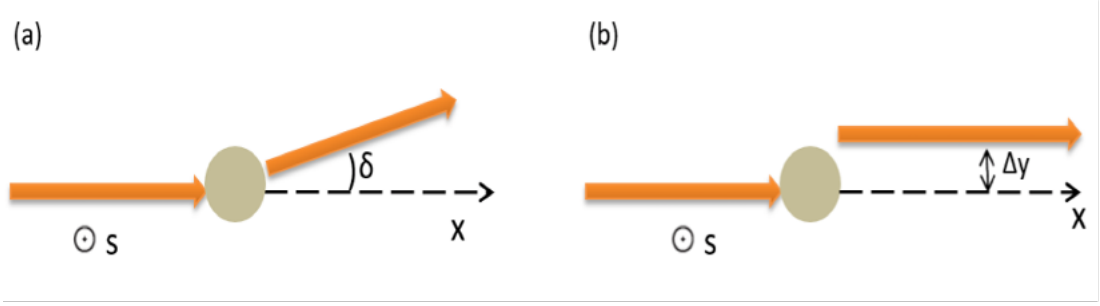

Figure 2.5: An electron's typical motion following scattering initiated from a central potential with spin-orbit interaction present. (a) depiction of skew scattering in which colliding with an impurity causes the trajectory to change to a degree equivalent to the angle δ. (b) depiction of a side jump relative to the initial trajectory ofΔ y. The electron's spin relative to the plane is directed normally [123].

Extrinsic effects are caused by impurities. There are two variations of this particular mechanism: the first is the skew scattering mechanism whilst the other is the side-jump mechanism. When spin up and spin down electrons experience asymmetric scattering involving central potential where there is spin-orbit interaction, the result is skew scattering [124; 125]. An illustration of this can be seen in Figure 2.5a. When electrons collide with impurities, this causes the trajectory of the electrons to change. It is this effect that is responsible for bringing about spin polarisation by means of a beam of electrons that is unpolarised. The following is the equation for the skew scattering influence of the conductivity associated with the SHE [120]:

$$\sigma_{ss}^{sH} = \sigma_s \rho_{ss} \sigma_c \tag{2.27}$$

where σ_c signifies Drude conductivity, σ_s represents spin conductivity, while resistivity $\rho_{ss} = \frac{m^*}{ne^2\tau_{ss}}$. In this case, n is the density of the electron, m^* represents the conduction band's effective mass and $\frac{1}{\tau_{ss}}$ denotes the rate of skew scattering.

In a spin-orbit coupled system, it is from the anomalous velocity operator that the side-jump mechanism is derived [123; 126]. This is considered to be an electron being discontinuously and finitely displaced from the initial direction. It is because of electrons and impurities colliding at random that this occurs. It is important to note

that the jump can occur in any direction relative to the direction of the incident wave. Owing to the fact that there is an identical displacement for both spin up and spin down electrons (albeit in opposite directions), the result is a spin current that is perpendicular relative to the original unpolarised charge current. The following equation is used to arrive at the contribution that the side-jump makes to spin Hall conductivity [120]:

$$\sigma_{sj}^{sn} = -2\frac{e^2}{h} n\lambda_c^2 \tag{2.28}$$

whereby λ_c denotes the conduction band's coupling constant and n signifies the density of the electron. Consequently, spin Hall conductivity is represented by the combination of two elements: $\sigma^{SH} = \sigma_{SS}^{SH} + \sigma_{sj}^{SH}$.

Spin Hall resistivity ρ_H has a term that is quadratic and linear in the electric resistivity ρ [127] :

$$\rho_H = a_{skew}\rho + b_{side}\rho^2 \tag{2.29}$$

whereby a_{skew} and b_{side} represent temperature-dependent factors that respectively provide insight into the contributions of skew scattering and side jumps.

The following equations demonstrate the nature of the relationship between the density of the spin current j_s and the density of the charge current j_c [127]:

$$\mathbf{j_c} = \mathbf{j_c^0} + \theta_{SHE}\frac{2e}{\hbar}\left(\mathbf{j_s} \times \sigma\right) \tag{2.30}$$

$$\mathbf{j_s} = \mathbf{j_s^0} + \theta_{SHE}\frac{2e}{\hbar}\left(\mathbf{j_c} \times \sigma\right) \tag{2.31}$$

whereby j_c^0 and j_s^0 signify the initial current densities, θ_{SHE} represents the angle of the spin Hall and σ denotes the spin polarisation vector. The angle of the spin Hall θ_{SHE} is arrived at by adding together the contributions made by the side jump and skew scattering mechanisms. Furthermore, the SHE is arrived at using the angle of the spin Hall θ_{SHE} which is the ratio of spin conductivity to electrical conductivity. It is apparent from equations 2.30 and 2.31 that a transverse charge current is brought about by a spin current, whereas a transverse spin current is brought about by a charge current.

When a metal layer that is not magnetic has a spin current injected into it, the spin current subsequently decays along the y axis as a result of spin relaxation [128] :

$$j_s(y) = \frac{\sinh \frac{d_N - y}{\lambda_{sd}}}{\sinh \frac{d_N}{\lambda_{sd}}} j_s^0 \tag{2.32}$$

whereby d_N denotes the thickness of the metal, λ_{sd} refers to the length of the spin-diffusion and j_s^0 signifies the density of the spin current at the interface. ISHE is responsible for transforming the spin current into charge current. In this instance, j_c^0 is 0 and, therefore, equation 2.30 becomes:

$$\mathbf{j_c} = \theta_{SHE} \frac{2e}{\hbar} (\mathbf{j_s} \times \sigma) \tag{2.33}$$

Using equation 2.32 to replace js in equation 2.33 and averaging across the thickness of Pt results in the average current density [128]:

$$\bar{j}_c = \frac{1}{d_{Pt}} \int_0^{d_{Pt}} j_c(y) dy = \theta_{SHE} \frac{2e}{\hbar} \frac{\lambda_{sd}}{d_{Pt}} \tanh \left(\frac{d_{pt}}{2\lambda_{sd}} \right) j_s^0 \tag{2.34}$$

whereby d_{Pt} signifies Pt's thickness and λ_{sd} denotes the length of the spin diffusion. A represents the Pt layer's cross-sectional area and the charge current for ISHE is arrived at by calculating $I_{ISHE} = \mathrm{A}\bar{j}_c$. Therefore, the ISHE voltage is calculated as $E_{ISHE} = I_{ISHE} R$, whereby R denotes the Pt layer's electrical resistance.

2.9 Spin Hall magnetoresistance

2.9.1 Theoretical model of SHMR

When undertaking spin Hall magnetoresistance (SHMR) experiments, the basic device comprises an FM insulator upon which a NM such as platinum is deposited and through which a current is passed. The charge current is unable to enter the FM because of its insulating qualities. The various stages of SHMR are illustrated below:

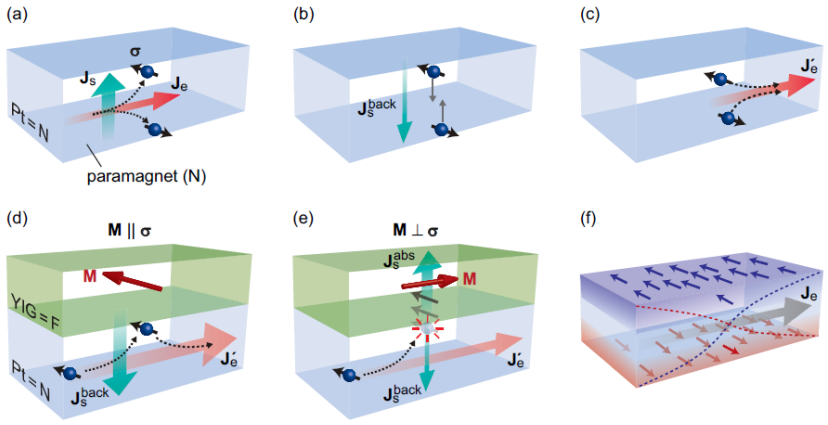

Figure 2.6: Diagram depicting the various stages of the SHMR effect and the separate contributions of the spin Hall effect and inverse spin Hall effect. When a metal has a charge current passed through it, it experiences the spin Hall effect (a), causing electrons to be deflected in a vertical direction relative to charge current with the spin orientation determining whether they are deflected upwards or downwards. When spin polarised electrons are reflected from the surface of the metal in the opposite direction, electrons are deflected as a result of the inverse spin Hall effect in the same direction as the charge current (b and c). Assuming that just a single surface of the NM makes contact with the magnetic insulator, it is with the FM's magnetisation that spin polarised electrons will interact. If FM's magnetisation is aligned with the interface spin polarisation in either a parallel manner, electrons are reflected from the interface with no spin transfer of angular momentum (d). Rotating FM's magnetisation in relation to spin polarisation causes the spin of the conduction electrons to engage with FM's magnetic moment and this causes FM to receive angular momentum. The reflected spin current is reduced by spin torque transfer into the FM thereby reducing the magnitude of Js and hence by the ISHE, the magnitude of Jc. The reduction in Jc reduces the voltage leading to an apparent increase in resistance. [105].

It is possible to measure the SHMR's size by measuring resistivity whilst rotating a

magnetic field around the current's direction. Altering the angle between the electron spin orientation and the applied field causes the SHMR to change. However, for the majority of MR it is the angle between the flow of current and magnetisation that matters. Consequently, this offers a way of differentiating between SHMR and alternative effects (e.g. AMR). It is possible to verify that an effect has not resulted merely as a result of numerous separate effects combining with alternative angular dependence by changing the orientation of how the magnetisation rotates. The following equation is used to arrive at the effect's angular dependence

$$\rho = \rho_0 - \Delta\rho \sin^2 \alpha \tag{2.35}$$

whereby α represents the angle of FM's magnetisation vector relative to NM's spin polarisation of electrons.

It is the cross product of spin accumulation along with the spin mixing conductance at the interface of NM that gives the density of the spin current. Owing to the fact that both of these measures relate to the applied field's angle, $\sin^2$ dependence is predicted.

The scale of the difference in resistivity, $\frac{\Delta\rho}{\rho_0}$, can be calculated using the following equation which involves a squared dependence on the angle of the spin Hall, θ_{sh}. Consequently, only a small effect is discernible. It is because the ISHE and spin accumulation are proportional to the angle of the spin Hall that there is such dependence.

$$\frac{\Delta\rho}{\rho_0} = \theta_{sh}^2 \frac{\lambda}{d} \frac{2\lambda G \tanh^2 \frac{d}{2\lambda}}{\sigma + 2\lambda G \coth \frac{d}{\lambda}} \tag{2.36}$$

λ is used to represent the spin diffusion length, whilst d signifies the thickness. It is the ratio of d to λ that governs where maximum SHMR resistivity is found because the length of the spin diffusion effectively constrains the effect of ISHE and spin accumulation. If the thickness is significantly greater than the length of spin diffusion, resistivity is not affected by the ISHE effect. If the thickness of FM is less than the length of the spin diffusion, interface spin accumulation is mixed owing to the close proximity. σ represents the metal's conductivity and G signifies the spin mixing conductance. The experimental data are fitted by this equation in Chapter Five.

2.9.2 Experimental observations of SHMR

Initial measurements of the effect were taken by utilising magnetic field sweeps rather than adjusting the angle. A known problem with this approach is that it fails to determine the full extent of the resistivity change. However, the magnetic field sweep achieves saturation for the YIG. If saturation were not achieved, there would not be a uniform direction of magnetisation at the platinum interface. It is this lack of uniformity that results in a different spin scattering compared to when saturated. Consequently, the resistivity change is different but it enables comparison between the effect and the YIG's hysteresis loop. Both the SHMR and the magnetisation have the same saturation points.

An experiment was undertaken to help clarify the issue of magnetic proximity. It is anticipated that the range of magnetic proximity will be relatively short owing to the fact that it relies on exchange interaction to be transmitted. For this to occur, there must be contact between the magnetic material and the platinum. A 5nm layer of copper was grown to separate the YIG and platinum, thereby ensuring that the platinum does not experience exchange interaction and there is no possibility of the proximity effect. Figure 2.7 presents the associated data. The SHMR of other materials has been found for example figure 2.8 shows the SHMR data for different thicknesses of tungsten on YIG as a function of temperature [129]. Also, figure 2.9 shows the SHMR data for different thicknesses of Ta on YIG [130].

A number of additional materials have recently been included in the effect with confirmation for palladium, tungsten, tantalum and iridium manganese. The results for palladium are especially curious because the angular dependence indicates that two effects are at play. In each of these experiments, the resistivity of the metals used is either the same as that of normal metal or the resistivity is not specified. The results for tungsten are the first to confirm that a metal's SHMR fails to adhere to this trend.

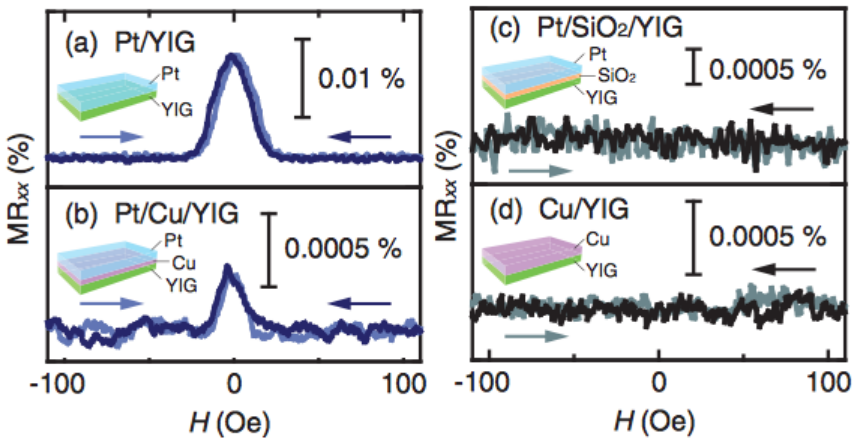

Figure 2.7: An illustration of field sweeps depicting the SHMR associated with 12nm platinum wire with various spacers positioned to separate the YI and metal. The effect is only realised if the YIG interface comes into contact with conduction electrons; magnetic proximity has no role to play in this [105].

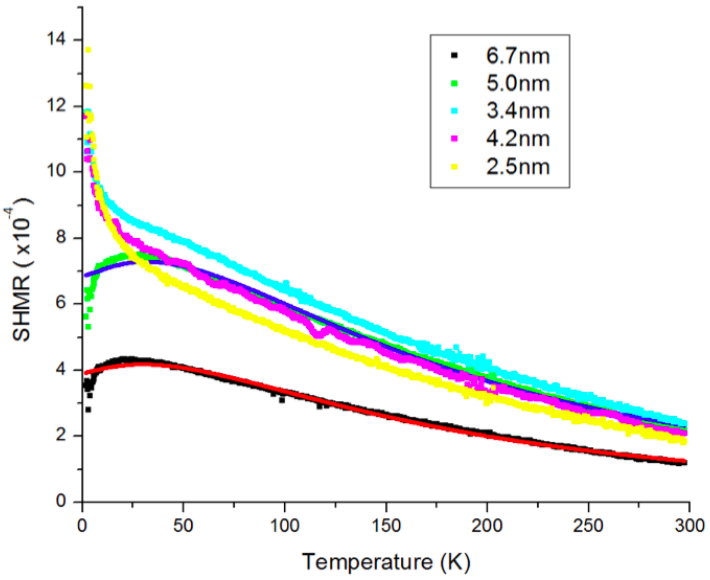

Figure 2.8: The SHMR for different thicknesses of tungsten on YIG as function of temperature. The blue and red are two fits for the EY mechanism [129].

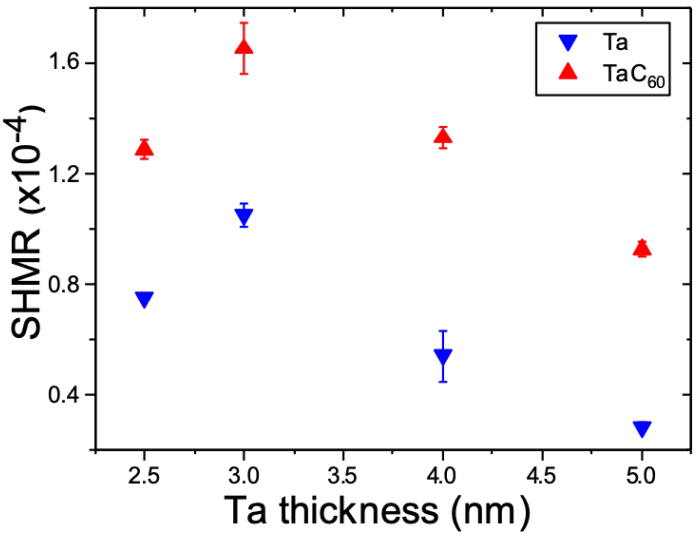

Figure 2.9: The SHMR for different thicknesses of Ta on YIG (blue) and Ta on YIG covered by C_{60} (red) [130].

2.10 Conventional Thin Film Transport

Thin metallic films of the same thickness are utilised in the current study. The purpose is to examine the concepts underpinning how impurities and geometry affect the resistivity of thin films. When discussing thin films' conductivity, the free electron theory of metals is utilised which was developed by Fuchs in 1938 [93]. This was subsequently incorporated with the theories of Sondheimer regarding electrons' mean free path in real metals [131] to produce the Fuchs-Sondheimer thin film resistivity theory. This theory has been extensively utilised and applies to the vast majority of thin film systems [132].

Classical physics teaches that a thin film's resistivity will be greater than that of a bulk sample. In the event that the thickness of a film is similar to the conduction electrons' mean free path, resistivity will effectively be dominated by the surface scattering of the film [132]. It is known from Matthiesen's rule that it is possible to calculate the

scattering process' contribution to resistivity independently and this can be combined utilising the relaxation time in an additive way [107; 133]

$$\frac{1}{\tau} = \frac{1}{\tau_{ph}} + \frac{1}{\tau_{skew}} + \frac{1}{\tau_0} \tag{2.37}$$

Equation2.37 provides an example of this whereby $\frac{1}{\tau}$ represents the rate of total scattering, τ denotes the relaxation time, τ_{ph} signifies the relaxation time from phonon scattering, τ_{skew} is the scattering resulting from skew scattering, and τ_0 is the scattering resulting from the film's defects. This equation plays a central role in the Fuchs-Sondheimer theory and comprises one aspect of the free electron theory of metals. An approximate equation was arrived at by Sondheimer so as to produce a simplified version of Fuchs-Sondheimer theory. This is important because it enables the effect that the thickness of a film has on resistivity to be established in a simple way [93; 131; 132]

$$\rho(d) \approx \rho_\infty + \frac{3}{8}(\rho l)_\infty \frac{1}{d}(1-p) \tag{2.38}$$

Whereby $\rho(d)$ represents a film of d thickness' resistivity,l_∞ signifies the conduction electrons' mean free path in bulk, ρ_∞ indicates the bulk sample's resistivity when the sample has the same composition, and p represents the factor that determines from the surface scattering.It is assumed that the surfaces of the film are parallel and smooth [93; 131; 132]. Whilst there are more advanced versions of this theory that consider matters other than the free electron model, this relatively simple version is valid in the majority of instances [132].

The total thin metal film resistivity can be calculated by a model with three types of electron scattering mechanisms, these three types are simultaneously operative: the scattering because of the external surfaces, the isotropic background scattering due to the point defects and phonons' combined effects, and the scattering because of the distribution of planar potentials (grain boundaries)[134] . The total resistivity is gained from imposing boundary conditions because of the external surfaces (as in the Fuchs theory) on Boltzmann equation. The intrinsic or bulk resistivity is gained from Boltzmann equation solving where both grain-boundary and background scattering are accounted for.[134]

2.11 Magnetoresistance in Thin Films

Subjecting a thin film to a magnetic field has an effect on its resistance. Typically, the introduction of a magnetic field will cause a thin film's resistance to increase but the opposite is true in certain cases [135]. If we have a lot of boundary scattering when we do the magnetoresistance then the electrons hitting the surface a lot but if we put a magnetic field for example longitudinal then the electrons will spiral around the magnetic field. So, as we increase the field the we stop the electrons from hitting the surface then the resistance goes down. With regards to magnetoresistance (MR), Kohler's rule applies:

$$\frac{\Delta\rho}{\rho_0} = F\left(\frac{H}{\rho_0}\right) \tag{2.39}$$

Whereby $\frac{\Delta\rho}{\rho_0}$ represents for the magnitude of the magnetoresistance in the thin film, ρ_0 signifies the resistivity for the zero-field, and $\Delta\rho$ indicates the effect that applying field H has on resistivity. The parameter F represents a function of the sample's composition and geometry, causing MR at various temperatures to be positioned along a given curve, albeit achieving differing magnitudes [135; 136]. As such, when measurements are taken at relatively low temperatures (i.e. when ρ_0 is relatively low), this indicates a greater $\Delta\rho$ as well as a more pronounced MR.

It is possible that a negative MR can be realised when utilising ferromagnets if there is a prevalence of s-d scattering and the respective domains have a magnetic polarisation that is distinct from that of the majority of the sample. It is also possible that s-d scattering could become elevated as a result of impurities and this could result in the MR becoming negative and non-standard. This occurs as a result of the spins at impurity sites experiencing magnetic polarisation and being impacted by the magnetic field they are subjected to [135; 137].

CHAPTER 3

Experimental techniques

3.1 Introduction

This chapter initially provides details of the methods by which the deposition of nm-thick YIG films can be achieved along with a number of innovative approaches to characterise thin YIG films. This starts with a description of how RF magnetron sputtering can be used for the deposition of YIG as well as how YIG/Pt bilayer structures can be grown. X-ray diffraction (XRD) and x-ray reflectivity (XRR) are used to characterise thin YIG films so as to arrive at their crystallinity, thickness and quality. Meanwhile, atomic force microscopy (AFM) is utilised to gauge how rough the surfaces of these films are. Meanwhile, vibrating sample magnetometer (VSM) and superconducting quantum interference devices (SQUID) VSM are employed to determine YIG films' magnetic qualities. Furthermore, low temperature transport measurements are used to investigate the spin hall magnetoresistance and anisotropic magnetoresistance in the YIG/Pt.

3.2 Deposition methods

3.2.1 Substrates

Owing to the fact that the crystal structure of YIG is highly complex, it is necessary to select an appropriate substrate to ensure the as-sputtered material grows as intended. Provided that the lattice constant as well as the structure of the substrate have a structure the same as the desired YIG, it is possible to produce epitaxial films. In addition, it is necessary for the lattice constants to be alike. In the event that the lattice constants differ, the films will experience strain at the interface [138]. In the empirical literature, gadolinium gallium garnet (GGG) is widely used and it has been selected for the current study. The chemical formula of GGG is $\mathrm{Gd_3Ga_5O_{12}}$ and it shares its garnet crystal structure with YIG. GGG has a lattice constant of 12.383 Å, whereas that of YIG is 12.376 Å [139].

The Czochralski process is employed to produce GGG with a seed sample and the constituent elements being subjected to molten flux [140; 141]. A comparable process

is used to produce YIG through liquid phase epitaxy (LPE). Each of the substrates share the same $<111>$ crystal axis protruding from the plane and it is ensured that the interface is smooth by carefully polishing the surface. Utilising AFM, it was confirmed that the RMS roughness of the surface was under 0.2nm. It is the roughness of the surface that ultimately governs how smooth the films will be that are produced upon the surface. Such is the strength of the GGG paramagnet that it can interfere with magnetic measurements. YIG films have relatively limited magnetic moments in comparison to this background effect and, therefore, it must be removed. However, this proves problematic when the temperature is low. Curie's law applies to paramagnetism because there is an inverse relationship between magnetisation and temperature. Figure 3.1 illustrates the moment for a sample of GGG, demonstrating the scale of the issue. For a YIG film of 40 nm in thickness, the contribution to the moment will be in the region of 10^{-3} emu. If the temperature is sufficiently low, paramagnetism can result in a sufficiently large signal to cause the lock-in amplifier to become overloaded, thereby ensuring that data cannot be taken. Thermal stability is critical when the temperature is relatively low.

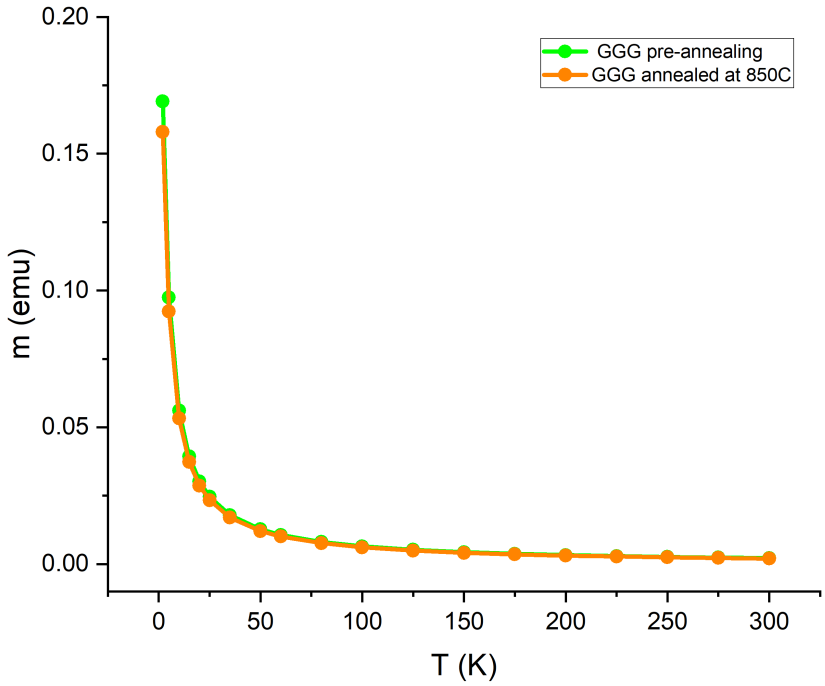

Figure 3.1: The relationship between temperature and magnetic moment for GGG at a 10mT applied field. This moment is of a similar size to that of thin YIG films, with the result that problems are likely to be encountered when measuring the hysteresis loop when temperatures are low.

The diamagnetism of Yttrium aluminium garnet (YAG) is particularly weak and this overcomes the issues with intense para-magnetism. Unlike YIG, the lattice constant of YAG is 11.953 Å [142] and, consequently, this has a bearing on how magnons are propagated as well as resulting in additional strain.

3.2.2 Fabrication of materials

It has been necessary to produce numerous samples for the current study including YIG magnetic insulator thin films as well as metallic element thin films. Direct current (DC) magnetron sputtering was utilised to produce metallic thin films, whereas radio frequency (RF) magnetron sputtering was employed to create the YIG thin films. A detailed account of these processes is provided below.

3.2.2.1 YIG Preparation

There are various options for how to produce the complex YIG material including RF magnetron sputtering, liquid phase epitaxy (LPE) and pulsed laser deposition (PLD). However, for the current study, the decision was taken to employ RF magnetron sputtering because of the benefits it affords in terms of cost and the speed of the process (two qualities that are highly desirable in manufacturing processes). Following deposition by sputtering, further processing is necessary to achieve a film with ferrimagnetic ordering and this entails annealing.

3.2.2.2 Growing Pt on YIG

A mask with an independent substrate wheel is employed to produce the metals required for the current study. An illustration of the mask used is provided in Figure 3.2. Numerous samples can be deposited using just a single mask because between the sample wheel and mask wheel is a motor capable of moving the mask between substrates. When it is necessary to produce wires of various thicknesses or to create tunnel junctions, several masks can be employed. In order to produce films with clearly defined edges, pressure is applied to the mask to ensure it is flush with the substrate positioned on a firm spring to achieve a good contact. Unless a good contact is made between the mask and sample, the edges of the film are likely to be poorly defined when the shadow masking method is utilised.

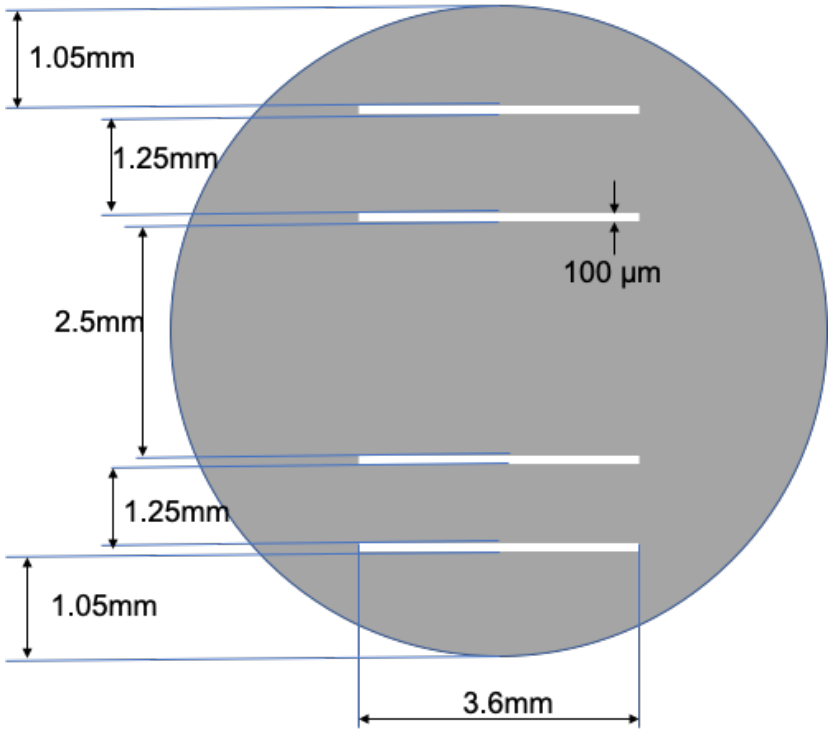

Figure 3.2: Depiction of the shadow mask utilised when depositing metals by means of sputtering.

3.2.3 RF and DC sputtering deposition

Sputtering entails thin films being vapour deposited upon substrates and is a form of plasma deposition. This entails the electrical ionisation of sputtered gas with the result being a plasma. Subsequently, ion bombardment coupled with target material being ejected to the substrate causes the target material to be removed. Sputtering offers a number of benefits including excellent control over thickness and smoothness; a high rate of deposition; consistent application over relatively large areas; considerable versatility utilising momentum transfer rather than reactions of a chemical or thermal nature, thereby ensuring that all materials are capable of being sputtered.

There are two electrodes in the sputtering deposition chamber which are held in

a vacuum supplied with high voltage power from an external source. The 'target' is the material being deposited and this is effectively the cathode. The sample wheel is earthed and it is upon this wheel that the substrates are positioned. Figure 3.3 illustrates the sputtering system. Into the vacuum chamber is added the sputtering gas. In order for an atom to be sputtered from the target, it is necessary for the ion-induced collision to have sufficient momentum transfer to surmount the binding energy that creates a surface barrier. There is electrical discharge generated as a result of a voltage being applied between the anode and cathode and the result is that the gas becomes partially ionised. When the energy with which these ions hit the target is adequate to cause surface atoms on the target to be ejected, they will then be deposited onto the substrate. As this process continues, the voltage accelerates the free electrons and ionised gas, causing them to collide and resulting in the gas continuing to ionise. Upon reaching a breakdown condition, the plasma becomes stabilised. It is the secondary electron emission that provides most of the electrons required for the plasma to be sustained. The sputter yield is a term used to refer to the rate at which surface atoms are ejected represented as a ratio of atoms ejected from the surface (mean value) to the number of incident ions striking the target. There are various factors that can affect the sputter yield including the particles' incident angles; the incident particles' energy; the target atom and ion's atomic weights; and the crystal structure of the surface of the target [143]. The maximum sputter yield is realised with an energy of between 10keV and 100keV and with an incident angle of between $60° - 80°$[143].

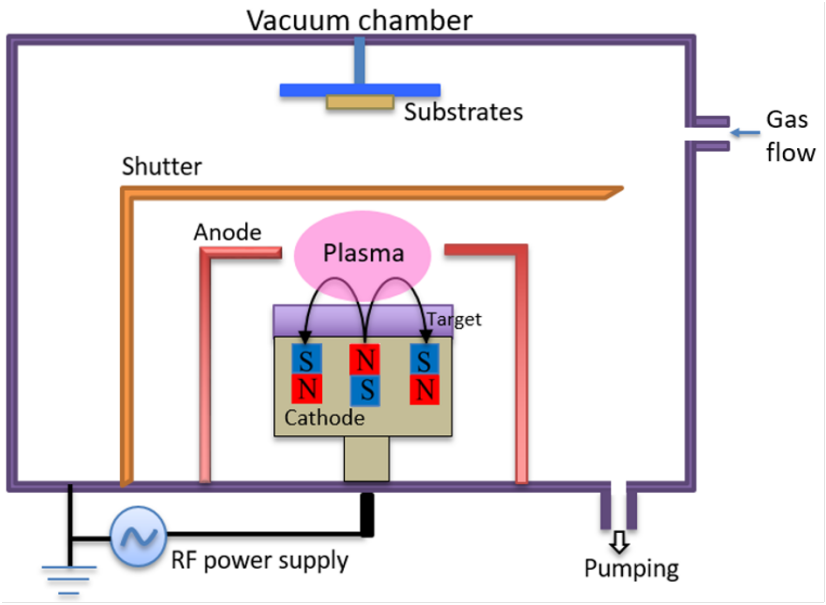

Figure 3.3: Illustration of on-axis sputtering. The evacuated chamber has sputtering gas added and among the anode and cathode there is a RF voltage. As the electrons between the electrodes accelerate, this causes the ionisation of the argon atoms and this creates plasma. As the target is bombarded with ionised ions, the target's surface ejects materials that are then deposited upon the substrate [121].

The choice of material being deposited determines whether the RF or DC sputtering methods are employed. RF sputtering is used to deposit thin films of insulators and DC sputtering is employed when depositing metal. For the purposes of RF sputtering, an oscillating radio frequency (RF) voltage in the region of 13.56MHz is used so as to ensure the glow discharge is sustained and the electrode is biased. The use of an alternating current ensures that the front of the insulator will not experience an accumulation of a surface charge of positive ions. For the purposes of DC sputtering, in order to generate plasma between the electrodes, a DC voltage of at least 400V is required. During the negative cycle, the target is sputtered and during the positive cycle the cathode attracts electrons, resulting in a negative bias. Having ejected the sputtered atoms, they become deposited upon the substrate. Magnetron sputtering entails the target having permanent magnets positioned underneath, thereby ensuring that the Lorentz force causes the plasma to be confined.

When electrons are ejected, their motion is cycloidal and their orbits migrate towards $\vec{E} \times \vec{B}$, where $\vec{E}$ represents the discharge's electric field and $\vec{B}$ is the transverse magnetic field (see Figure 3.4 a). The orientation of the magnetic field ensures that the electrons' move in a manner that encircles the target, thereby serving as an electron trap (see Figure 3.4 b). Trapping electrons makes it more likely that the sputtering gas will be ionised, thereby causing the plasma to become more dense and accelerating the rate at which deposition occurs.

There are a total of 7 sputtering guns in the on-axis sputtering system: 1 for insulator, 2 for magnetic, and 4 for the deposition of metal. There is also a single evaporation source. There are 16 separate slots on the sample wheel for the substrate and a shutter system to enable multilayers of various materials to be grown.

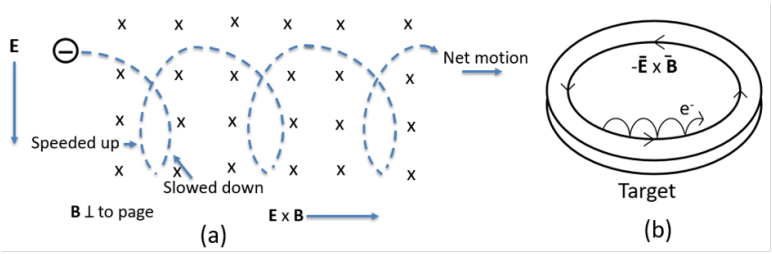

Figure 3.4: a) A closed loop results from the movement of an electron when faced with magnetic and electric fields; b) A cycloidal path results from electrons moving towards E x B when the velocity of movement is E/B [121].

Computer software is used to manipulate the sample wheel as well as the position of the shutter. A distance of approximately 7 cm is maintained between the substrate and target. A vacuum is required for sputtering at a pressure of approximately 10^{-8} Torr. Initially, a cryopump and roughing pump create a pressure of 10^{-7} in the chamber but then a Meissner nitrogen trap reduces the pressure to 2×10^{-8} Torr with the result that atmospheric residual water vapour is condensed. RF magnetron sputtering was employed to grow thin YIG films on both (111) GGG and YAG substrates. A combination of the temperature, pressure, flow of sputtering gas and RF power govern the rate of deposition. Whilst YIG films are being deposited, a base pressure of

2.4×10^{-8} Torr is maintained in the chamber along with total rate 24 SCCM of argon flow and oxygen flow (different oxygen content in the sputtering atmosphere between 5% to 6.8%) produces the most accurate YIG stoichiometry. Finally, RF power was held constant at 50W at 13.56MHz. Intersecting the discharge chamber and power supply is an impedence-matching network set to avoid power being reflected back to the source. It is necessary to use water to cool the inductor and target in the matching network. Upon deposition, the YIG film is amorphous and this suggests that YIG is deposited as a combination of the elements it comprises. The elements that make up YIG are not of a uniform mass and, therefore, each of these elements has its own sputter rate and mean free path. Oxygen is incorporated into the atmosphere of argon so as to slow the rate of growth and ensure that iron and yttrium are deposited with the stoichiometry required for YIG. The measured rate of deposition was 0.16 Å/s. This rate was set based on how thick the samples were following the x-ray reflectivity curve being fitted.

DC magnetron sputtering is used to deposit Pt onto samples of annealed YIG to produce YIG/Pt bilayer samples. An ultrasonic bath with isopropanol and acetone is used to clean the sample of Pt prior to initiating the depositing process. Using 9W of power and 25mA, the rate at which Pt was deposited was 1.65Å/s.

3.2.4 Annealing

Owing to the fact that the deposited YIG films are not magnetic and also amorphous, there is a need for them to be annealed to produce crystalline YIG throughout the length of the GGG crystalline plane. Isopropanol and acetone are used to clean the samples for the purpose of annealing and the samples are swiftly put into a tube furnace for a period of 2 hours at 850 °C in open air conditions. The samples must by positioned within an area of 15cm at the centre of the furnace to ensure that they experience the same temperature. Cycles of heating and cooling are initiated at 5 °C/minute to ensure that the films do not experience strain. Having been annealed, it is necessary for the samples to be returned to the sputtering chamber so that the YIG can receive deposit of Pt.

3.3 Surface and Structural Characterisation

3.3.1 X ray reflectivity

Thin films can undergo structural characterisation without the possibility of being damaged by utilising XRR. XRR offers a proven means of establishing the parameters of thin films including their density and thickness as well as the roughness of their interfaces and surfaces. In cases where x-rays are incident on the sample, the material's refractive index n is marginally lower than 1, calculated as follows:

$$n = 1 - \delta \tag{3.1}$$

where $\delta = \frac{2\pi\rho r_0}{k^2}$. ρ, r_0 and k represent the electron density, Bohr radius and wave vector, respectively and δ is the order of 10^{-5}. In the event that the angle of incidence for the x-rays on the sample has a grazing angle below that of the critical angle of incidence θ_c, total reflection is experienced and the x-rays are unable to enter the sample. However, refraction takes place if the angle of incidence is $\theta > \theta_c$ and the x-rays are able to enter the sample.

To interpret the relationship between the angle of incidence θ and the angle of refraction θ', Snell's law of refraction is utilised:

$$\cos\theta = n\cos\theta' \tag{3.2}$$

Snell's law can be used to determine the critical angle by putting $\theta' = \theta_c$ expanding the cosine to arrive at the critical angle's expression. The following formula is used to calculate the critical angle of incidence θ_c:

$$\theta_c = \sqrt{2\delta} = \sqrt{\frac{4\pi\rho r_0}{k^2}} \tag{3.3}$$

It is necessary to measure the critical angle because it offers insight into the reflecting material's electron density [144; 145].

Grazing incidence and the straight-through beam are used when measuring reflectivity so that the area under $\sim 0.4^{\circ}$ is attributable to instrument function (for instance, beam optics). Following this there is a marked reduction in intensity at the critical angle where the beam starts to penetrate the upper-most layer of the surface. The profile that is reflected indicates oscillations resulting from x-ray interference as they are reflected from the film's surface as well as the film/substrate interface. Such oscillations are referred to as Kiessig fringes [146]. It is possible to calculate thin films' densities, thicknesses and well as the roughness of their interface and surfaces based on analysis of reflectivity intensity curves.

A good quality of fit indicates that the material is smooth and the layers are parallel to the substrate. It is the discrepancy between the substrate and film densities that determines the oscillations' amplitude. A greater discrepancy results in a higher amplitude. As such, it is possible to infer the film's density from both the critical angle as well as the amplitude of oscillations. Moreover, it is possible to infer a film's roughness based on the rate of reflectivity decay. The reduction in reflectivity is more pronounced when the surface is particularly rough; therefore, the rougher the surface, the quicker the oscillations decay. Meanwhile, details about how thick a film is can be determined based on the angular positions of oscillation. It is possible to utilise the Kiessig equation to calculate a film's thickness (t) based on an interpretation of the interference pattern's angular distributions:

$$\lambda = 2t\sqrt{\sin^2\theta_n - \sin^2\theta_c} \tag{3.4}$$

whereby n represents an integer, λ indicates the wavelength and θ_n is the constructive peaks' angular position [145; 147].

The modeling fits from Bede$_{REFS}$ Mercury software [148] was used to provides the valuable information about the thickness of our films, the roughness of the film surface and the interfacial roughness , and also, the electron density [149].

3.3.2 X ray diffraction

The XRD method can be applied to determine a material's crystal structure. It is based on coherent interference resulting from the scattered waves emanating from areas that are electron-dense. Diffraction results when electromagnetic radiation is incident on atomic planes and the crystal's atoms cause scattering. If scattered rays are to interfere in a beneficial manner from consecutive crystallographic planes, it is necessary for these rays to satisfy Bragg's law:

$$n\lambda = 2d_{hkl}\sin\theta \tag{3.5}$$

whereby n represents an integer governed by the diffraction peak order, λ indicates wavelength and d_{hkl} relates to the spacing of the lattice. It is Bragg's law that governs XRD which results in Bragg's peak in high angle scans. Bragg developed the equation in 1913 as a means to explain crystals' cleavage faces are able to reflect x-rays at particular angles of incidence. In the current system, a copper target that has a typical wavelength of λ = 1.54Å generates Cu K_α x-rays. The resulting electrons are accelerated in the direction of a copper target by introducing a high voltage. Upon striking the target, the electrons shed kinetic energy, possibly resulting in electrons from the metal atoms' K shell to be knocked out. It is electrons that drop from the L and M shells that fill the resulting hole and this causes x-ray photons to be emitted that have an energy equivalent to the discrepancy between the energy levels of wavelengths Cu K_α and Cu K_β. The Cu K_β is filtered out when the x-ray photons travel across a range of filters and slits with the result being a beam that is collimated monochromatic.

Figure 3.5 a illustrates how an incident x-ray engages with periodically-organised atoms in a lattice plane. Spheres are used to indicate atoms and these create an alternative series of lattice planes in crystals. In accordance with Bragg's law, parallel planes that have an index hkl and lattice spacing d_{hkl} produce a diffracted beam when x-rays with a wavelength of λ strike atoms at an angle of θ and are caused to reflect at an identical angle. Figure 3.5 b depicts the core implements required for a XRD including a sample stage, detector and source of x-rays. X-rays strike the sample at an angle of θ and when x-rays are reflected it is a mobile detector positioned at an angle of θ that detects these reflected x-rays.

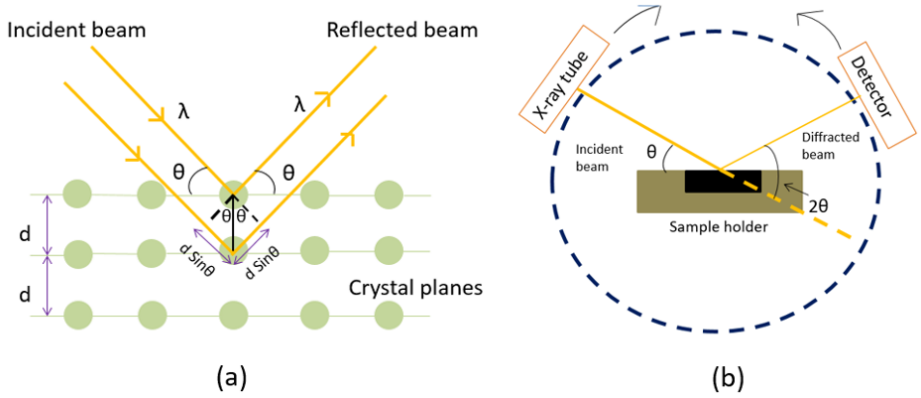

Figure 3.5: a) A depiction of Bragg conditions concerning x-ray diffraction caused by a crystal's atomic planes. Crystal planes reflect incident waves. In the event that Bragg's law ($n\lambda = 2d\sin\theta$) is satisfied, diffracted waves are in phase. b) Illustration of a set-up for XRD involving a sample stage, detector and a source of x-rays [121]

In order to take specular condition measurements, it is necessary for the angle at which the detector moves to be twice that which the sample moves. The angle of incidence was adjusted to take measurements and the resulting intensities of the diffracted peaks generate a pattern of diffraction.

3.4 Magnetometry

3.4.1 Vibrating Sample Magnetometer (VSM)

VSM offers the ability to measure a thin magnetic film's magnetic moment. VSM are based on Faraday's Law of Induction and the sample being studied is retained within a magnetic field. Assuming that the sample is magnetic, the field will have the effect of magnetising the sample, causing the domains or spins to become aligned with the field. The sample's magnetic dipole moment generates a magnetic field enveloping the sample and this is referred to as the magnetic stray field. Vibrating the sample at a specific frequency causes the stray field to alter as a function of time, causing the pick-up coils to generate an electric current that is relative to the sample's moment.

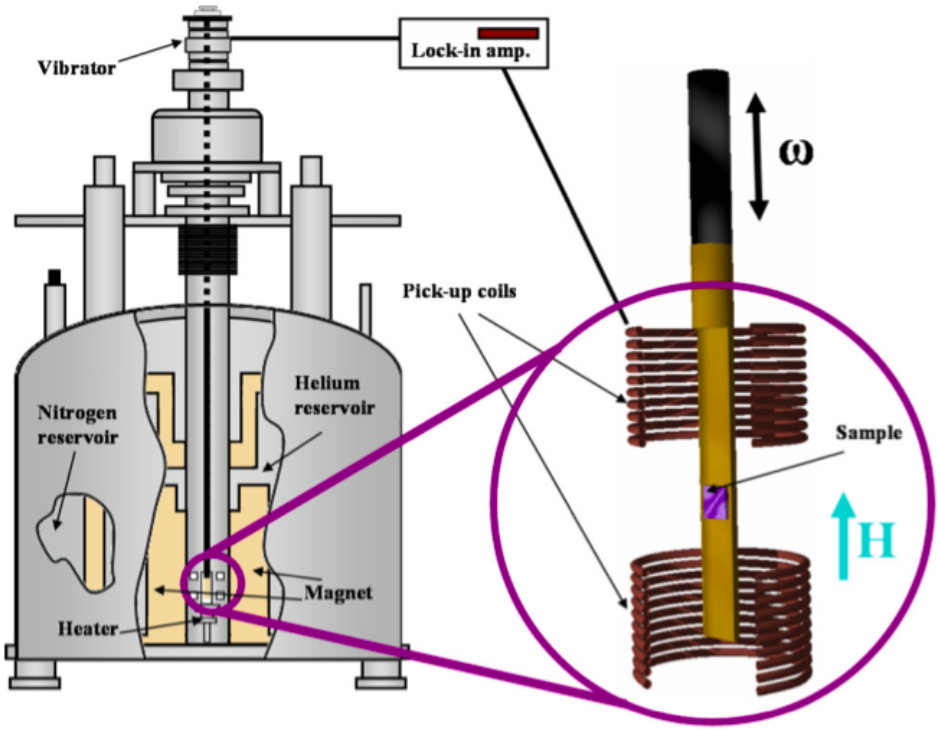

Figure 3.6: Illustration of a vibrating sample magnetometer. A magnetic field is applied and the samples vibrate. The voltage that results in the coils is gauged and the coils are wound in different directions so as to minimise background interference [150].

It is possible to set a temperature between 1.5K and 305K using the Oxford Instruments Maglab VSM. Figure 3.6 depicts a vibrating sample magnetometer. Having attached the sample upon a Polyether ether ketone (PEEK) paddle, the paddle, in turn, is connected to a rod of carbon fibre and positioned within a helium flow cryostat amid two pick-up coils. In a bath of liquid helium is a variable temperature insert (VTI) and into this is positioned the rod. In turn, the liquid helium sits in a reservoir of nitrogen with a vacuum jacket keeping the two apart. A small helium inlet in conjunction with a DC resistance heater at the bottom of the VTI facilitates a flow of liquid helium and it is this that achieves a constant temperature. A roughing pump ensures that the pressure within the VTI is held constant. Around the sample chamber is a superconducting

magnet that is capable of generating a magnetic field of 9T parallel relative to the rod. The lock-in attached to a vibrator at the uppermost part of the VTI vibrates the sample at 55Hz and this causes the magnetic flux to alter with the coils inducing an EMF. This change in flux is amplified and the lock-in amplifier interprets this with the result being that the pick-up coils generate electrical current.

The thin magnetic films only generate a small signal and, therefore, care is required to ensure that there is no interference from the substrates and probe generating background signals. Moreover, it is necessary to prevent magnetic impurities contaminating the surface by ensuring the samples are prepared in a clean setting.

3.4.2 Superconducting Quantum Interference Device

When a high degree of sensitivity is required when measuring small magnetic moments, the optimum magnetic sensor is a superconducting quantum interference device (SQUID). The operation of SQUID relies on quantum effects in superconducting loops. Underpinning the SQUID is a Josephson junction which enables current to flow between superconductors partitioned by a thin insulator by means of quantum tunnelling. In effect, a Josephson junction enables Cooper pairs to tunnel by establishing a gap between the superconductors. There can be single (RF SQUID) or double (DC SQUID) Josephson junctions in a SQUID and the Josephson junction is illustrated in Figure 3.7.

The supercurrent I_s associated with the Josephson equation moves along the junction and this is associated with both the junction's relative phase difference δ as well as its critical current I_0:

$$I_s = I_0 \sin \delta, \delta = \theta_1 - \theta_2 \tag{3.6}$$

whereby δ represents the discrepancy between the superconductors; phases θ_1 and θ_2.

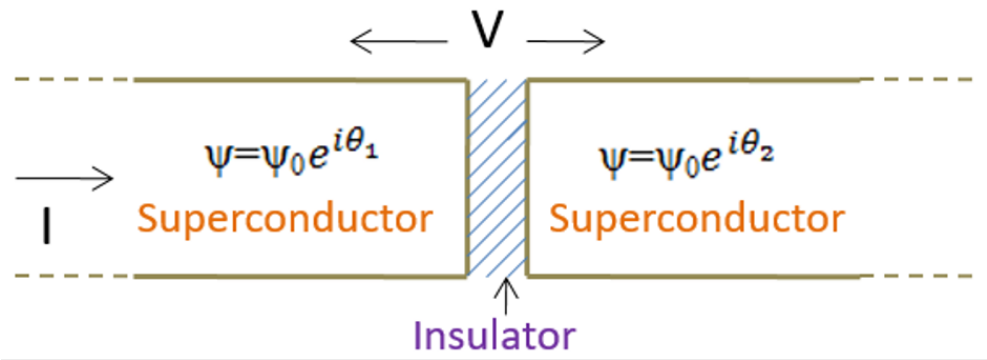

Figure 3.7: Illustration of a Josephson junction comprising 2 superconductors parted by an insulator. Cooper pairs are able to tunnel through the insulator, thereby enabling a supercurrent to flow. Ψ represents the superconducting state's wavefunction in the superconductors. the phases are indicated by θ_1 and θ_2 [121].

A Quantum Design SQUID-VSM MPMS3 detection system similar to that depicted in Figure 3.8 has been employed in the current study to examine the samples' magnetic qualities. With a sensitivity of approximately 10^{-8} emu, the system is able to function with magnetic fields as high as 7T and across temperatures of between 1.8K and 1000K. The system comprises superconducting detection coils connected inductively with the DC SQUID. Having positioned the sample on a quartz holder, this holder is then attached to carbon fibre sample rods that taper and have adapters at both ends. The measurement system vibrates the sample at a frequency of ω at the detection coils' midpoint. There is a default vibration amplitude of 2mm, whilst the vibration frequency is at a default setting of 14Hz. Vibrating the magnetised sample causes the detection coils to experience a change in flux. Altering the detection coil's magnetic field brings about a shift in the input coil's magnetic field. There is magnetic coupling between the input and primary coils and any divergence in magnetic flux is detected.

In a DC SQUID there are parallel Josephson junctions comprising a superconducting loop. Any input current (I) is divided in equal proportion between the two junctions unless there is an external magnetic field to exert influence. If there is an external magnetic field, the superconducting loop experiences a screening current (I_s) and the result is a magnetic field of the same size albeit the reverse of the field applied, thereby nullifying the net flux.

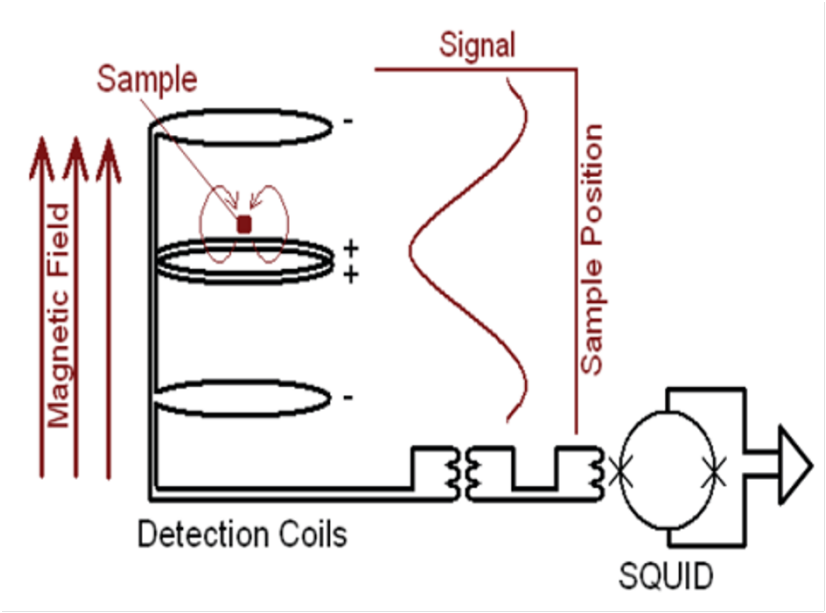

Figure 3.8: Depiction of SQUID VSM MPMS3 detection system [151] whereby the superconducting detection coil, inductor input coil and DC SQUID are all connected.
.

The screening current and the input current are flowing in an identical direction one a branch of the superconducting loop but in opposite directions in the alternative branch. Therefore, one branch has a total current of $\mathrm{I}/2+I_s$, whilst the other has a total current of $\mathrm{I}/2-I_s$. There will be a voltage across the junction whenever the current in any one of the branches surpasses the junction's critical current. Increasing the magnetic flux causes the screening current to rise and at the point where the magnetic flux is equivalent to half a quantum ϕ_0(ϕ_0= h/2e is the flux quantum), there is no current passing through the SQUID and the junctions are fleetingly resistant (at least in theory). When there is half flux quantum, the sign of the screening current flips but at one flux quantum it is zero, whereupon the total current returns to its maximum. The following equation gives the total current:

$$I_{tot} = 2I_0 \left|\cos\left(\frac{\pi\phi}{\phi_0}\right)\right| \tag{3.7}$$

Changes in the current of the detection coils are proportional to alterations in magnetic flux and the result is an output voltage (V) over the junction that is effectively governed by the magnetic flux being applied and the period of ϕ_0. As a result of the alteration in flux, whilst the current in the detection coils is cancelled by the SQUID feedback circuit, this is not the case for the induced current [152; 153]. The instrument electronics cause the voltage of SQUID to become amplified and digitised. The magnetic coupling of the input coil and primary coil must be highly efficient in order to achieve a high degree of sensitivity.

3.5 Atomic force microscopy (AFM)

AFM enables images to be produced with a vertical resolution of 0.1nm and lateral resolution of tens of nanometres. Gerd Binnig is attributed with inventing AFM and it was first utilised for research purposes during 1986 [154]. Crucially, AFM entails measuring the force that exists between the tip of the cantilever on an AFM and the surface of a sample being examined. Whilst oscillating, there are two core types of force: short-range repulsive and van der Waals forces [155–157]. There may also be additional forces; e.g. capillary or adhesion forces. In the current study, the tapping mode was selected in order to ensure that the sample's surface would not be damaged. When using the tapping mode, the tip of the cantilever oscillates at a frequency close to its resonance , ω_0 as a result of a force with an amplitude of F_0 whilst scanning the sample's surface. This entails contact being made between the cantilever and a piezoelectric crystal that is experiencing an oscillating voltage. The following equation indicates the way in which the tip of the cantilever loves:

$$m\frac{d^2z}{dt^2} + kz + \frac{m\omega_0}{Q}\frac{dz}{dt} = F_{ts} + F_0\cos(\omega t) \tag{3.8}$$

where Q represents the quality factor, ω is the driving force's angular frequency and k is the free cantilever's force constant. Meanwhile, z indicates the cantilever's

transverse displacement and F_{ts} is the forces of interaction at the tip-surface. If these forces are not present, Equation 3.8 provides a description of the forced harmonic oscillator's movement when there is damping. Solving the equation entails a steady solution and transient term. At the outset, the motions are both dominant but after a period of $(2Q/\omega_0)$, the transient term is diminished by a factor of 1/e and this has the effect of ensuring that the steady solution dominates. The following equation gives the steady state solution which is a sinusoidal function:

$$z\left(z_c, t\right) = z_0\left(z_c\right) + A\left(z_0\right)\cos\left(\omega t - \phi\left(z_c\right)\right) \tag{3.9}$$

whereby z_0, represents mean deflection, A is the amplitude, ϕ indicates the phase shift of oscillation and z_c is the distance that the tip is from the surface of the sample [155; 156].

There are changes to the amplitude of vibration and the phase difference regarding excitation changes and the response of the cantilever when the sample is scanned by the tip. The photodetector monitors the oscillating signal. It is usually the case that a frequency somewhat lower than the resonance is selected so as to achieve the greatest possible sensitivity of the amplitude measurement. It is by passing the tip over the surface of a sample that an image is generated and measurements are taken point-by-point. Careful control is achieved over the movements of the tip using 3 piezoelectric crystals; one of the crystals is responsible for achieving the desired distance between the sample and the tip (z) and the others govern how the tip moves across the sample (x and y). Tips used in tapping mode have relatively short cantilevers (typically $(125\mu\mathrm{m})$), relatively high spring constants $(\sim 50\ \mathrm{N/m})$ as well as relatively elevated resonance frequencies $(\sim 300\mathrm{kHz})$.

In addition, there is a need for a feedback loop so as to ensure that the oscillation amplitude of the cantilever is held steady. Figure 3.9 a depicts the arrangement for atomic force microscopy utilising AFM electronics. At the rear of the cantilever is a reflected laser beam with a four quadrant photodetector employed to gauge the intensity of that reflection (see Figure 3.9 b). The signal alters as the tip nears or moves away

from the surface owing to changes to the tip's resonance frequency altering when the tip interacts with the surface. Tapping mode entails the use of a high frequency voltage for the excitation piezo and this serves as a signal picked up by the lock-in amplifier that it uses to get the photodetector data's amplitude signal. Comparisons are subsequently made of the measured signal by means of the feedback loop using a voltage specified by the person operating the apparatus.

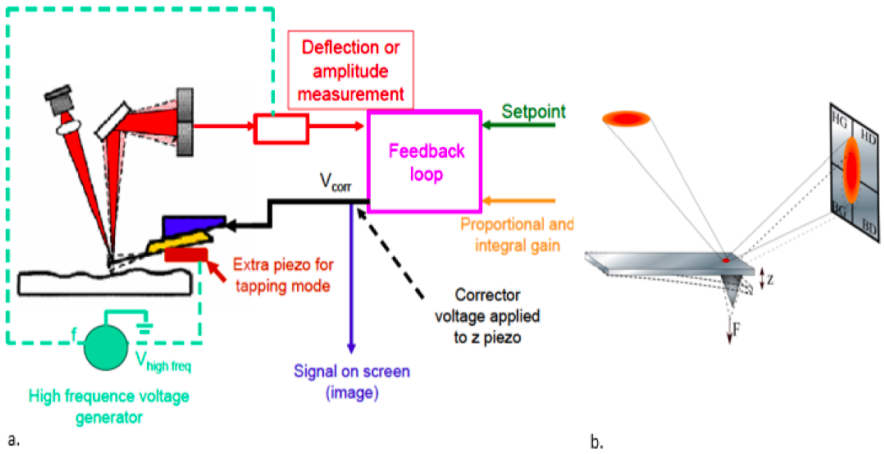

Figure 3.9: Illustration of how an AFM is set up. Operating in air during tapping mode, the tip of the cantilever scans the sample's surface with a feedback loop governing how far the tip is from the sample. Computer evaluation generates a topographical image. b) A four quadrant photodetector capture the intensity of the reflected laser beam as it passes the rear of the cantilever [121].

Whilst functioning in tapping mode, the setpoint specifies free amplitude as a percentage. In the event that the measured value is the same as the setpoint value, there is no reaction from the feedback loop. However, if there is a discrepancy, a V_{corr} signal is sent by the feedback loop to the z piezo so as to adjust the position of the tip in a way that ensures the two values are identical. The V_{corr} signal is calibrated in nm and provides quantitative data from which it is possible to derive the root mean square (RMS) roughness of the surface in the image produced of the surface on the monitor. It is necessary to optimise the integral and proportional gains in order to ensure a rapid

response by the feedback loop whilst avoiding additional noise being incorporated into the data. Nanoscope software was employed to analyse the AFM image, whilst AFM was used to establish how rough the samples of YIG were.

3.6 Low Temperature Electron Transport

Measurements of magneto-transport are taken in gas flow helium (He) cryostats at low temperatures of between 1.5K and 300K. Figure 3.10 illustrates how a cryostat is operated and the underlying principles.

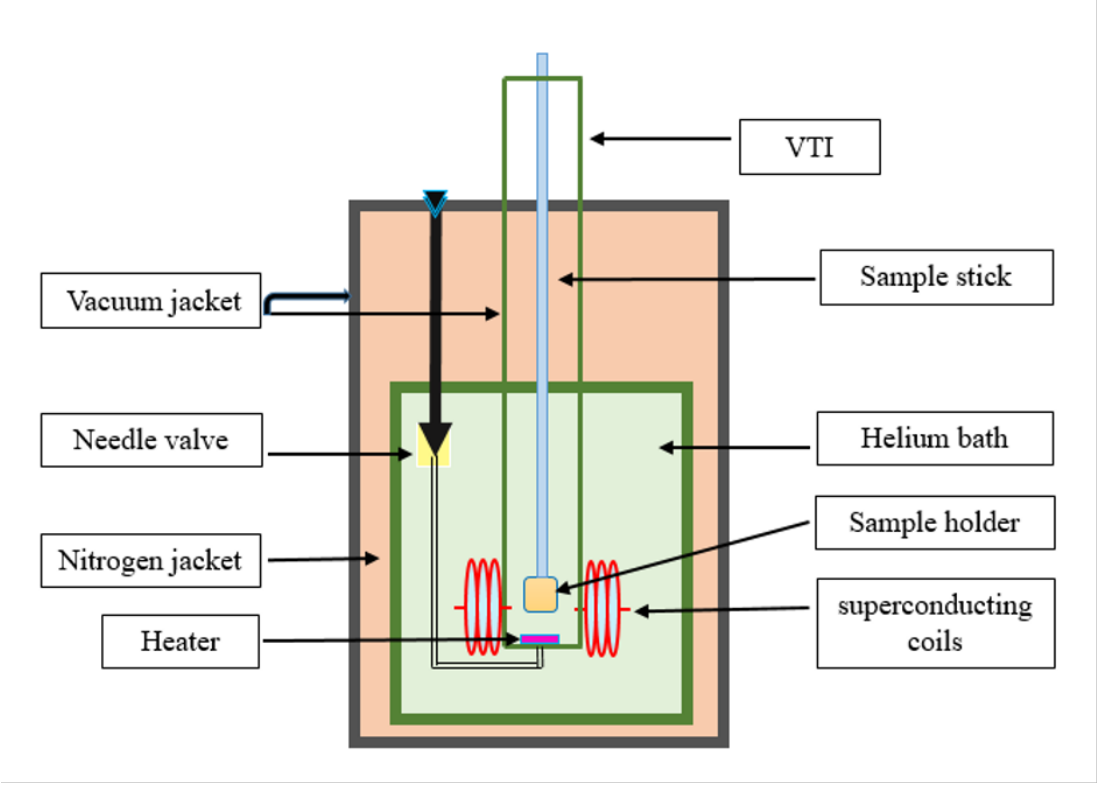

Figure 3.10: : Diagram of a gas flow cryostat including the variable temperature insert (VTI). The sample head surrounds the sample and the precise positioning of the sample may differ [158].

The set-up illustrated in Figure 3.10 involves a sample stick with a purpose-built holder positioned at one end. The VTI provides the housing for this and enables the sample's temperature to be governed by adjusting the rate at which helium gas flows. Helium enters at the base of the VTI via a needle valve with a heater used to warm the gas. The needle valve functions by the operator turning a screw and sits in the bath of helium around the VTI. The valve comprises a steel needle housed in brass with a pipe providing a connection to the VTI. Raising the tip of the needle causes helium to enter the pipe and, in turn, the VTI. Depending on the cryostat used, the helium can enter from different parts with certain manufacturers choosing to place the point of entry considerably closer to the sample. The heater is able to maintain a steady temperature. Whilst the roughing pump evacuates the VTI space, the void is filled by the helium that enters. Pumping achieves superior convection because when the helium is heated, it expands and is drawn in the direction of the sample.

The sample is subjected to magnetic fields by utilising a coil of superconducting wire to serve as a magnet. In order to guarantee uniformity, the sample is positioned at the midpoint of the magnetic field. In addition, a vacuum jacket provides insulation for the sample, thereby avoiding resources being wasted. There is a vacuum jacket encasing the entire cryostat to avoid unnecessary boil-off, whilst another jacket surrounds the VTI to help stabilise the temperature. The bath of liquid helium is surrounded by a liquid nitrogen jacket that serves as an insulator. At the upper section of the cryostat are metal plates to shield against cosmic rays and other types of electromagnetic radiation.

Measures of magnetoresistance, resistivity relative to temperature and other magneto-transport values were taken using the cryostat. In order to apply a lateral field, a split pair approach is utilised with a magnitude not exceeding 3T. To the housing around the stick is placed a stepper motor, thereby enabling the sample to be spun within the magnetic field. The apparatus incorporated a pressure gauge, thereby helping to ensure that the same conditions in the VTI were maintained. At a temperature of 290K, the pressure was 5mbar and whilst taking measurements, neither the pump nor the valve were altered.

As the sample was allowed to cool from 300K to 5K, measures of the sample's resistance were taken. Figure 3.11 demonstrates how resistance of the Pt/YIG bilayer declined as the temperature fell in a manner similar to how metal behaves.

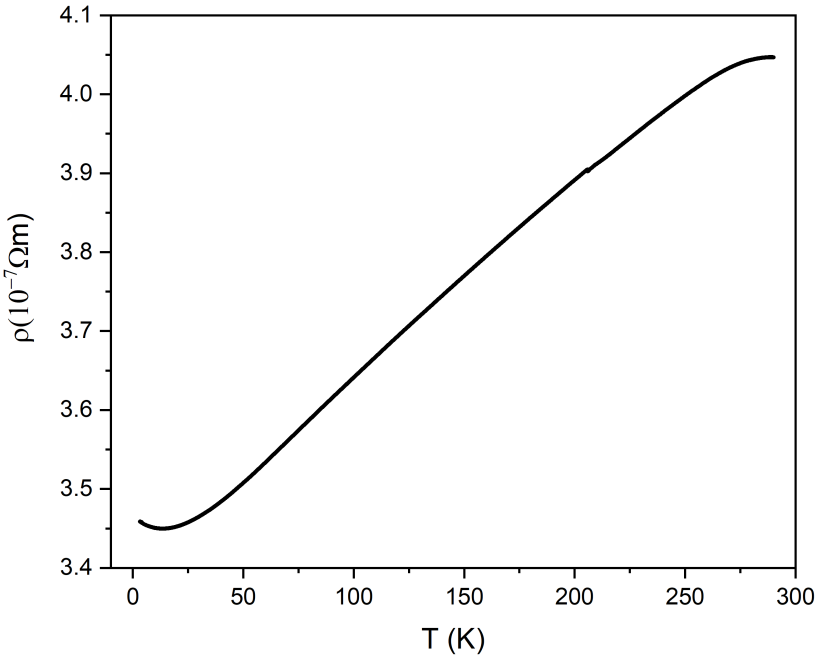

Figure 3.11: : The relationship between temperature and Resistivity for 2nm of Pt on 40nm of YIG.

3.6.1 Magnetoresistance Measurements

Figure 3.12 illustrates the various measurement planes when gauging magnetoresistance (MR). It is usually the case that a magnetic field will be swept in a certain direction when measuring MR and this usually occurs along the axes shown in the figure. To the x-axis is applied the jc charge current. Meanwhile, a field is applied along the x-axis running parallel to the current for the purposes of longitudinal MR. In addition, a field is applied along the y-axis running perpendicular to the current in the film's plane for the purposes of transverse MR. Finally, a field is applied to the z-axis to achieve perpendicular MR.

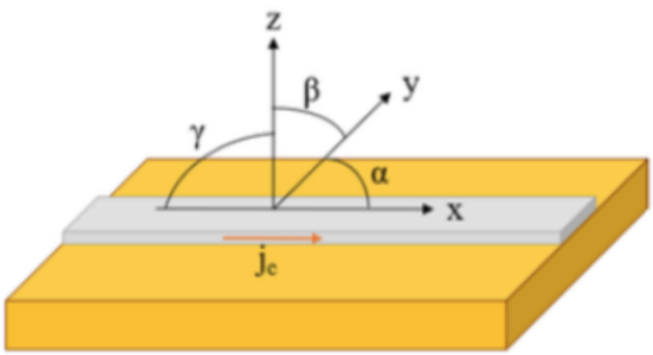

Figure 3.12: The terminology for the orientations and measuring planes required to take measurements of magnetoresistance in the current study. Along the x-axis is oriented the charge current (j_c). Among the x- and y-axes is the α-plane, among the y- and z-axes is the β-plane, whilst among the x- and z-axes is the γ -plane [159].

In figure 3.12, in α direction, the magnetisation of YIG changes with respect to the spin accumulation and any induce magnetisation into the Pt also changes relative to the current so in that case we have SHMR and AMR. In β direction, the magnetisation of YIG changes relative to the current but the magnetisation always perpendicular to the spin current so in that case there is no AMR we have only SHMR. In γ direction, the magnetisation changes relative to the current so there is AMR in that case but the magnetisation does not change relative to the spin accumulation so there is no SHMR.

Angle-dependent MR (ADMR) is also applied as a means of measuring MR in the current study. Taking this measurement requires the application of a constant field whilst rotating the sample to ensure the field traverses a certain plane (see Figure 3.12). If the field rotates in a longitudinal orientation (x-axis) and transverse orientations (y-axis), it is referred to as α-plane magnetoresistance. Meanwhile, if the field rotates in the transverse orientation (y-axis) and perpendicular orientation (z-axis), it is referred to as β-plane magnetoresistance.

Owing to the fact that the field and current are consistently perpendicular, it is possible to employ this orientation when measuring the spin Hall MR (SHMR), thereby eradicating anisotropic MR (AMR) from ferromagnetism. It is only in γ-plane magnetoresistance that AMR effects can be measured, where the field is consistently perpendicular relative to the spin orientation, resulting in the SHMR and ensuring that it is not possible to observe the SHMR. Amid the perpendicular and parallel orientations, the field rotates relative to the charge current, resulting in any AMR that is there becoming apparent.

Relative change in resistivity is applied when characterising the MR. Standard MR is given using the following equation:

$$\frac{\Delta\rho}{\rho_0} = \frac{\rho_{\max} - \rho_0}{\rho_0} \tag{3.10}$$

whereby $\rho_{\max}$ represents the level of resistance when the applied field is optimal, ρ_0 indicates resistivity when there is no applied field, and $\frac{\Delta\rho}{\rho_0}$ signifies the amount applied to calculate MR. The definition used with regard to ADMR is governed by the orientation because standard AMR and SHMR definitions are applied. To help keep things as simple as possible, $\frac{\Delta\rho}{\rho_0}$ is used to denote the quantity of ADMR but for the α-plane MR, its value is:

$$\frac{\Delta\rho_\alpha}{\rho_0} = \frac{\rho_x - \rho_y}{\rho_y} \tag{3.11}$$

whereby ρ_x represents the applied field's resistance when oriented longitudinally, and ρ_y is the applied field's resistance when oriented transversely. Regarding the β-plane MR:

$$\frac{\Delta\rho_\beta}{\rho_0} = \frac{\rho_z - \rho_y}{\rho_y} \tag{3.12}$$

whereby ρ_z represents the applied field's resistance when oriented perpendicularly. The definition used here is compatible with that applied in relation to the SHMR. Regarding the γ-plane MR:

$$\frac{\Delta\rho_\gamma}{\rho_0} = \frac{\rho_x - \rho_z}{\rho_z} \tag{3.13}$$

whereby the same definition of the resistivities is specified as with the alternative orientations. As such, for AMR $\rho_z > \rho_x \approx \rho_y$ whereas for SHMR: $\rho_x > \rho_y \approx \rho_z$ [104; 160; 161].

CHAPTER 4

YIG sample characterisation

4.1 Introduction

Yttrium iron garnet (YIG) film is a very interesting material for intensive research because of its complex crystal structure and magnetic properties [162]. The liquid phase epitaxy was the first method use to make single crystal YIG [163–165] . To develop the YIG thin films properties to be used in applications and make YIG more economical there are other methods that have been used, notably pulsed laser deposition (PLD) and sputtering techniques. LPE can make single crystals of very high quality but only on substrates which are not ideal and are difficult to make thin [166]. PLD is a good method to make high quality films of oxides. It is possible to control the oxygen stoichiometry because there are usually very small differences in composition between the target and the film and also by adjusting the oxygen pressure in the deposition chamber [101; 167; 168]. PLD can make stoichiometric YIG only when the substrate temperature was greater than 800 K [66; 168–170]. Recently more work has produced good films by cooling the film in oxygen in the growth chamber [6] or if they used a lower growth temperature of 650 K with a high temperature annealing [101]. Radio frequency (RF) magnetron sputtering is economical low temperature method and convenient compared with LPE [171]. It is easy to sputter insulator materials [172]. Because of oxygen vacancies the films grown by RF are usually off-stoichiometry [171].

In this chapter, we want to explore potential improvements in the growth of YIG. We report that the small changes at the interface can have significant effects to improve the structural and magnetic properties of YIG. Our YIG thin films are deposited on (111) oriented 0.5 mm thick GGG and YAG substrates by radio frequency (RF) magnetron sputtering and open air annealing at 850 C. X-ray reflectivity (XRR) and x-ray diffraction (XRD) were used to study the structural quality, lattice parameter, thickness of the YIG films. Atomic force microscopy (AFM) was used to study the surface roughness of the YIG films. Thin films were grown under the same deposition condition on two different substrates GGG and YAG with different thicknesses between 10 nm to 200 nm and subjected to an annealing process. Also, several samples of thin YIG films with the same thicknesses 40 nm were deposited with different contents of oxygen on the GGG and YAG substrates. There is an interface diffusion

between the film and substrate as part of the annealing process which can affect the structural and magnetic properties of the films. VSM and SQUID-VSM were used to investigate the magnetic properties of single crystal YIG films. It is important to determine the coercive field and the saturation magnetisation. The thickness of the dead layer is determined from the thickness dependence measurement by VSM. SQUID-VSM magnetometry was used in this work to measure the magnetic moment of the YIG samples in the wide temperature range from 2 K to 300 K. These measurements in VSM and SQUID-VSM were done for different thicknesses of YIG ranging from 10 nm to 200 nm. Also, the measurements in SQUID-VSM magnetometry were done for several samples of thin YIG films with the same thicknesses 40 nm were deposited with different contents of oxygen. At low temperature region in SQUID-VSM magnetometry measurements there is no magnetisation. From [173] they have recently shown that YIG grown on GGG, the favoured substrate for most, suffers from the problem of Gd – Y co-diffusion as part of the annealing process. From comprehensive TEM measurements as we see in figure 4.1 they have shown that this behaviour is vacancy driven and we suspect that this could be due to oxygen deficiency. We have used a variation in Oxygen pressure during sputtering to study the possible effects of reducing vacancies. At room temperature the interdiffused layer is non-magnetic i.e. a dead layer, as temperature is reduced, the Gd-based layer becomes magnetic and orders anti-parallel to the YIG – these effects are detected by Squid magnetometry as a function of temperature.

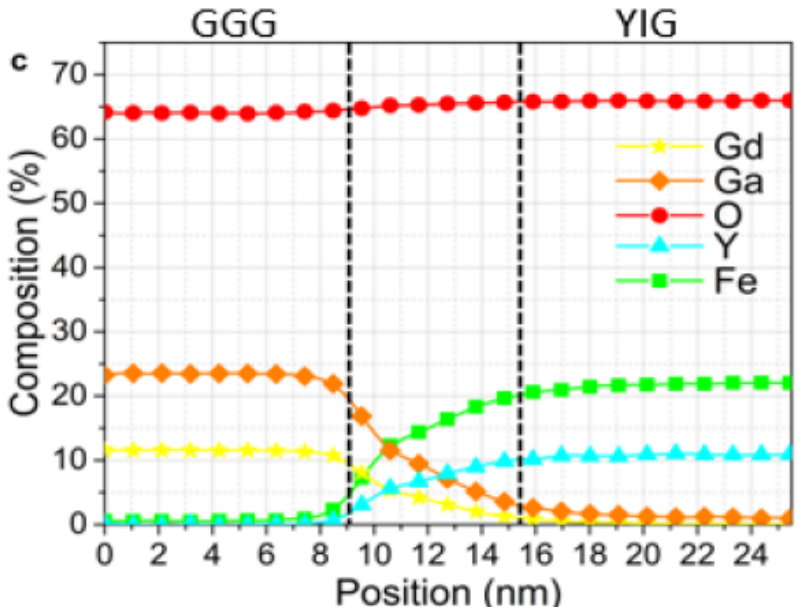

Figure 4.1: transmission electron microscopy scan show the behavior is vacancy driven [173].

4.2 Structural properties

4.2.1 X-ray reflectivity

In this section, X-ray reflectivity was used to study the structural properties of thin YIG films in this section. This tell us about the thickness and growth rate, surface roughness and the density.

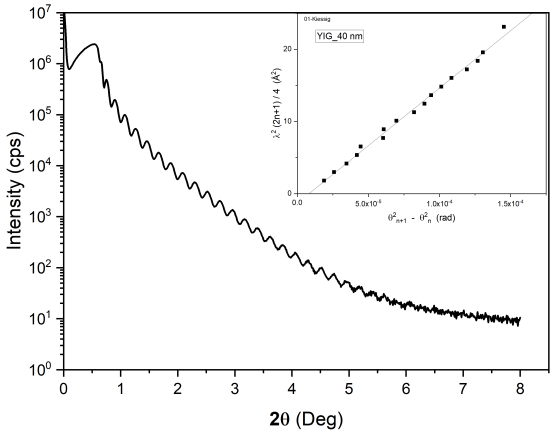

(a)

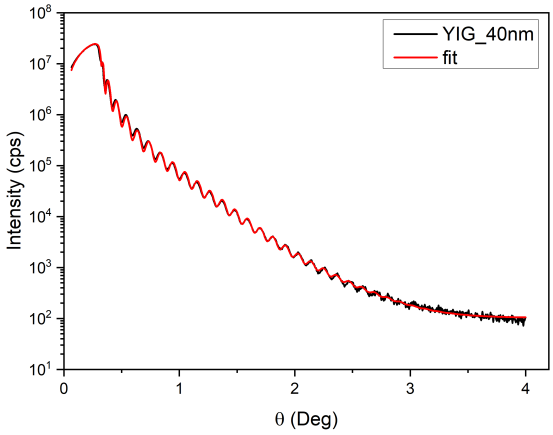

(b)

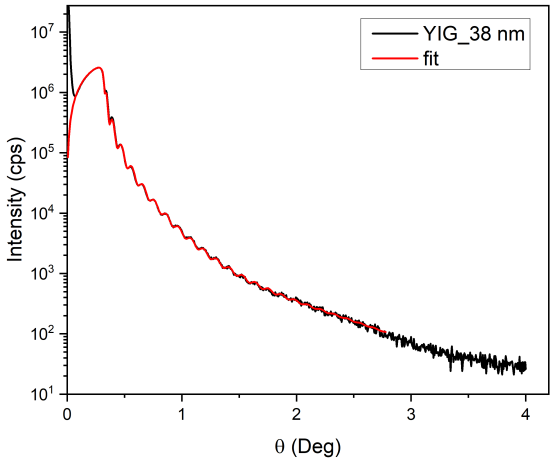

(c)

Figure 4.2: X-ray reflectivity YIG on GGG before annealing (a) and good fit by using Bede software in (b) (40 nm) before annealing. XRR for YIG (38 nm) after annealing for the same sample (c).

Figure 4.2(a) shows the x-ray reflectivity ($CuK\alpha, \lambda$ = 1.54 Å radiation) of 40 nm YIG film before annealing. The angular positions of the Kiessig fringes (inset of figure 4.2(a)) were used to determine the thickness by using equation 3.4. Figure 4.2(b) shows that the Bede software was used to fit the X-ray reflectivity (XRR) curve and get more information about the chemical nature of the YIG on GGG. We measured the thickness of YIG films before and after annealing. We found the films decreased by a very small amount. For example this film in figure 4.2(b) was (40 nm) before annealing and (38 nm) after annealing in figure 4.2(c). The slow exponential decay of the reflectivity curve indicates a smooth surface of the YIG after annealing.

To have more information about the chemical structure of the films the Bede software used to fit the reflectivity curves. We have sputtered four samples for 3500s with changing the oxygen contents during the sputtering 5 %, 5.5 %, 6 %, and 6.5 %. The reflectivity curves before and after annealing are fitted using the Bede software. A much better fit for the reflectivity curves after annealing when we include an additional layer which is Gd at the interface. The dead layer thickness can be changed by changing the Oxygen contents during sputtering as we see in figure 4.3(d). We have a good fit with the goodness of fit (GOF = 0.05). The parameters from the fitting for each samples before and after annealing are shown in figure 4.3.The parameters can be changed by changing the oxygen contents during the sputtering. As we see from the figure 4.3(a) the thickness is increased by increasing the oxygen contents. Also, the thicknesses for the unnealed samples are thinner than the thicknesses before annealing in the same figure. Figure 4.3(b) shows that the roughness can be changed by changing the oxygen contents, the smoothest sample is the sample with 6 % of oxygen. The samples after annealing are smother than before annealing (see figure 4.3(b). The density from the fit for our samples was changed by changing the oxygen contents, the lowest density for the sample which has 6 % of oxygen and the highest density was for the sample with 5 % of oxygen (see figure 4.3(c).

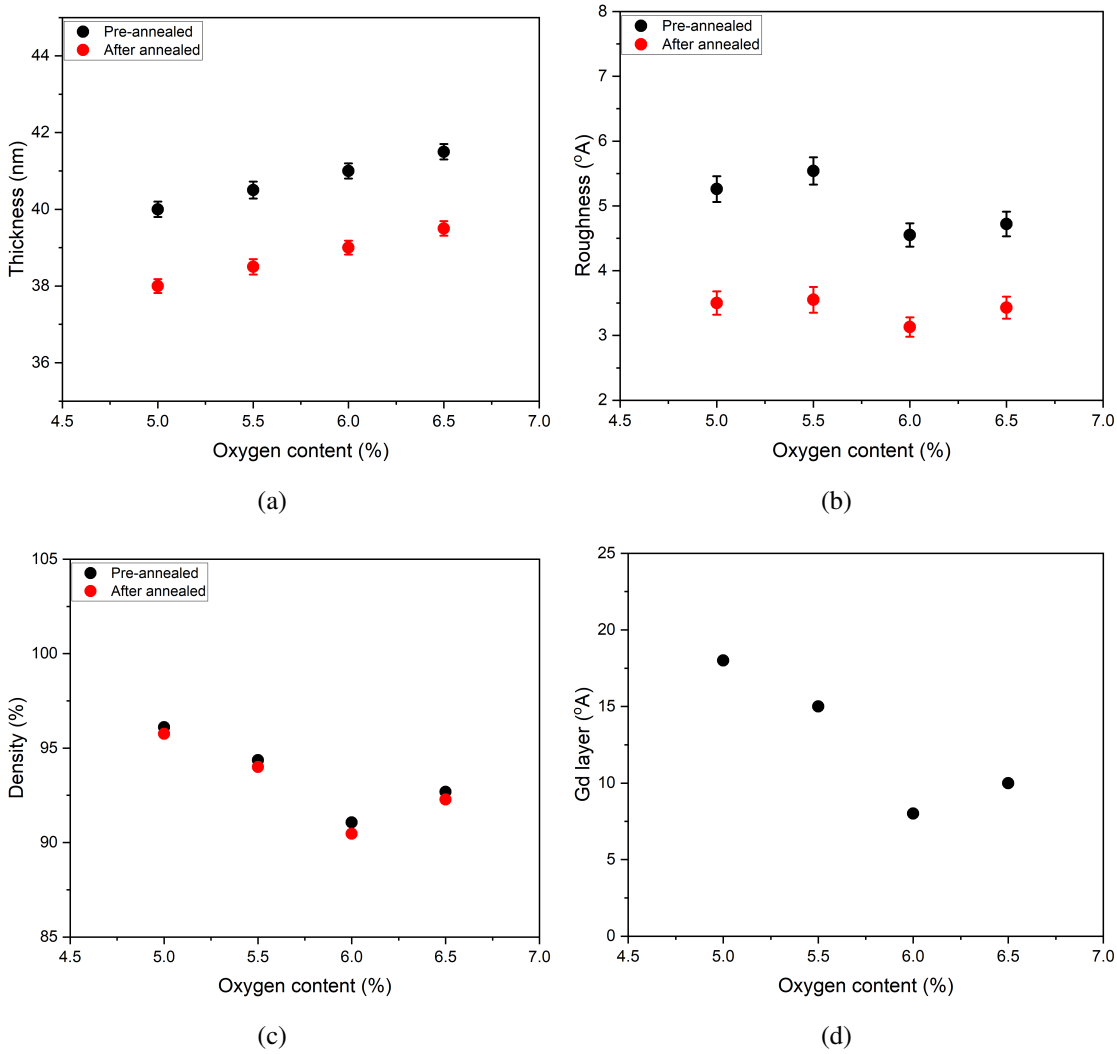

Figure 4.3: Parameters used to fit the x-ray reflectivity data for unnealed (40 nm) and annealed YIG (38 nm), the fit is shown in figure 4.2.

4.2.2 Crystal properties

In this work XRD measurements used to determine the lattice constant and the crystalline orientation of YIG. Also, we used the XRD measurements for a deeper insight into the structural of the film. A high angle XRD scan was taken around the GGG $< 444 >$ peak. In [129] they showed that the YIG peak continued to increase until 850 °C for two hours. The YIG film was annealed up to 1000 °C for 24 hours but no difference was determined compared to annealing for 2 hours at 850 °C [129]. The annealing was done by tube furnace at 850 °C for 2 hours in air to make sure we have good crystallisation.

Figure 4.4(a) shows the high angle scan for YIG sample before annealing, we only can see the GGG substrate peak because the as-deposited YIG samples are nanocrystalline or maybe amorphous. Figure 4.4(b) shows the high angle scan for annealed (100nm YIG) samples with different oxygen content during sputtering. The lattice constant for 100nm with 5 % of oxygen content (red line) is 12.328 $\pm$ 0.002 Å compared to a bulk value of 12.376 Å, the lattice constant for 100nm with 6.8 % of oxygen content (blue line) is 12.401 $\pm$ 0.002 Å. The 100nm YIG sample with 6.2 % of oxygen content (green line) we could not determine the lattice constant because part of YIG peak is hidden under the GGG substrate peak and is therefore assumed to be the same as the bulk as YIG and GGG lattice constants differ by only 0.016 %.

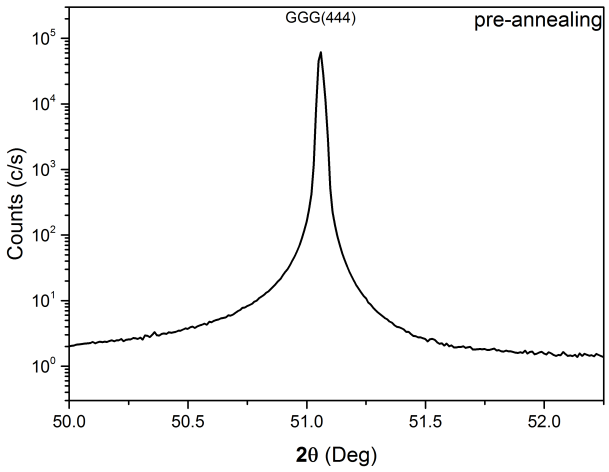

(a)

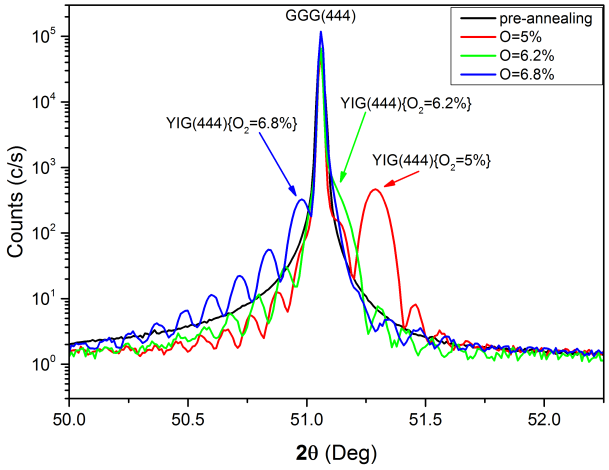

(b)

Figure 4.4: X-ray diffraction scan for YIG sample before annealing (a). X-ray diffraction scans annealed (100 nm) YIG samples with different oxygen content during sputtering (b).

Several samples with different thicknesses were grown with 5 % of oxygen content. All samples were subjected to high angle scans at each stage of the YIG preparation. The annealing is necessary for any crystal structure to be formed as seen in figure 4.5. The location of the peak is not in the expected place for the bulk lattice constant. For

all samples prepared with 5 % of oxygen content on GGG, the YIG peak is at a higher angle than the bulk position.

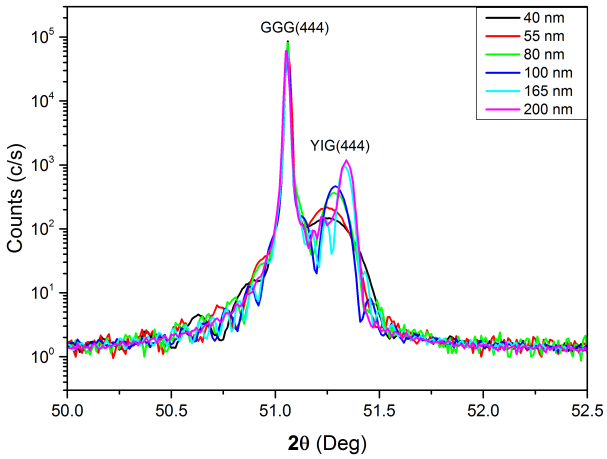

(a)

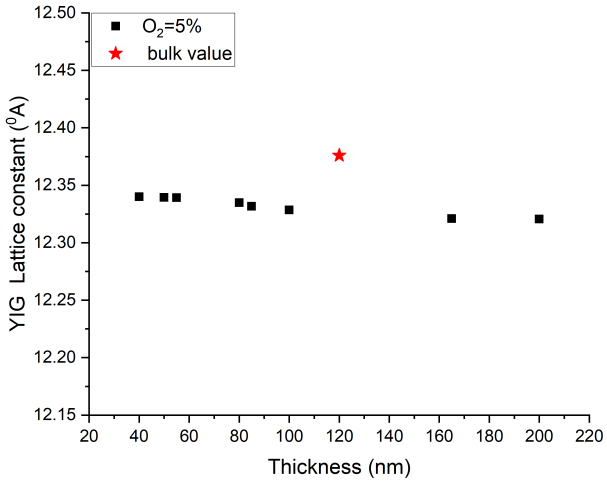

(b)

Figure 4.5: X-ray diffraction scan for YIG samples with 5 % oxygen content during sputtering after annealing. The YIG has a(111)crystalline orientation. Intensity of the YIG peak varies as a function of thickness(a). The lattice constant (a_o) as a function of thickness of the YIG samples with 5 % oxygen content during sputtering compared to the bulk YIG lattice constant 12.376 Å(b).

YIG samples with different thicknesses were grown with 6.8 % of oxygen content. The location of the peak is not in the expected place for the bulk lattice constant. For all samples prepared with 6.8 % of oxygen content on GGG, the YIG peak is at a lower angle than the GGG.

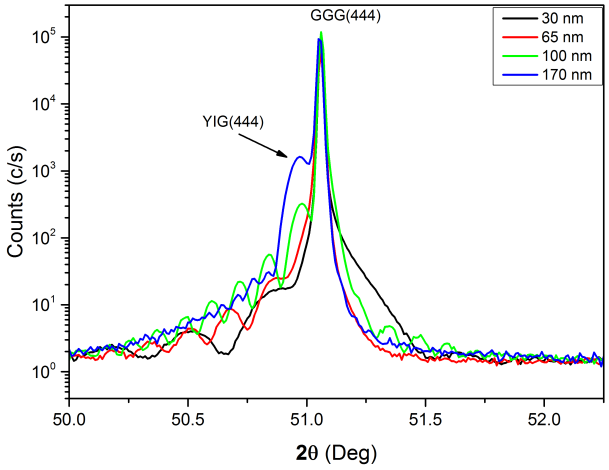

(a)

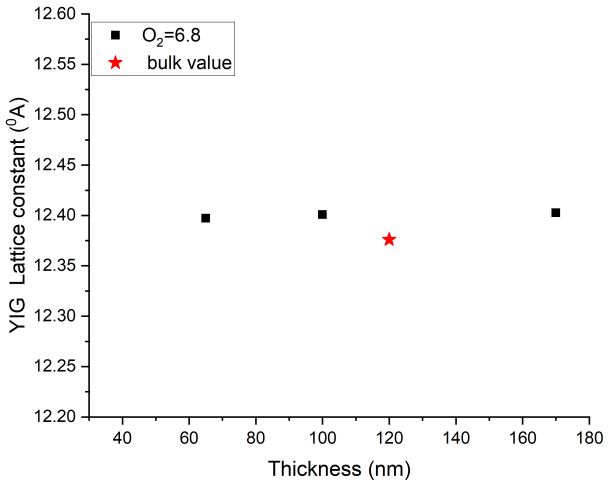

(b)

Figure 4.6: X-ray diffraction scan for YIG samples with 6.8 % oxygen content (a). The lattice constant (a_o) as a function of thickness of the YIG samples with 6.8 % oxygen content during sputtering compared to the bulk YIG lattice constant 12.376 Å(b).

For YIG films were grown With 6.2 % of oxygen content, the YIG peak positions in the x-ray diffraction spectrum are much closer to the YIG bulk position and have a very high quality with a lattice constant which agrees with the bulk value of YIG lattice constant (12.376 Å) as we see in figure 4.7

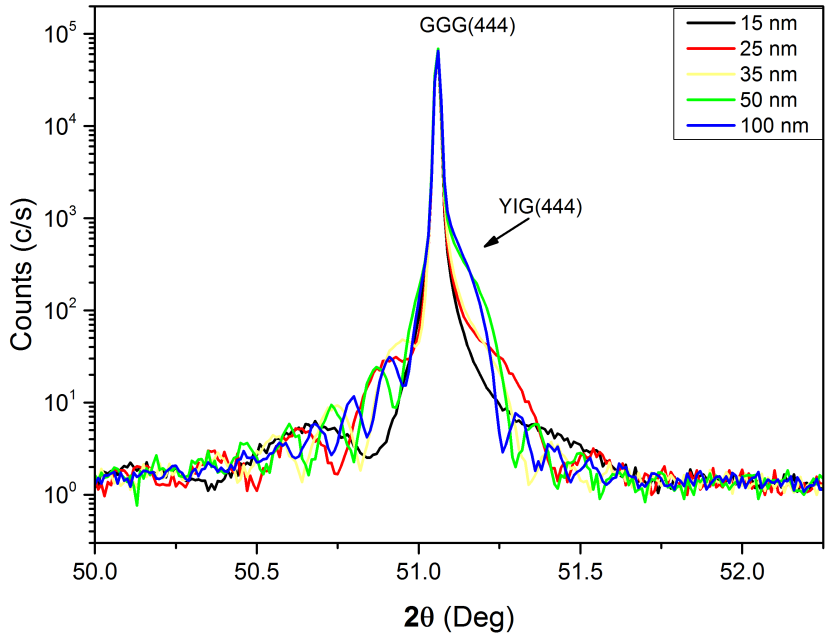

Figure 4.7: : X-ray diffraction scan for YIG samples with 6.2 % oxygen content during sputtering after annealing. The YIG peak is closer to the bulk YIG peak.

Figure 4.7 shows the high angle scan for YIG samples were grown with 6.2 % of oxygen content, we can see the location of the YIG peak is close to the expected place for the bulk lattice constant.

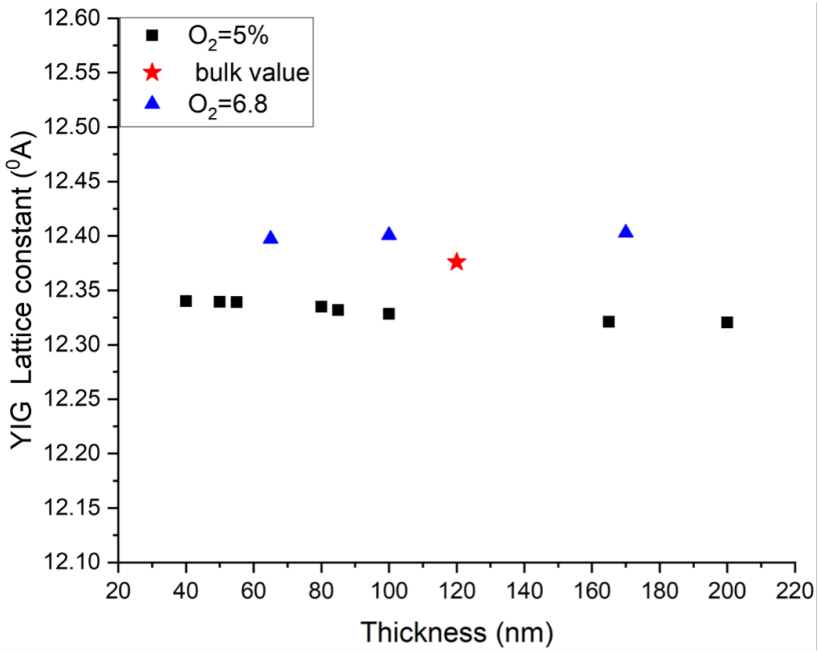

Figure 4.8: : The lattice constant (a_o) as a function of thickness of the YIG samples were grown with different oxygen content during sputtering compared to the bulk YIG lattice constant 12.376 Å.

The location of the YIG (444) peak can be moved by changing the contents of oxygen. When the oxygen was 5 % the YIG peaks have appeared on the right side of the GGG peak. When the oxygen was 6.2 % the location of the YIG peaks are close to the expected place for the bulk lattice constant. When the oxygen was 6.8 % the YIG peaks have appeared on the left side of the GGG peak.

4.2.3 Morphology

In this section, atomic force microscopy was done on the annealed 40 nm YIG on GGG to study the surface roughness. The surface morphology measurement was done in tapping mode in air. Two scan size $(1\mu m, 5\mu m)$ were used to scan the surface roughness on many different area

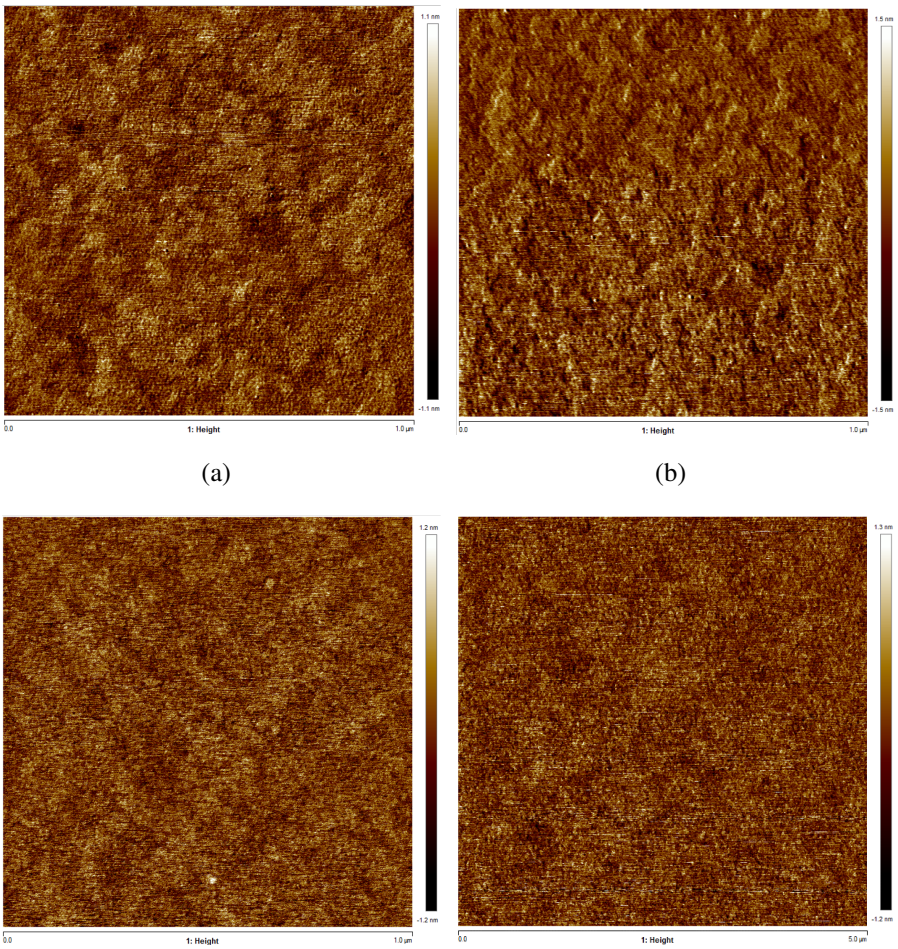

(a) (b)

(c) (d)

Figure 4.9: : AFM Surface scan of annealed 40 nm thin films (YIG on GGG). The scan size was about 1μ m. Those films were growing with different content of oxygen 5 % in (a) 5.5 % in (b) 6 % in (c) and 6.5 % in (d).

AFM measurements after annealing show how the surface roughness is dependent

on the oxygen content during sputtering. Figure 4.10 shows the comparison of those different oxygen contents. From the plot the roughness values we see that the 6 % oxygen provides the smoothest YIG after annealing.

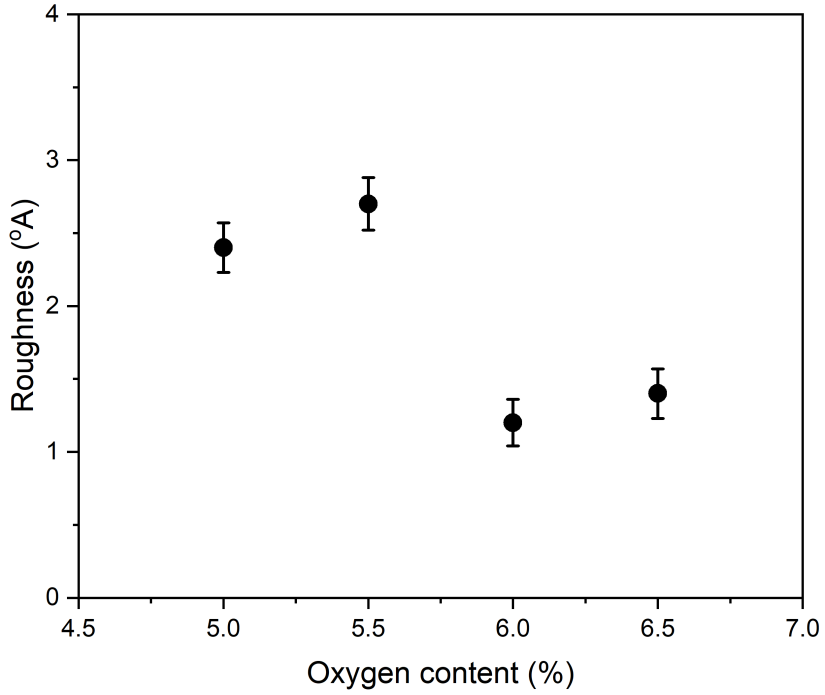

Figure 4.10: : The roughness from AFM scan of annealed 40 nm YIG on GGG after annealing with a different oxygen content in the sputtering atmosphere. The smoother film is found with 6 % oxygen content.

The smoothest YIG after annealing was found when the YIG films were deposited with 6 % oxygen content. The reason for the increased roughness for other oxygen content is not understood but I think it is more likely that when the oxygen vacancies are not filled, it means the surface will be rougher.

From the AFM scan and the parameters that we used to fit the XRR data for the same samples, the smoothest film in AFM and Bede fit was the sample which has 6 % of oxygen. The result from AFM were smoother than the parameters that we used in the fitting as we see in figure 4.11.

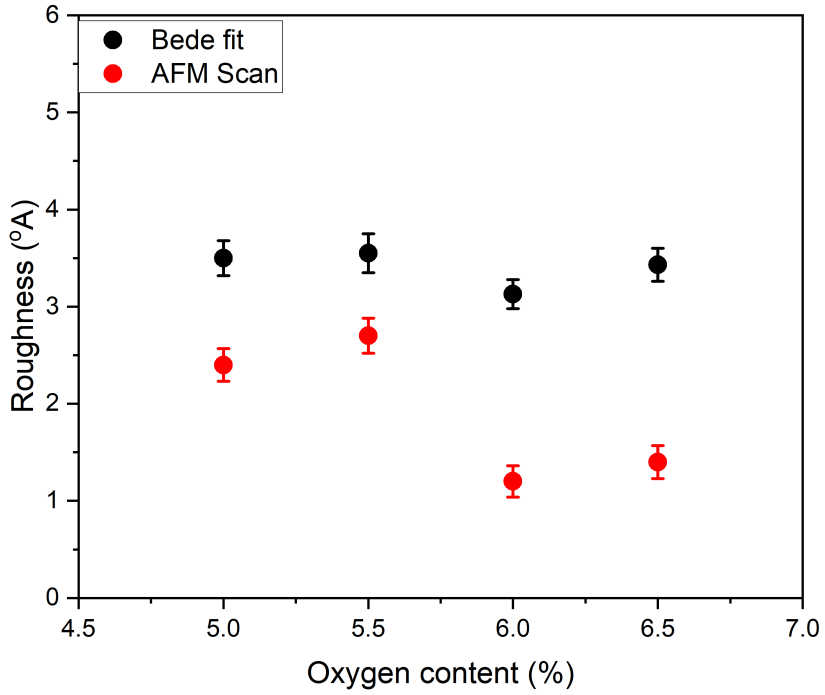

Figure 4.11: : The roughness of YIG on GGG after annealing with a different oxygen content in the sputtering atmosphere. Red points from AFM scan. Black points from parameters used in fitting. The smoother film is found with 6 % oxygen content.

4.3 Magnetisation properties

4.3.1 Thickness dependent magnetic properties

In this section, Vibrating sample magnetometer (VSM) was used to study the thickness dependent magnetic properties of YIG on (111) GGG substrate. The YIG films were grown with three different contents of oxygen. An array of magnets attached to the shutter wheel help us to set the direction of easy axis of our samples during the growth. The substrate sits at the centre of these magnets during the deposition. We determined the net magnetic moment (m) and the coercivity (H_c) from the hysteresis loops as a function of applied field at 295 K. The magnetic field was applied in plane along the easy axis of the sample.

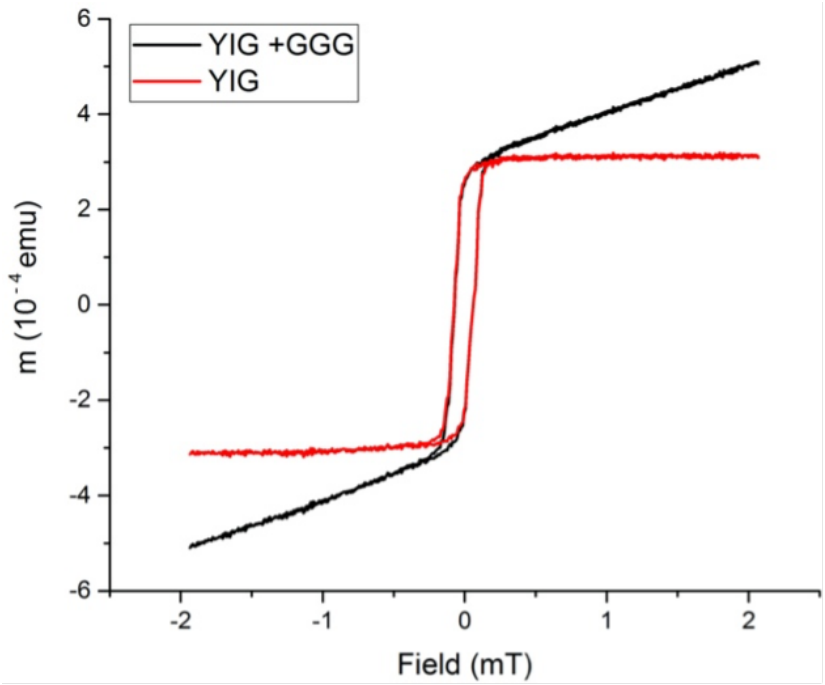

Figure 4.12: : The black curve shows the net magnetic moment of a 100 nm YIG on GGG substrate versus in plane magnetic field at 295 K. The magnetic moment as a function of applied magnetic field after the subtraction the paramagnetic contribution from the GGG substrate(red curve).

Figure 4.12 shows that the paramagnetism from the Gd^{3+} ions in the GGG substrate is dominating the signal of the thin film of YIG generating a large background signal (black curve). The red curve shows the typical dependence of the magnetic moment versus in plane magnetic field of a 100 nm YIG on GGG at 295 K.

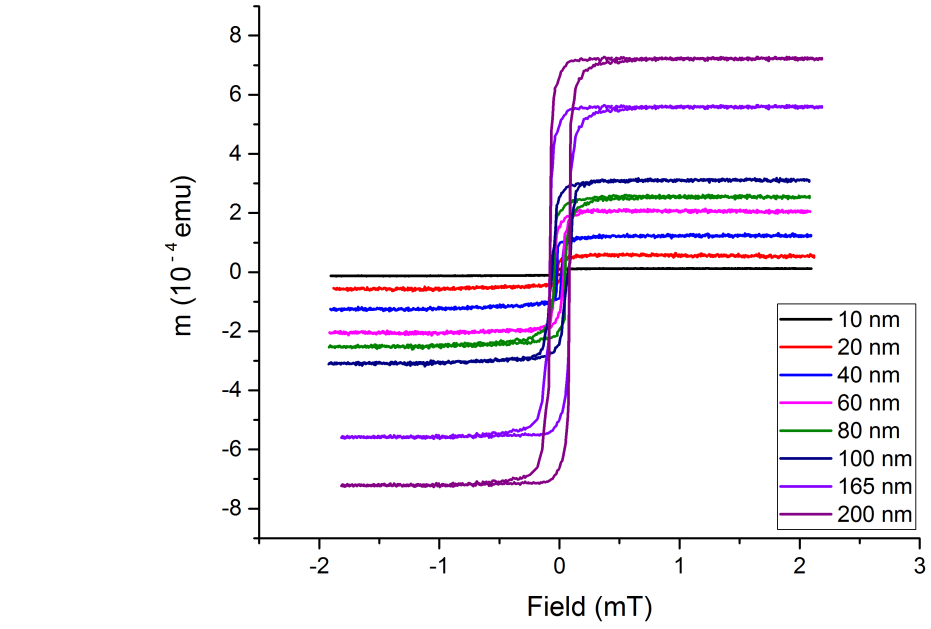

(a)

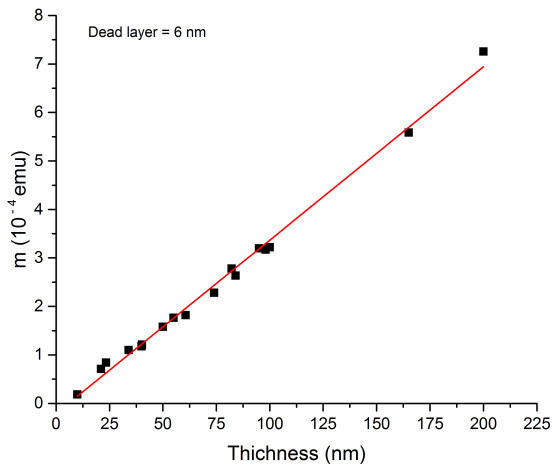

(b)

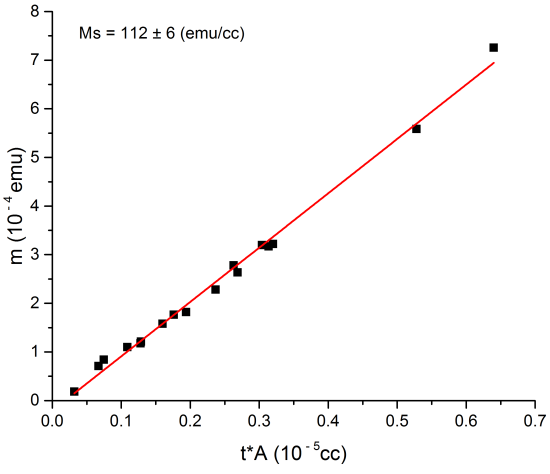

(c)

Figure 4.13: Magnetic moment as a function of applied field at room temperature for different thicknesses of YIG with 5 % oxygen content during sputtering. The data shows that the YIG is soft and the coercivity of our films is 0.67 $\pm$ 0.05 Oe (a). The linear extrapolation of the saturation magnetic moment as a function of thickness shows that there is a dead layer of about 6 nm (b) which agreed with the results from [173]. (c) The linear extrapolation of the saturation magnetic moment as a function of thickness times area shows the $M_s = 112 \pm 6$ emu/cc.

Different thickness of YIG ranging from 10 nm to 200 nm were grown with 5 % of oxygen content during sputtering. Figure 4.13(a) shows the hysteresis loops for different thickness of YIG after the subtraction of the paramagnetic contribution from the GGG substrate at room temperature. Also, from the hysteresis loops the coercivity of samples is 0.67 ± 0.05 Oe. Figure 4.13(b) shows that the linear extrapolation of the saturation magnetic moment versus thickness shows the thickness of the diffusion between the YIG and GGG substrate, which called a dead layer is about 6 nm. The magnetization can be found from the measured magnetic moment by determining the thickness of each sample and using the sample volume. The saturation magnetisation obtained from the slope is M_s =112 $\pm$6 emu/cc, compared to the bulk value M_s = 143 emu/cc at room temperature.

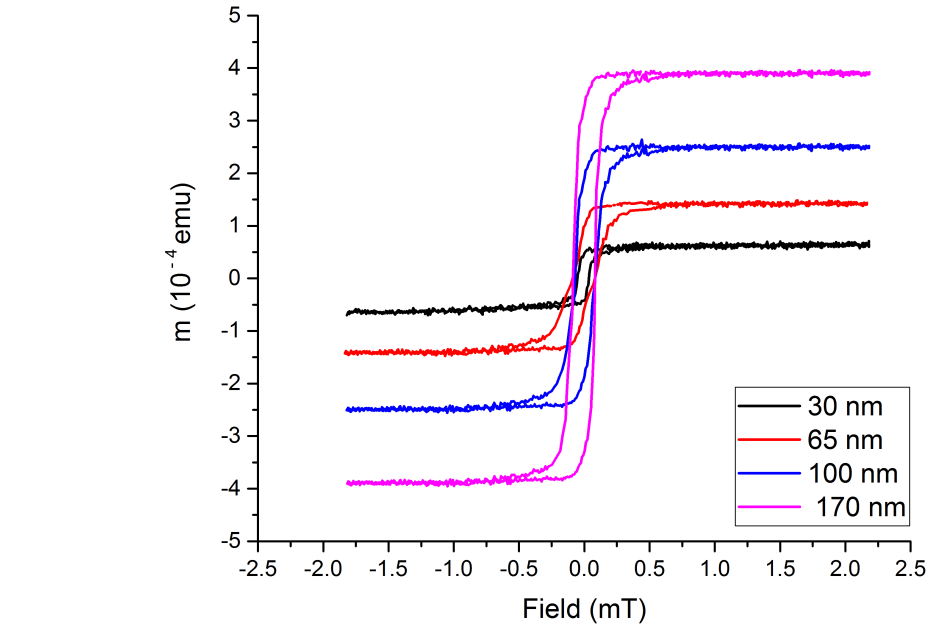

(a)

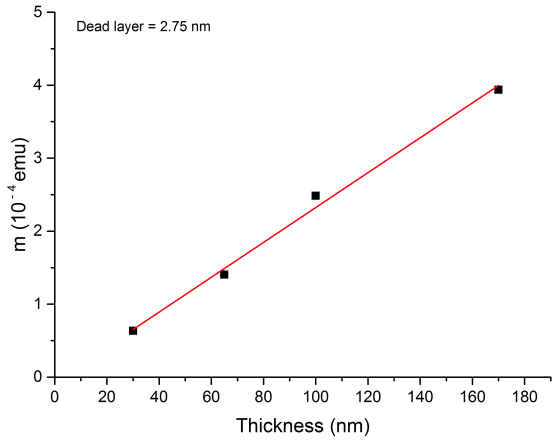

(b)

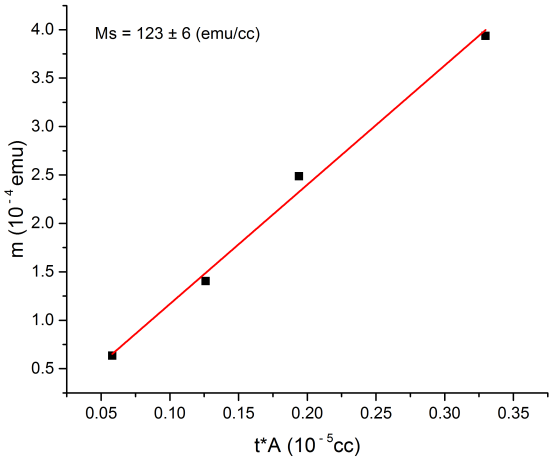

(c)

Figure 4.14: Magnetic moment as a function of applied field at room temperature for different thicknesses of YIG with 6.8 % oxygen content during sputtering. The data shows that the YIG is soft and the coercivity of our films is 0.78 $\pm$ 0.05 Oe (a). The linear extrapolation of the saturation magnetic moment as a function of thickness shows that there is a dead layer of about 2.75 nm (b). (c) The linear extrapolation of the saturation magnetic moment as a function of thickness times area shows the $M_s = 123 \pm 6$ emu/cc.

Next, different thickness of YIG ranging from 30 nm to 170 nm were grown with 6.8 % of oxygen content during sputtering. Figure 4.14 (a) shows the hysteresis loops for different thickness of YIG after the subtraction of the paramagnetic contribution from the GGG substrate at room temperature. Also, from the hysteresis loops the coercivity of samples is 0.78 ± 0.05 Oe. Figure 4.14 (b) shows that the linear extrapolation of the saturation magnetic moment versus thickness shows the thickness of the diffusion between the YIG and GGG substrate, which called a dead layer is about 2.75 nm. The magnetization can be found from the measured magnetic moment by determining the thickness of each sample and using the sample volume. The saturation magnetisation obtained from the slope is M_s =123 $\pm$6 emu/cc, compared to the bulk value M_s = 143 emu/cc at room temperature.

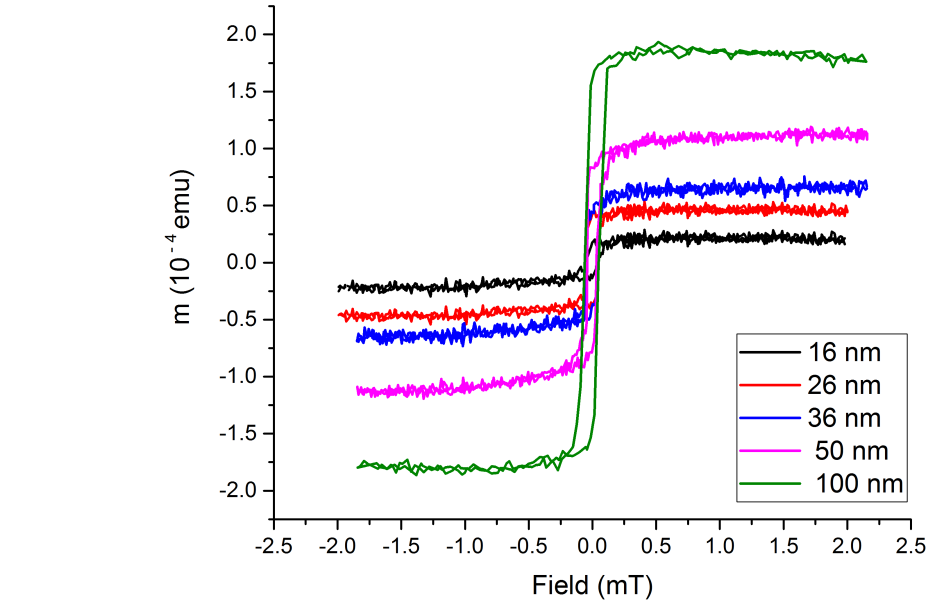

(a)

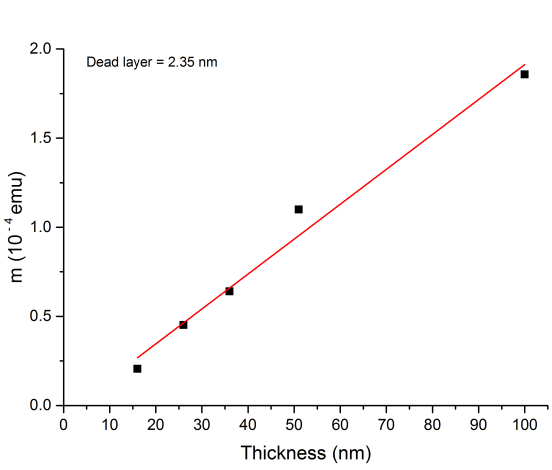

(b)

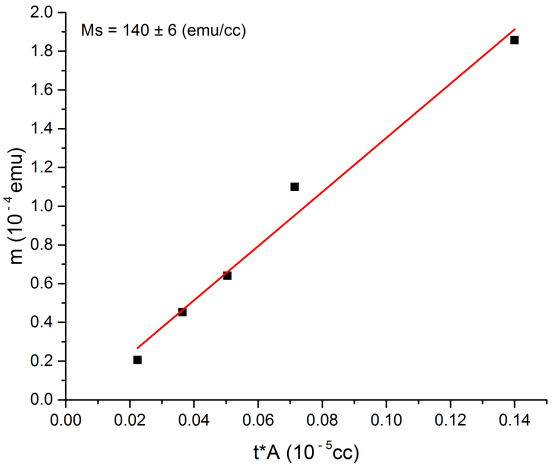

(c)

Figure 4.15: Magnetic moment as a function of applied at room temperature for different thicknesses of YIG with 6.2 % oxygen content during sputtering. The data shows that the YIG is very soft and the coercivity of our films is 0.38 ± 0.05 Oe (a). The linear extrapolation of the saturation magnetic moment over area as a function of thickness shows that there is a dead layer of about 2.35 nm (b). (c) The linear extrapolation of the saturation magnetic moment as a function of thickness times area shows the M_s $=140$ ± 6 emu/cc

After when we see that the YIG films can be improved by changed the oxygen content during sputtering as we grew mor sampleas with 6.2 % of oxygen content. these samples were grown with different thickness of YIG ranging from 16 nm to 100 nm. Figure 4.15 (a) shows the hysteresis loops for different thickness of YIG after the subtraction of the paramagnetic contribution from the GGG substrate at room temperature. Also, from the hysteresis loops the coercivity of samples is 0.38 ± 0.05 Oe. Figure 4.15 (b) shows that the linear extrapolation of the saturation magnetic moment versus thickness shows the thickness of the diffusion between the YIG and GGG substrate, which called a dead layer is about 2.35 nm. The magnetization can be found from the measured magnetic moment by determining the thickness of each sample and using the sample volume. The saturation magnetisation obtained from the slope is M_s =140 $\pm$6 emu/cc, which agrees with the bulk value M_s = 143 emu/cc at room temperature.

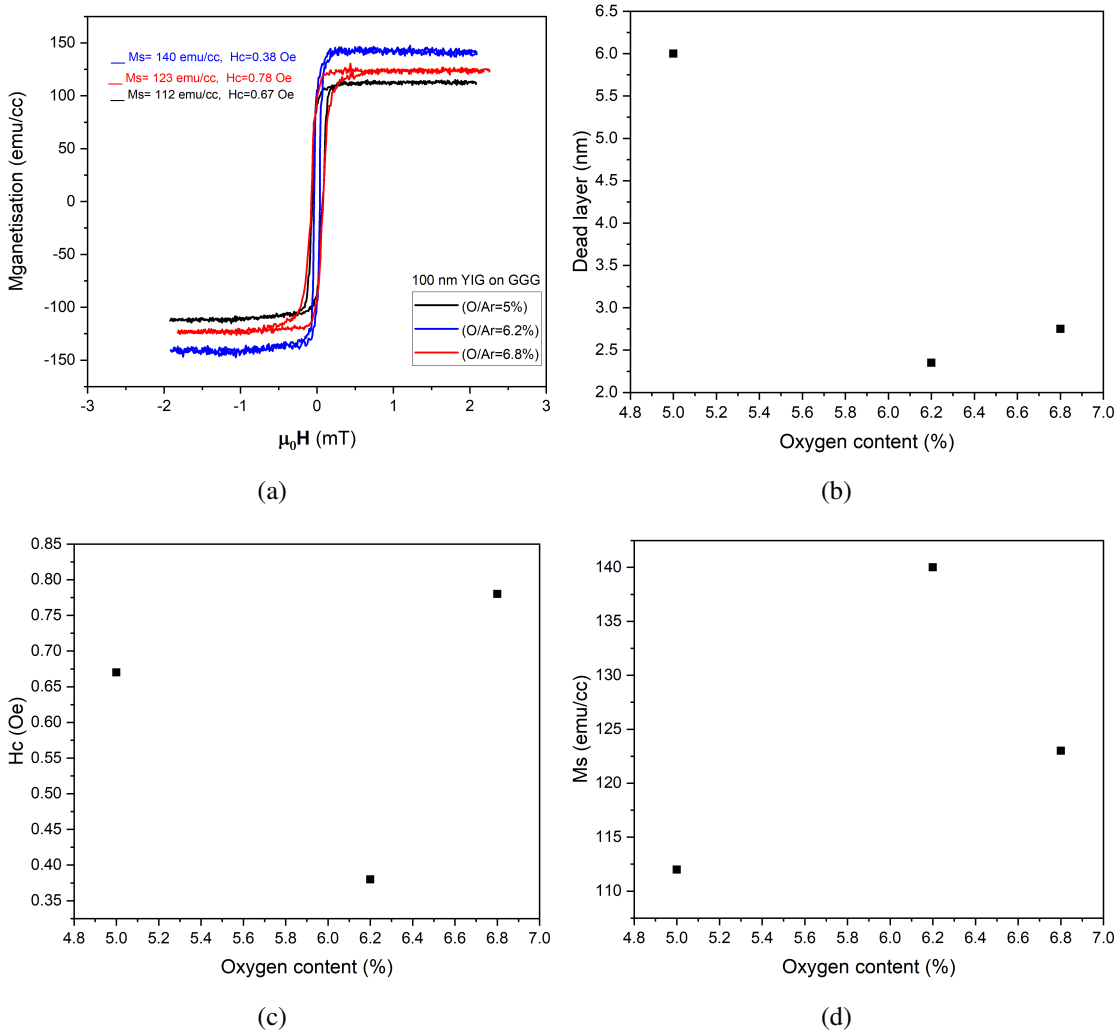

Figure 4.16: The saturation magnetisation as a function of applied field at room temperature for annealed 100 nm YIG with different oxygen content during sputtering (a). The dead layer at YIG/GGG interfaces as a function of oxygen growth content (b). Coercive field (H_c) of YIG as a function of oxygen growth content (c). The saturation magnetisation (M_s) for YIG as a function of oxygen growth content (d).

Figure 4.16 shows that the magnetic properties of YIG film can be improved by changing the contents of oxygen. Figure 4.16 (a) shows the saturation magnetisation at room temperature for 100 nm of YIG on GGG depends on the oxygen growth content.

The saturation magnetisation from the hysteresis loop is M_s =112 $\pm$6 emu/cc when the oxygen was 5 % and M_s =123 $\pm$6 emu/cc when the oxygen was 6.8 %, compared to the bulk value M_s = 143 emu/cc at 295K. When the oxygen was 6.2 % the saturation magnetisation from the hysteresis loop is M_s =140 $\pm$6 emu/cc, which agrees with the bulk value M_s = 143 emu/cc at room temperature. Figure 4.16 (b) demonstrates that the thickness of the inter-diffused dead layer can be changed with changing the O/Ar %, therefore greatly improving the magnetic properties of thin film RF sputtering YIG. The dead layer is the thinnest at 2.35 nm when the oxygen was 6.2 % and thickest at 5 % with a 6 nm dead layer. Figure 4.16 (c) shows the coercive field is found to become smallest at 0.38 Oe when the oxygen was 6.2 %. There is a very small difference between the largest coercive field and smallest by changing the oxygen growth content, the different between them is about 0.4 Oe. For PLD-grown YIG film in reference [101] the H_c value (2 Oe) is about 10 times larger than our H_c. Also, in reference [174] which is 15-30 Oe for different YIG thicknesses about 100 times larger than our H_c.

4.3.2 Temperature dependence of magnetisation

In this section, SQUID-VSM magnetometry was used to measure the magnetic moment of the YIG samples on GGG in the wide temperature range from 2 K to 300 K. The measurements in SQUID-VSM magnetometry was done for the same thicknesses (40 nm)YIG films were deposited with different contents of oxygen.Thin sample could help us to measure the effect of Gd from GGG diffused into the YIG after annealing. The M(T) curve can show a compensation point is different when we changed the oxygen contents during sputtering. The magnetic field was applied in plane along the easy axis of our samples.

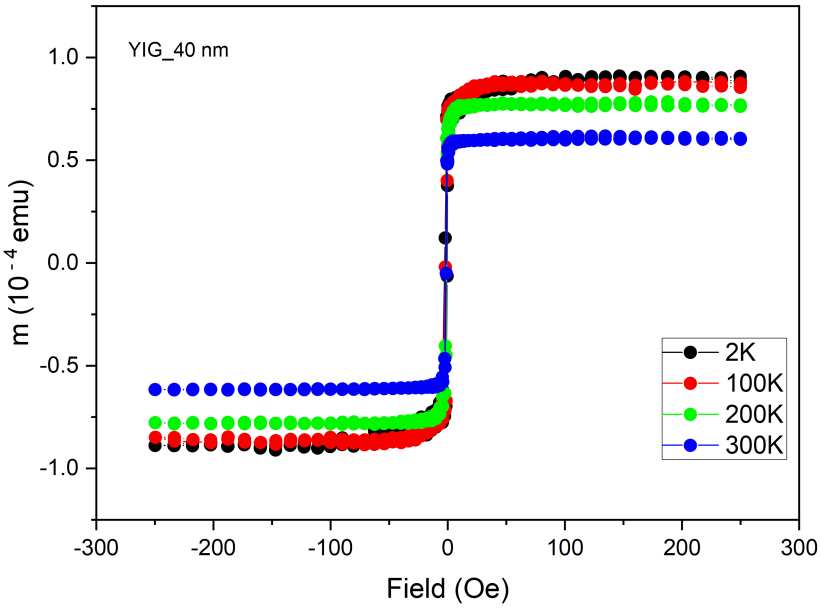

Figure 4.17: : Hysteresis loops as a function of applied field for 40 nm YIG at different temperatures. with decrease in temperature, the paramagnetic background from the GGG increase.

Figure 4.17 shows the hysteresis loops for 40 nm thick of YIG after the subtraction of the paramagnetic contribution from the GGG substrate at different temperatures. To ensure that the sample was saturated we applied magnetic field (H) from -250 Oe to 250 Oe. The magnetic moment was calculated from the hysteresis loops by correcting the linear paramagnetic slope at each temperature. These measurements were done for the same thickness of YIG films with different growth oxygen contents to obtain the magnetisation curve for each sample.

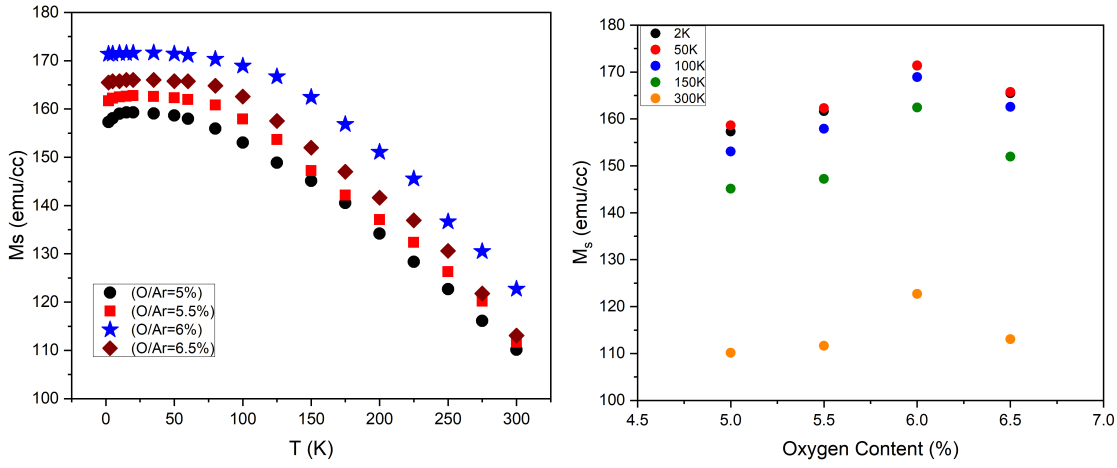

(a) (b)

Figure 4.18: The temperature dependence of the saturation magnetisation for 40 nm YIG on GGG with different contents of oxygen during sputtering. There is a decrease of M(T) at low temperature region in sample with 5 % and small decrease with other samples in varying proportions. (a) . The saturation magnetisation (M_s) for 40 nm YIG at different temperature as a function of oxygen growth content (b).

The saturation magnetisation as a function of temperature M(T) for 40 nm YIG thickness with different contents oxygen during sputtering is plotted in figure 4.18. At the low temperature region shows a decrease in magnetisation with decrease in temperature in sample with 5 % oxygen content and small decrease with other samples in varying proportions. The probable explanation on the decreases of magnetisation (ΔM) at low temperature due to the diffusion of Gd from the GGG substrate into the YIG. As part of the annealing process at high temperature will substitutes Gd for Y to form either Gd-doped YIG or Gd-rich YIG layer at the YIG/GGG interface. From the VSM data at room temperature, we obtained that the dead layer thickness can be changed by changing the oxygen growth content. The thinnest thickness of dead layer is 2.35 nm when the oxygen was 6.2 % and thickest at 5 % with a 6 nm thickness as shown in (fig.4.16 b). Our results show much improvement which shows that downturn in magnetisation in the low temperature region is very small compare to the results in [173] as we see in figure 4.19.

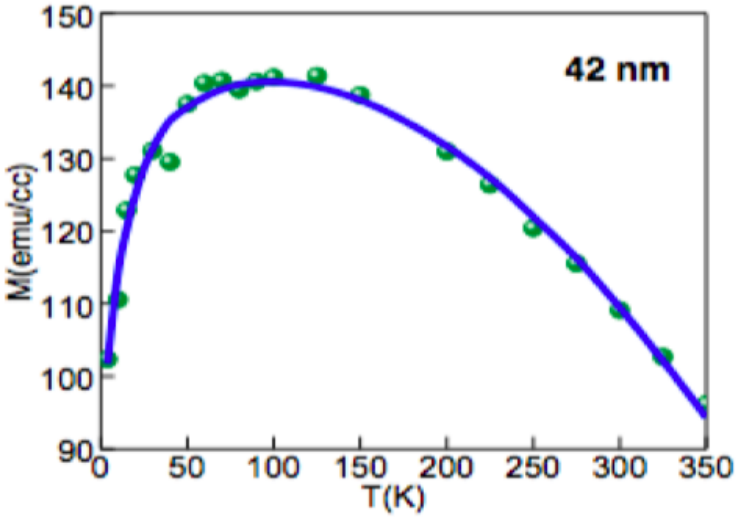

Figure 4.19: Temperature dependence of magnetisation for a 42 nm of YIG film thickness shows a decrease in magnetisation with decrease in temperature at the low temperature region [173].

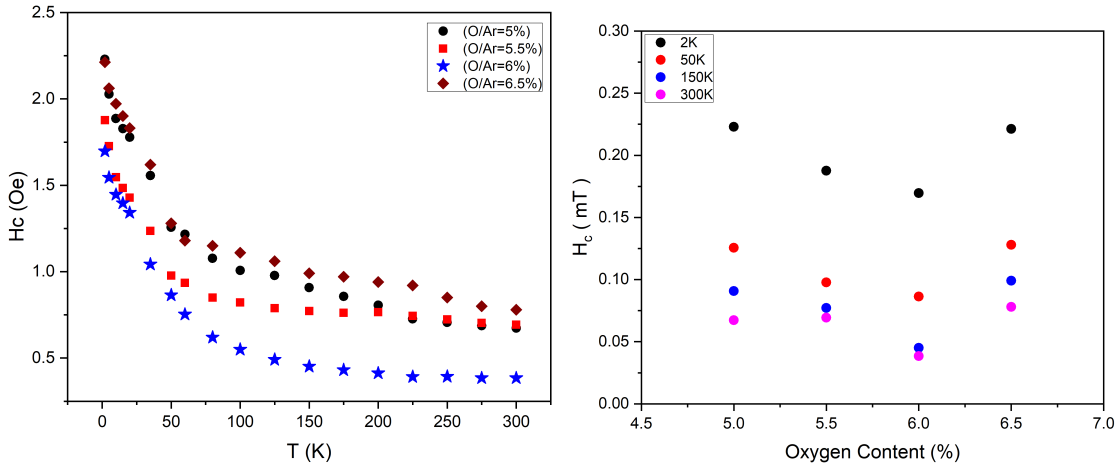

(a) (b)

Figure 4.20: The temperature dependence of the coercive field H_c (T) shows widening at lower temperatures regions as expected and having breaking point around 50 K(a). This data for 40 nm annealed YIG samples were grown with different contents of oxygen. Coercive field of 40 nm YIG as a function of oxygen growth content at different temperatures(b).

From our data, we observed a small change of the coercive field by changing the growth oxygen contents. The coercive field becomes larger with decreasing temperature. This data show that the YIG is very soft. The coercive field is important quantity to determine. The coercive field becomes wider in the low temperature region. In the low temperature region the coercive field is used to know the minimum required field to saturate the magnetisation in transport measurements.

The magnetic properties of YIG are agreed with the results gained from the crystal structure analysis. The results showed that M_s and H_c of YIG/GGG, which was grown with 6% of Oxygen contents, were agreed with M_s and H_c values of bulk YIG. However, the film of YIG/GGG, which was grown with 5%, 5.5% and 6.5% of Oxygen contents showed that M_s and H_c were close to M_s and H_c values of bulk YIG.

4.4 YAG substrates

In this study, both substrates GGG and YAG have been used, in the (111) orientation. YAG substrate is used as an alternative choice substrate because the dead layer is unfavourable for applications in the propagation of magnons when we used GGG substrate. The dead layer is due to gadolinium diffusing from the GGG substrate into the YIG film at high temperature during annealing process [173]. In this study, a non-magnetic dead layer has been found to form due to the diffusion from aluminium or yttrium when a YAG substrate is used to the YIG film. YAG has a larger difference in the lattice constant from the lattice constant of YIG. The different lattice constant is large and has induced a strain on the YIG due to the mismatching, but YAG substrate has a benefit over GGG substrate in that the YAG has no strong paramagnetic signal.

YIG films on YAG were annealed at 850 °C in open air. After annealing the XRD measurements used to determine the lattice constant and the crystalline orientation of YIG. Figure 4.21(a) shows the high angle scan from x-ray diffraction for different thicknesses of YIG which has been annealed on a YAG substrate. For YIG films grown on GGG, the YIG peak has high intensity compared with the intensity when we used GGG substrate. The low intensity for the YIG films on YAG could be due to the quality of the film. The peak positions in the x-ray diffraction are much closer to the bulk value and have high intensity for the YIG peak 10^3 for YIG films grown on GGG see figure 4.5(a) but for YIG films grown on YAG the YIG peak has low intensity 10^1 figure 4.21(a). This can be explained by the large lattice mismatch between the lattice constant for YIG and YAG lattice constant. Figure 4.21(b) shows the lattice constant for different thicknesses of the YIG samples on YAG and it is much smaller compared to the bulk YIG lattice constant (red point). This could be due to the large different between YIG lattice constant and YAG lattice constant or due to the dead layer at the interface between the YIG and YAG as we see the YIG lattice constant can be changed if the thickness of dead layer changed in figure 4.8.

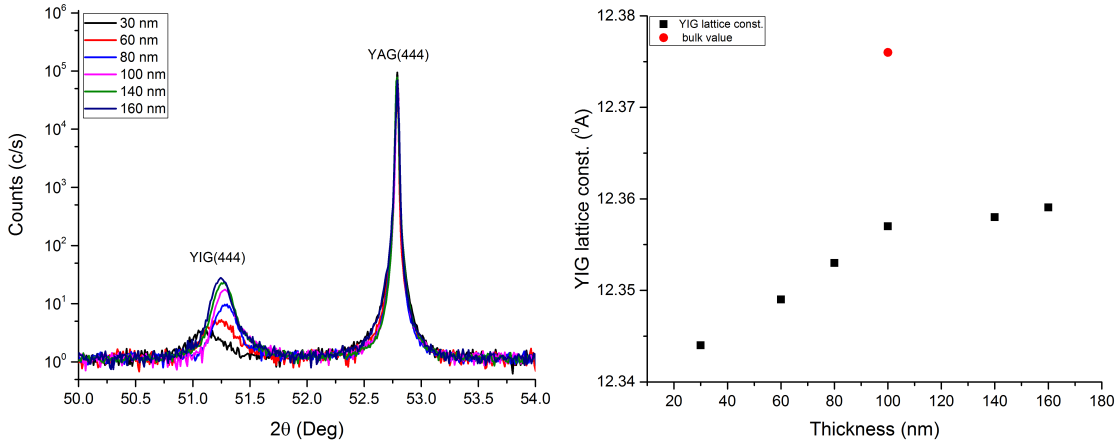

(a) (b)

Figure 4.21: X-ray diffraction scan for YIG films on YAG substrate after annealing. The YIG has a(111)crystalline orientation. Intensity of the YIG peak varies as a function of thickness(a). The lattice constant (a_o) as a function of thickness of the YIG samples on YAG compared to the bulk YIG lattice constant 12.376 Å(b).

We used the XRD to determined the crystalline orientation and the lattice parameter of 40 nm YIG on YAG were grown with different contents of oxygen during sputtering(5 %, 5.5 %, 6 % and 6.5 %). Figure 4.22 shows the high angle scan from x-ray diffraction and the lattice constant for annealed 40 nm of YIG on YAG with different oxygen contents. The lattice constant can be change by changing the oxygen contents of the YIG samples as we see in figure 4.22(b).

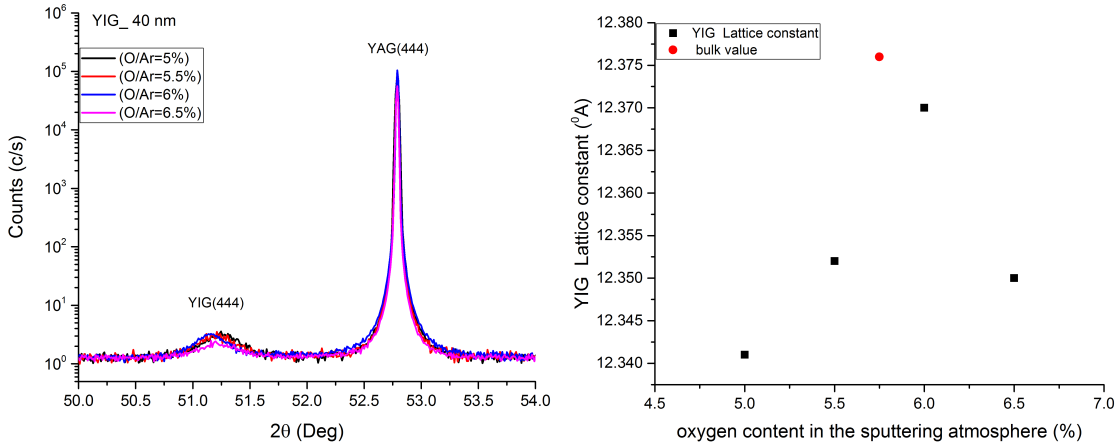

(a) (b)

Figure 4.22: X-ray diffraction scan for annealed 40 nm YIG films with different oxygen contents on YAG substrate. The YIG has a(111)crystalline orientation. Intensity of the YIG peak varies as a function of oxygen contents (a). The lattice constant (a_o) as a function of oxygen contents for YIG on YAG compared to the bulk YIG lattice constant 12.376 Å(b).

YIG films with different thickness ranging from 30 nm to 160 nm were growing on YAG substrate. Figure 4.23(a) shows the hysteresis loops for different thickness of YIG on YAG at room temperature. Figure 4.23(b) shows that the linear extrapolation of the saturation magnetic moment versus thickness shows the thickness of the diffusion between the YIG and YAG substrate, which is about 5.75 nm. The magnetization can be found from the measured magnetic moment by determining the thickness of each sample and using the sample volume. The saturation magnetisation obtained from the slope is M_s =63 $\pm$6 emu/cc, compared to the bulk value M_s = 143 emu/cc at room temperature.

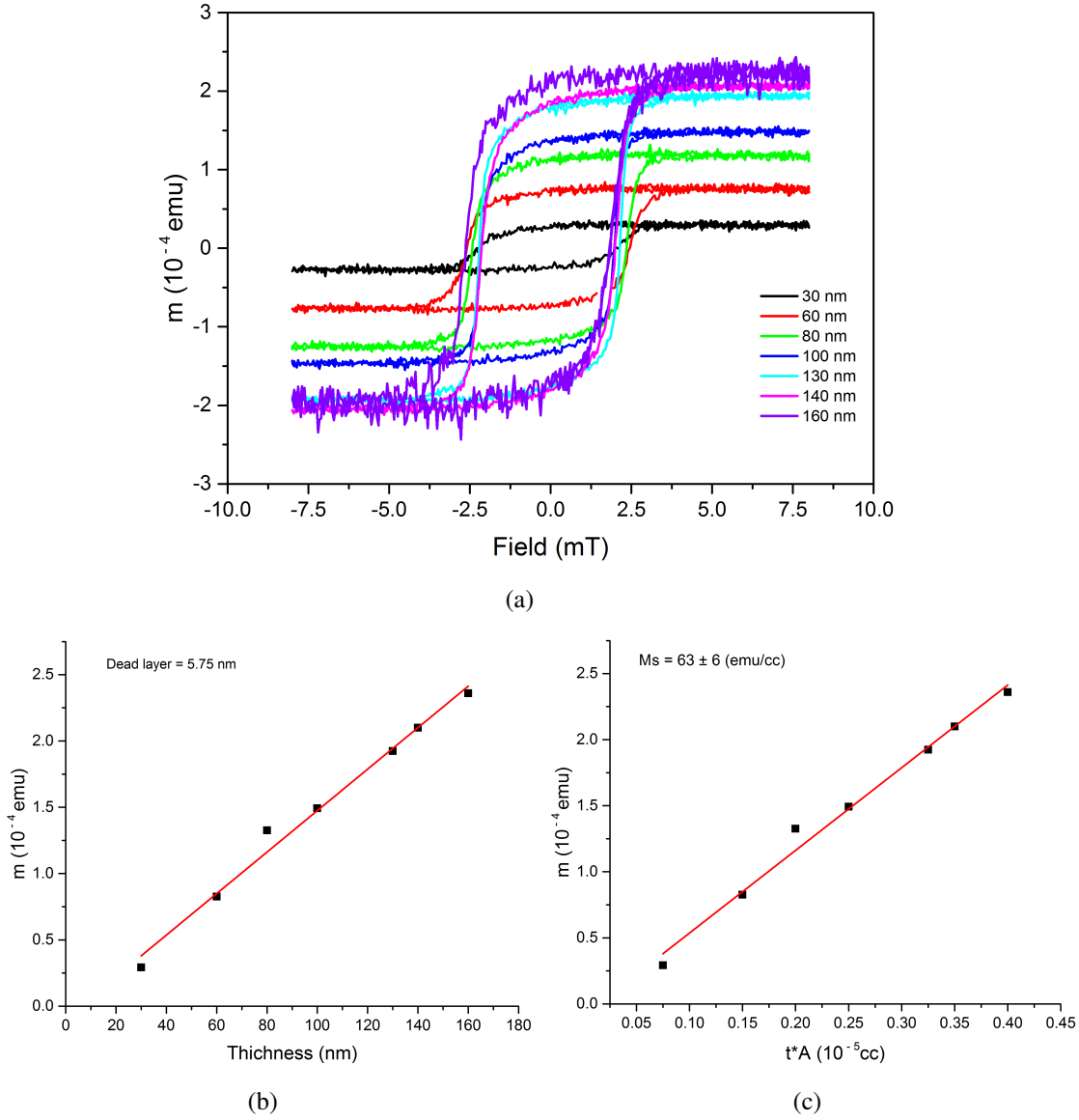

Figure 4.23: Magnetic moment as a function of applied field at room temperature for different thicknesses of YIG on YAG (a). The linear extrapolation of the saturation magnetic moment as a function of thickness shows that there is a dead layer of about 5.75 nm (b). (c) The linear extrapolation of the saturation magnetic moment as a function of thickness times area shows the $M_s = 63 \pm 6$ emu/cc.

Several samples of 40nm YIG films were grown on YAG substrates with different contents of oxygen. These samples on YAG were made alongside twin samples on GGG subtrate. SQUID-VSM magnetometry was used to measure the magnetic moment of the YIG samples on YAG in the wide temperature range from 2 K to 300 K. Figure 4.24 shows the hysteresis loops for 40 nm thick of YIG on YAG substrate at different temperatures. To ensure that the sample was saturated we applied magnetic field (H) from -250 Oe to 250 Oe.

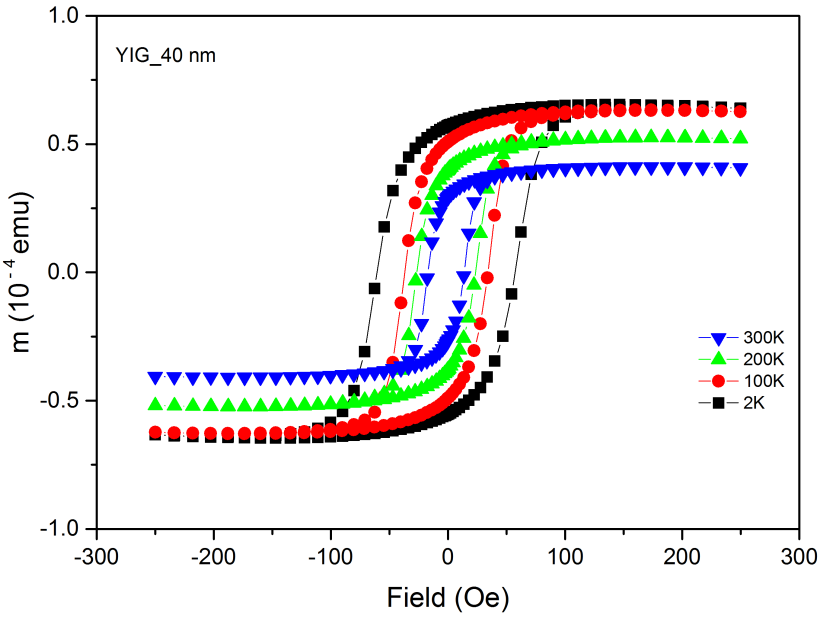

Figure 4.24: : Hysteresis loops as a function of applied field for 40 nm YIG on YAG at different temperatures.

The saturation magnetisation as a function of temperature M(T) for 40 nm YIG on YAG with different oxygen contents during sputtering is plotted in figure 4.25. Figure 4.26 shows the coercive field for 40 nm YIG on YAG as function of temperatures. the coercivity can be changed by changing the growth oxygen contents.

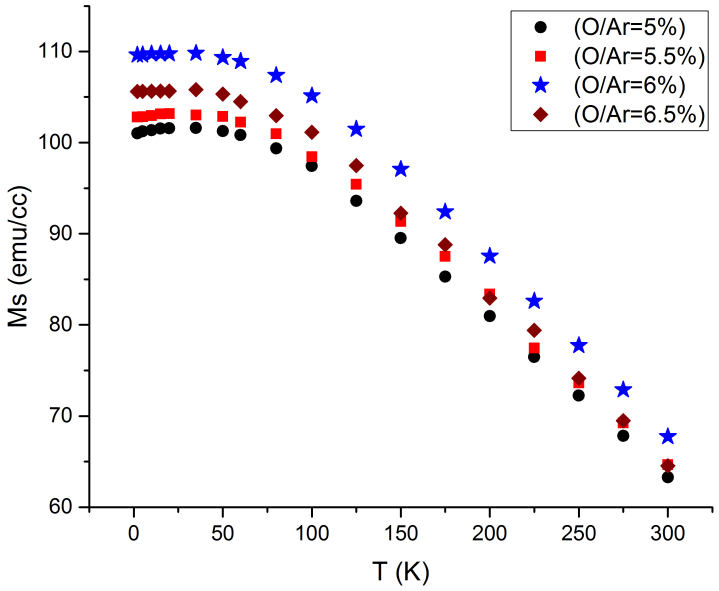

Figure 4.25: : The temperature dependence of the saturation magnetisation for 40 nm YIG on YAG with different oxygen contents.

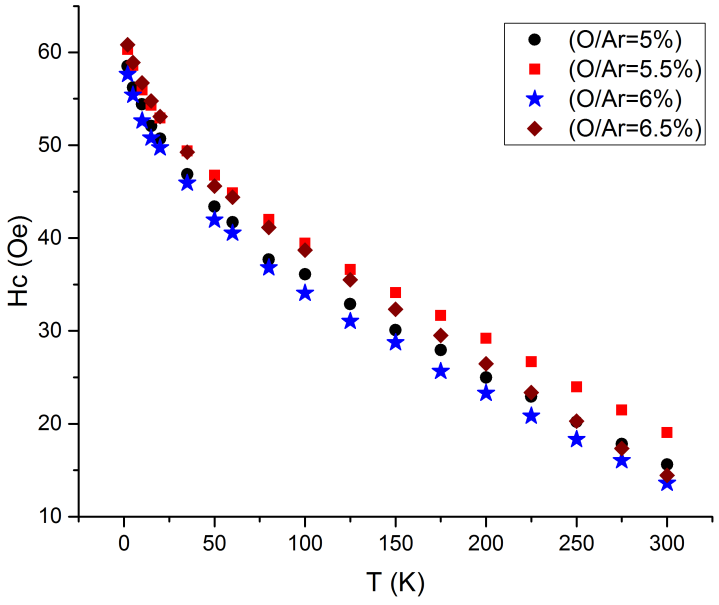

Figure 4.26: : Coercive field of 40 nm YIG on YAG as a function of oxygen growth content at different temperatures. The temperature dependence of the coercive field H_c.

Figure 4.27 shows two annealed 40 nm YIG samples were grown on two deferent substrates GGG and YAG. The two YIG samples on YAG and on GGG were grown at the same time and annealed together in a furnace. The saturation magnetisation is found to be much bigger for the sample on GGG substrate than YAG substrate. M_s at room temperature for YIG on GGG is found 140 ± 6 emu/cc, which is comparable to the M_s bulk value . YIG on YAG substrate, the M_s is found 63 ± 6 emu/cc; less than half the M_s for YIG on GGG.

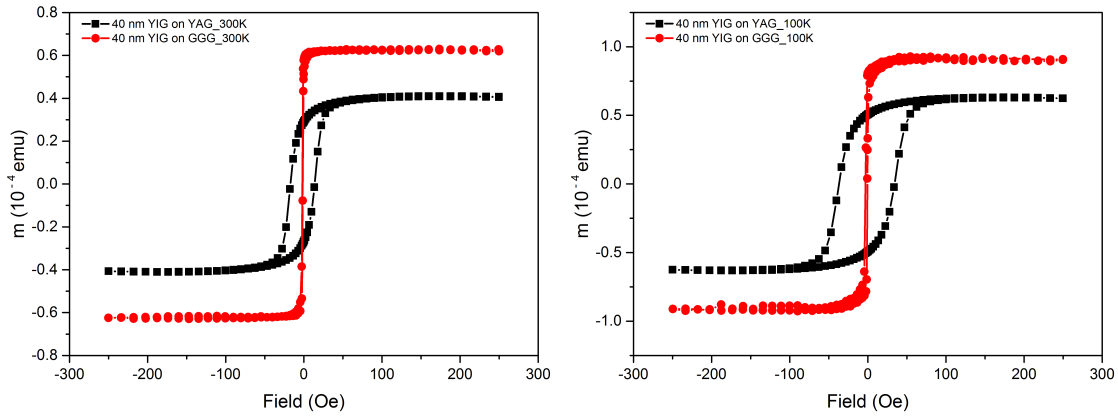

(a) (b)

Figure 4.27: Magnetometry data for 40.8 nm of YIG grown by RF magnetron sputtering on both GGG (red) and YAG (black) substrates. The samples were annealed at 850 °C. VSM measurements are taken in the plane of the sample at a temperature of 300 K (a) and 100 K (b).

4.5 Conclusion

In this chapter, we performed a comprehensive study for the YIG films sputtered by RF, this study includes of the crystallinity and morphology and also the chemical nature of the YIG/GGG interface and the magnetic properties after annealing. We have used a variation in Oxygen pressure during sputtering to improve the structural and magnetic properties of YIG films. The x-ray reflectivity and x-ray diffraction used to study the structural quality of the samples. From the Bede fit for the XRR results for the annealed YIG sample, we noticed an interdiffusion at the YIG/GGG interface, the thickness of the interdiffusion can be changed if we changed the Oxygen contents during sputtering. The XRD results for the annealed YIG sample showed that we have improved the structural quality of the samples, for example like the films with 6.2% of Oxygen has lattice constant similar to the Bulk value. Our AFM results for YIG films confirmed that our films are smooth with roughness about 1-3 Å.

The most important results that the Gd-interdiffusion region at the YIG/GGG interface, which at room temperature is paramagnetic and at low temperatures orders antiparallel to YIG at low temperatures. Our results from VSM and SQUID shows that we have reduce the dead layer from ~ 6 nm for the samples with 5% of Oxygen to be ~ 2.35 nm for the samples with 6.2% of Oxygen.

YAG substrate was used as an alternative choice substrate because we want to stop the diffusing from the substrate into the YIG film if the dead layer is from gadolinium diffusing from the GGG substrate into the YIG film. In this study, a nonmagnetic dead layer about 5.75 nm has been found, the diffusion from aluminium or yttrium when a YAG substrate is used to the YIG film. The peak positions in the x-ray diffraction are much closer to the bulk value and have high intensity for the YIG peak 10^3 for YIG films grown on GGG but for YIG films grown on YAG the YIG peak has low intensity 10^1. This can be explained by the large lattice mismatch between the lattice constant for YIG and YAG lattice constant. The lattice constant can be change by changing the oxygen contents of the YIG samples. The saturation magnetisation is found to be much bigger for the sample grown on GGG substrate than YAG substrate. M_s at room temperature for YIG on GGG is found 140 ± 6 emu/cc, which is comparable to the M_s

bulk value . YIG on YAG substrate, the M_s is found 63 ± 6 emu/cc; less than half the M_s for YIG on GGG.

CHAPTER 5

Spin Hall magnetoresistance in platinum

5.1 Introduction

Spintronics has attracted intense interest because it is combined the fields of electronics, magnetics, and computer engineering [98; 175; 176]. It has been considered as the technology's key of the next generation for the information processing devices, the information is transferred and processed by the electrical spins rather than the electrical charges [175].

Insulating spintronics [177] has appeared as a hopeful, novel technological aims based on the combination of ferromagnetic insulators (FMIs) as a media to generate and process and transport spin information for long distances in devices [8; 9; 45; 47; 49; 88; 104; 105; 177–198]. The usefulness of using FMIs compare to the metallic ones is that the charge currents' flow is avoided, so stopping ohmic losses or the emergence of unwished spurious effects. Some phenomena discovered in insulating spintronics as the spin pumping [45; 47; 178; 179], the spin Hall magnetoresistance (SHMR) [104; 105; 179–187], the magnetic gating of pure spin currents [191; 192] or the magnon spin transport (MST) [8; 9; 47; 88; 193–198], the spin Peltier effect [190], the spin Seebeck effect [49; 179; 188; 189].

The fundamental block structure that used to explore these phenomena is created by a FMI layer –typically YIG due to the soft ferrimagnetism, its small damping, and insignificant magnetic anisotropy– and a non-magnetic (NM) metal with strong spin-orbit coupling (SOC) as Pt or Ta placed on it, which is basically used to generate or detect spin currents by the spin Hall effect (SHE) or inverse spin Hall effect (ISHE) [44; 111; 116; 199; 200]. Pt doped with magnetic impurities has been an order of interest in solid state physics, with the magnetic proximity effect (MPE) discovered for the potential to design materials that have desirable properties for applications [201–207]. Recently, great interest is focused on the MPE effect on spin transport phenomena such as the spin Hall magnetoresistance and spin Hall effect [160; 161; 208–215].

For the development of available spin-based devices, It is important to improve the spin transport efficiency and the spin diffusion length because during transport the spin is not conserved [216]. The interfacial condition for spin transport efficiency is one of

the dominant factors because the information and most energy transferred via transport spins in typical spin-based devices is lost at the interface [217–220].So, improving the efficiency and understanding the mechanism of spin transport at the interface is a very important issue for the investigation of spin-based devices. It has been reported that the spin transport is sensitive to the interface characteristics [170; 219–232]. Also, it has been reported that the chemical modifications and crystallinity are effective features, it can improve or quell spin transport efficiency for a high quality interface or amorphous interface [219–222].

The spin-mixing conductance is the most relevant parameter that determines the spin current transport across the interface [52; 179; 233]. However, other interface effects is still under debate whether, it could be related to these hybrid systems. Such as the spin-dependent interfacial scattering [234], the MPE [161; 210; 215; 235–237], the Rashba-Edelstein effect [238–241], the anomalous Nernst effect [210; 242; 243]. Therefore, it is very important to understand the interface's role of the NM/FMI and the impact of its properties on the resulting spintronic phenomena.

5.2 Resistivity

5.2.1 Growth parameters

DC sputtering was used to grow platinum (Pt) on YIG. Calibration sheet films of Pt were grown on silicon (Si) to study the thickness and work out the deposition rate. XRR was used to determine the sheet films thickness and growth rate. The angular positions of the Kiessig fringes (inset of figure 5.1(a)) was used to determine he thickness by using equation 3.4. Figure 5.1(a) shows the x-ray reflectivity (XRR) of 30 nm Pt. Figure 5.1(b) shows that the Bede software was used to fit the XRR curve.

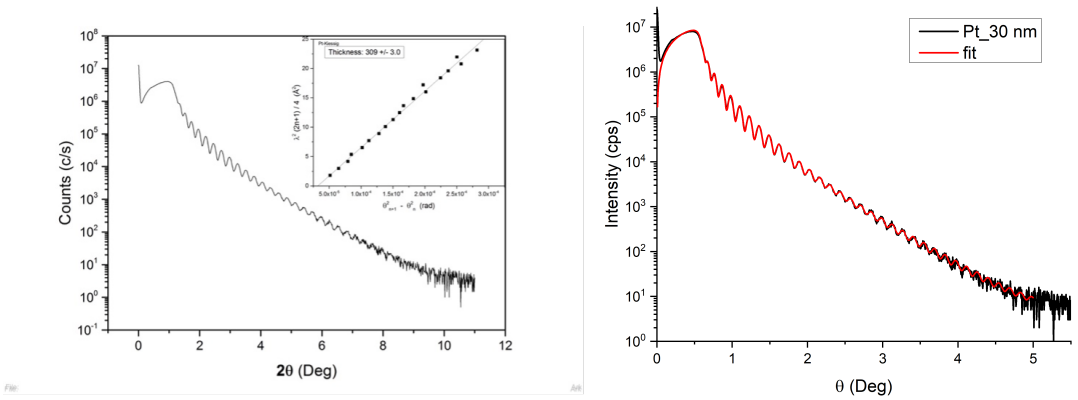

(a) (b)

Figure 5.1: X-ray reflectivity Pt on Si (a)and good fit by using Bede software in (b).

The masking technique that shown in figure 3.2 was used to grow platinum wires on the YIG films. The thickness of Pt wires was fixed to be 2 nm to study the possible effect from the oxygen content in the YIG surface. The Bede software was used to fit the X-ray reflectivity (XRR) curve for Pt on YIG as shown in figure 5.2.

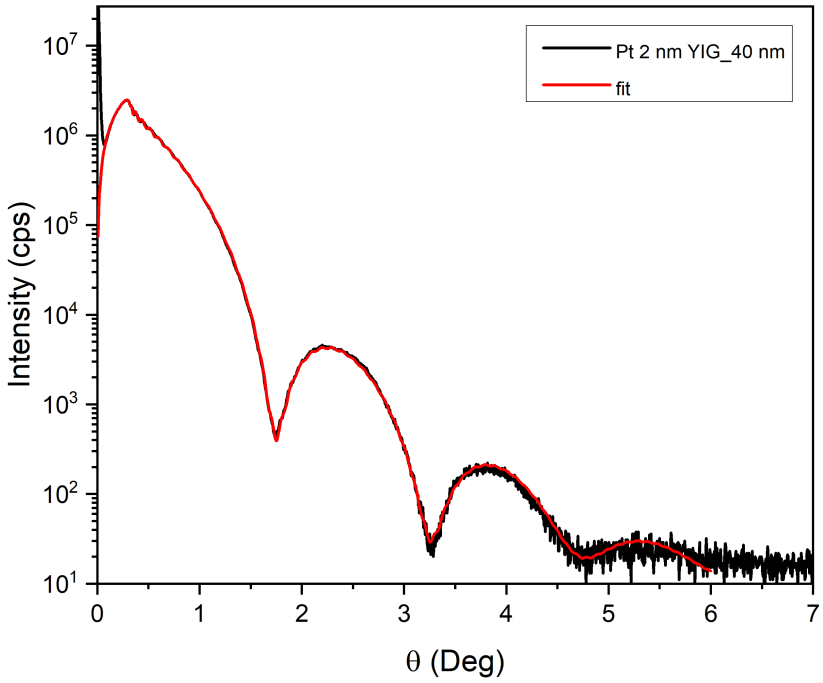

Figure 5.2: Good fit by using Bede software for the XRR 2 nm of Pt on 40 nm annealed YIG (the YIG film has 6% of Oxygen).

The Bede software was used to fit the reflectivity curves for Pt on Si as shown in figure 5.1(b), and Pt on YIG film as shown in figure 5.2. We used the software Bede to get further information about the chemical nature of the Pt/YIG interface and also the density and roughness. The parameters we got from the fitting for each curves is shown in the table 5.1. To have the best fit for the x-ray curves, there is a layer between Si and Pt which is SiO_2 and a layer on top of Pt which is PtO (figure 5.1(b)). We have to include Gd layer between the GGG substate and YIG, this is due to diffusion between GGG/YIG during annealing. From the fits the thickness of Gd layer is 7.50 Å which agreed with results from the fits in chapter 4. Also, we have to add a top layer on Pt which is PtO (figure 5.2).

	MATERIAL	THICKNESS(Å)	DENSITY (%)	Roughness(Å)	Goodness of fit
	Si	∞	96	1.42	0.04
	SiO_2	3.41	105	7.11	
Figure	Pt	302	97	5	
5.1(b)	PtO	2.50	102	2.70	
	GGG	∞	102	2.53	0.05
	Gd	7.50	107	9.45	
Figure	YIG	400	97	2.75	
5.2	Pt	20	95	3.63	
	PtO	2.11	100	1.40	

Table 5.1: Parameters used in Bede software to fit the x-ray reflectivity data for Pt on Si shown in figure 5.1(b), and sheet films of Pt on YIG film shown in figure 5.2.

AFM was used to determine the Pt wires thicknesses and surface roughness. Many scan were taken around the Pt edge to study the thickness carefully when the Pt was grown by the mask. Figure 5.3 shows the AFM scan of Pt wire on YIG and the scan cross the Pt wire. We have done many scan on each wire and took the average of the wire thicknesses and an average surface roughness. The cross sections in figure 5.3(b) , 5.3(c) shows how thick the Pt wire, the cross sections were done on too many different area and we took the average as we see in table 5.2. Table 5.2 shows the average of thicknesses and the average surface roughness of different areas of Pt wire.

Oxygen content (in YIG)	Pt wire Thickness(Å)	Pt Roughness(Å)
5%	19.6	4.5
5.5%	22	5
6%	20.5	4
6.6%	20.2	4

Table 5.2: the average of thicknesses taken from the AFM scan section cross the Pt wiers, and the average roughness of different areas of Pt wire.

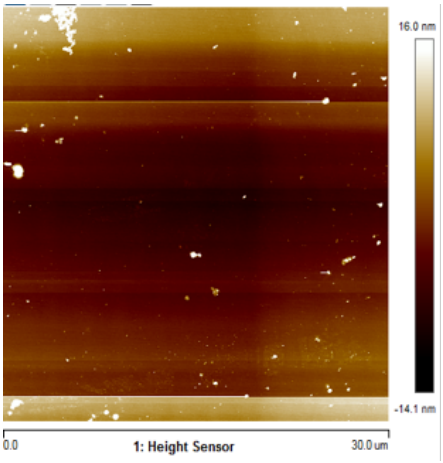

(a)

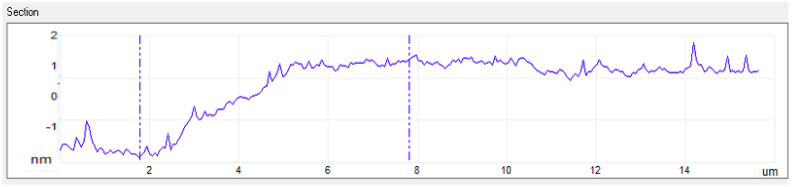

(b)

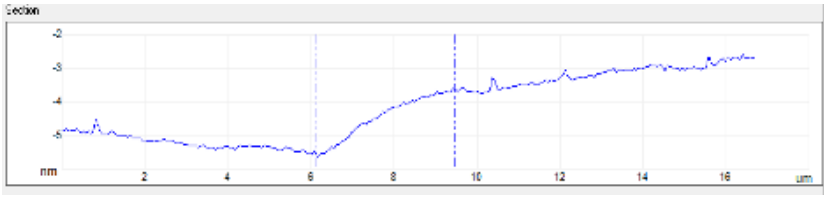

(c)

Figure 5.3: AFM scan of platinum on YIG from AFM and scan section cross.

5.2.2 Temperature dependence

There are many factors that can affect the resistivity as the surface roughness and the impurity in the platinum structure [244–246]. To reduce this, the samples used for the SHMR study in this chapter were done on YIG films prepared with a different oxygen content in the sputtering atmosphere to change the vacancies. Fuchs-Sondheimer model described that the surface scattering is the dominant effect. This raised the resistivity at 300K above the bulk value of 10.6 $\mu\ \Omega$ cm [247–249]. The Pt grown on YIG shows an upturn in the resistivity at low temperatures. This upturn in metals that have magnetic impurities is known as the Kondo effect [250; 251]. The data in figure 5.4 shows the resistivity upturn in platinum grown on YIG at low temperatures. The effect of upturn on the resistivity is only at low temperatures. The localisation effect is the more convincing argument for the resistivity upturn in the low temperature region [159]. In ultra thin films the localisation effect has been seen and it is due to the reduced dimensions and electron-electron scattering in a two dimensional system [252; 253].

Weak localisation is an effect prevalent in disordered conducting systems at low temperatures. In these situations, a positive correction to the conductor's resistivity manifests, impacting magnetotransport in the system. Not only does resistivity increase at low temperatures, but the magnetoresistance of a sample is also impacted [254; 255] .

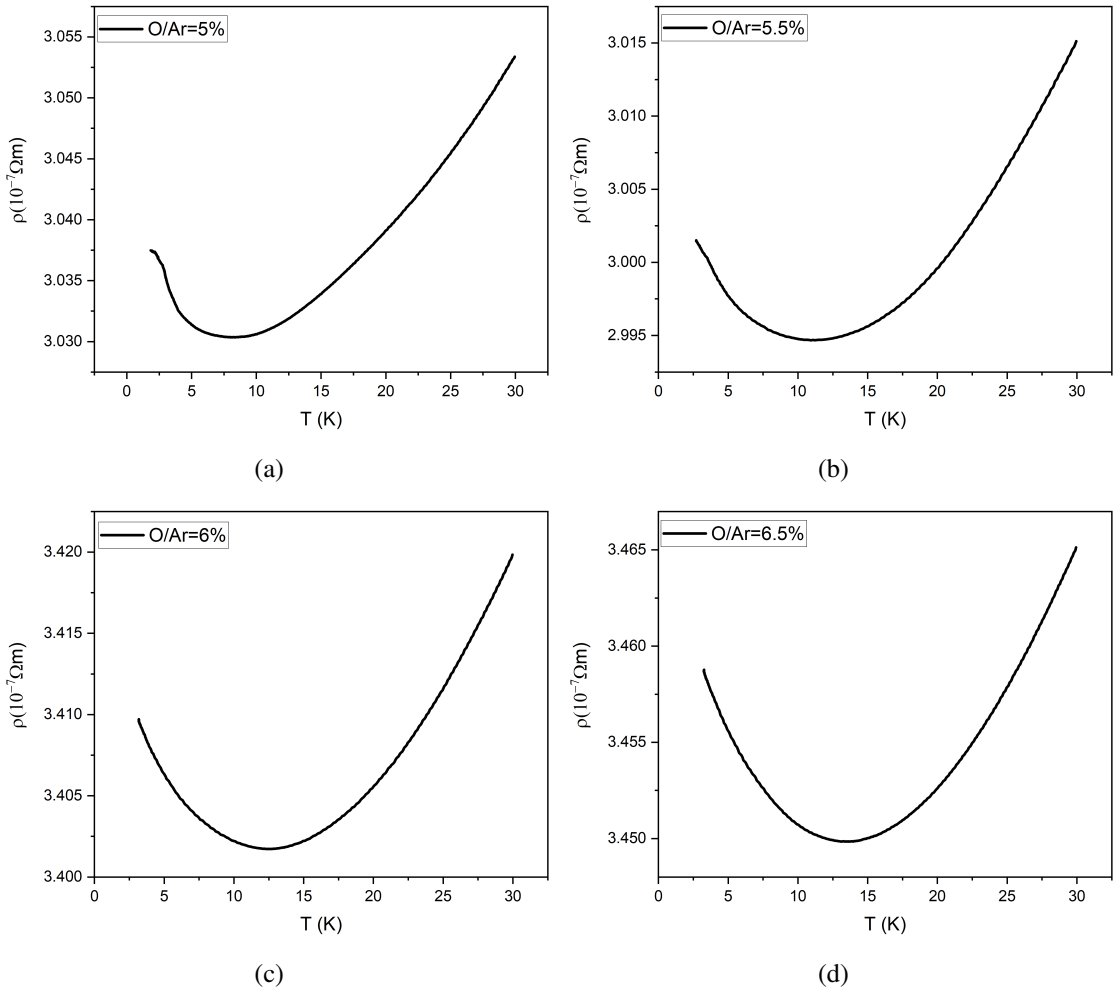

Figure 5.4: Resistivity at low temperatures of 2 nm Pt on 40 nm YIG. The YIG has different oxygen contents 5 % (a), 5.5 % in (b), 6 % in (c) and 6.5 %(d).

The resistivity of 2 nm platinum grown on YIG can be changed if the YIG has different oxygen contents. The big of the upturn for all samples is the same $(0.0075 \times 10^{-7})\ \Omega m$. At 2 K the minimum value of the resistivity is $3.001 \times 10^{-7}\ \Omega m$ (5.4(b) and the maximum resistivity value is $3.458 \times 10^{-7}\ \Omega m$, the difference is only 15%.This is not understand but it could be due to the different oxygen contents in the YIG that may affect on the YIG/Pt inteface or it could be due to the additional layer on Pt. Figure 5.5 shows the resistivity data over the 2-290 K temperature range. This is related to the SHMR as it is an important fitting parameter. As we see from figure 5.5(b) the

resistivity has a small increase with the oxygen contents. Due to resistivity change we expect a change in spin Hall angle as the resistivity contributes to the spin Hall angle in the SHMR equation.

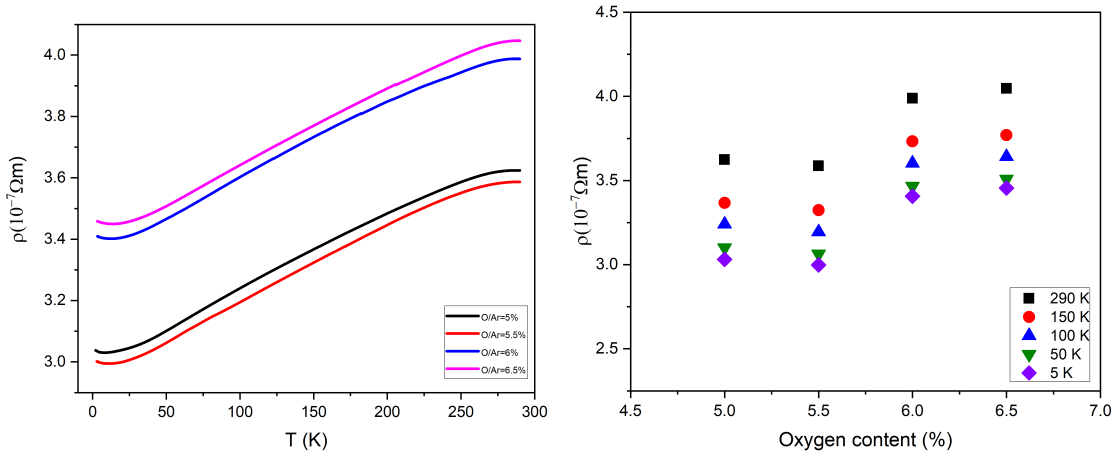

(a) (b)

Figure 5.5: Resistivity as a function of temperature for 2 nm Pt on 40 nm YIG showing the comparison between the different oxygen contents in YIG films.

5.3 SHMR properties

5.3.1 Angular rotations

The angular dependence was found by measuring resistances. Resistance measurements are taken at a stable temperature and a current of 1mA . To remove any noise because of the sample movement causing temperature shift during rotation, the measurements were taken in 5°steps with a 2 second pause between the sample moving and the next measurement. The measurements were done in from -180°to 180°in both clockwise and anticlockwise direction.

At room temperature the data and fit match everywhere in figure 5.6(b) but at 5 K in figure 5.6(c) the data and fit does not match, the resistance goes up at 0 ° and it is less at 90 °. In our experiments we start perpendicular then go to transverse so in that case the additional MR is not AMR because the magnetisation always perpendicular to the spin current. At 5 K we see two things, the SHMR and the additional MR which mean the Pt is beginning to look like it is magnetic and the additional MR is associated with this proximity magnetism in the Pt.

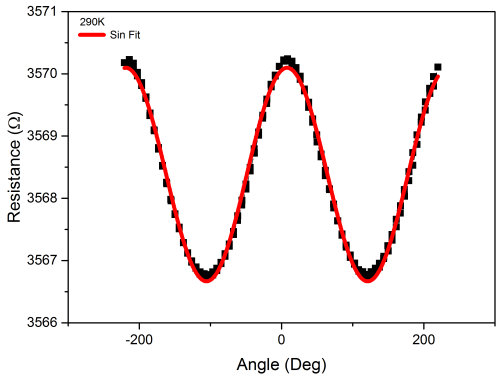

(a)

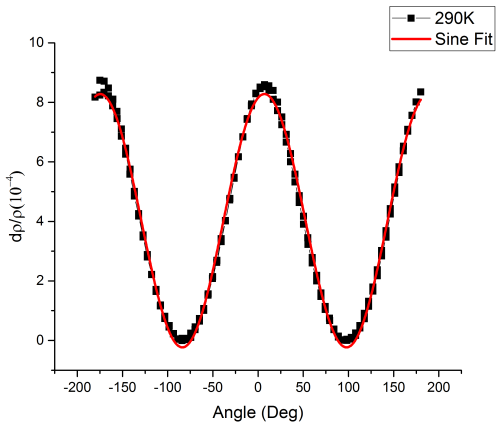

(b)

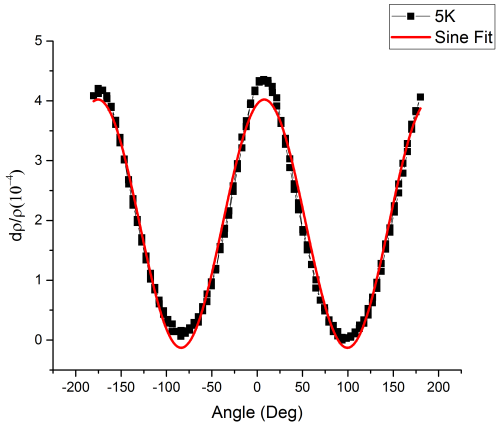

(c)

Figure 5.6: Resistance change of 2 nm platinum wire as a function of angle at 290 K (a) and the SHMR change as a function of angle at (290 K in (b), 5K in (c)).

5.3.2 Temperature dependence

The SHMR theory just require the magnetisation direction of the YIG is saturated in the required direction, it does not require any directly applied field in the wire of platinum. It is important to measure the effect on different properties of YIG films as the spin current injected into the YIG by the SHMR. We measured 2 nm platinum on 40 nm YIG, the YIG has different oxygen content during sputtering. Each sample has four wires of platinum to ensure consistency and keep our samples uniform. Also, to make sure we grew all samples in one vacuum cycle and get more samples to do more measurements. Figure 5.7 the different temperatures dependence of the SHMR between 5-290 K. As we see there is a small variation between the different oxygen content in YIG. At below 50 K the different oxygen content in YIG has no clear effect the SHMR value. The small variations between each sample could be due to the small difference in the YIG surface quality as we see from the previous chapter the different oxygen content can change the YIG surface roughness. From the SHMR theory the variation can be due to the spin mixing conductance or the spin Hall angle.

Figure 5.7(a) is shown the fits from taking the extremes by modifying equation 2.36. To produce a different fit we can change the spin mixing conductance and the spin Hall angle as the spin Hall angle is increased the spin mixing conductance reduces.

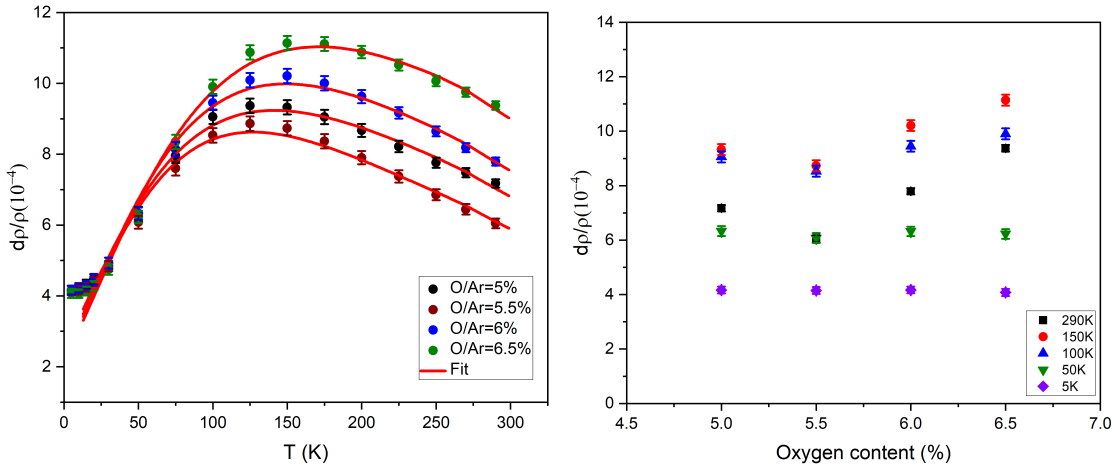

(a) (b)

Figure 5.7: SHMR in 2 nm platinum on 40 nm YIG (YIG has different oxygen content)(a). Values selected at several different temperatures in (b) show no difference below 50 K for all samples.

The SHMR data fit is done by assuming a spin mixing conductance is constant of $1.5 \times 10^{15} \Omega^{-1}\ \mathrm{m}^{-2}$ [179; 256] and the spin diffusion length is modelled by equation 5.1

$$\lambda = \frac{a}{T + b} \tag{5.1}$$

whereby a and b are constants. Figure 5.8 shows the spin diffusion length at different temperature as a function of oxygen content. This shows that the T dependence of spin diffusion length is the same, this is expected because the shape of SHMR is the same for all 4 samples and since we assume that temperature dependence of spin diffusion length is due to E-Y scattering (phonons) we expect it to be the same. At high temperatures as we see at room temperature in figure 5.9, the spin diffusion length is small in comparison to the values (λ = 1.5 nm) in [257; 258] and similar to the values (λ = 0.7 nm) in[186].

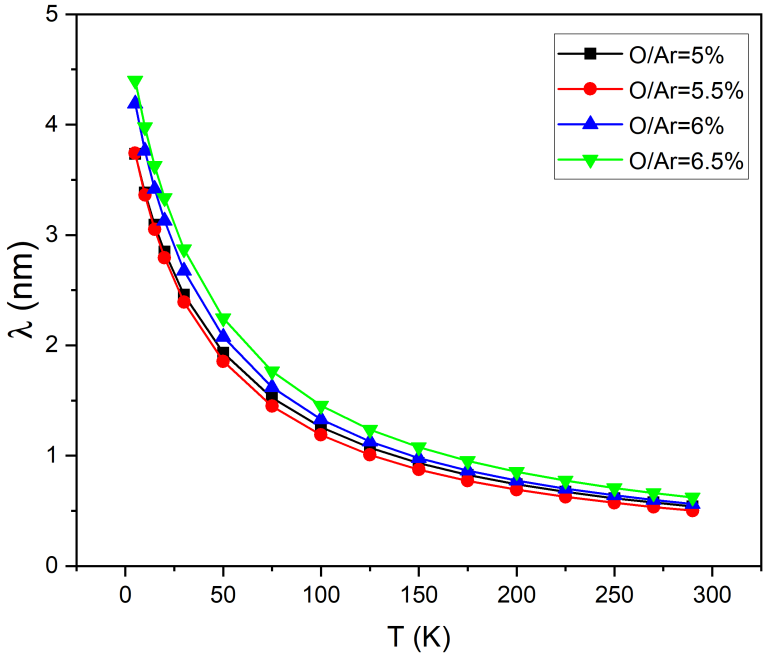

Figure 5.8: Spin diffusion length at different temperature as a function of oxygen content in YIG

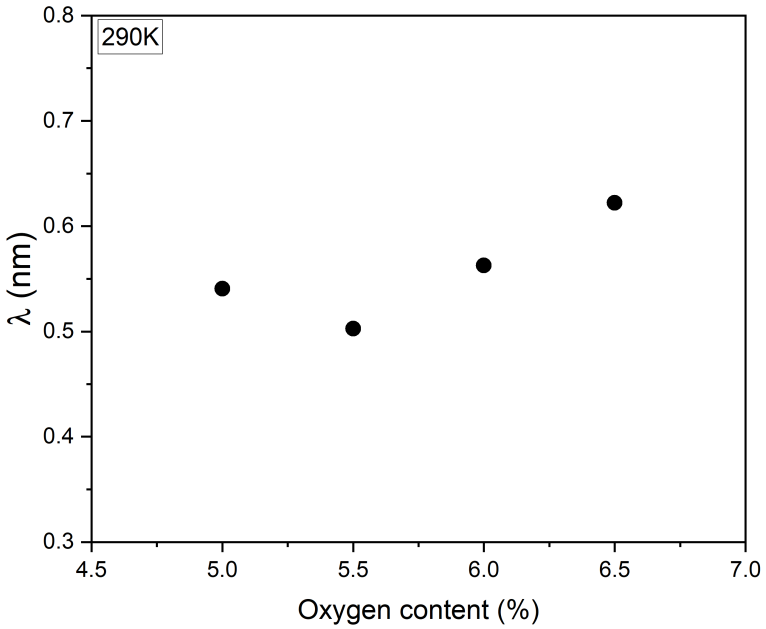

Figure 5.9: Spin diffusion length at room temperature as a function of different oxygen content in YIG.

The spin Hall angle we obtained is shown in figure 5.10(a) as function of oxygen content. We did the fit in two different ways, the first way was we kept the spin mixing conductance constant as we see in figure 5.10(a) , the other way was we kept the spin Hall angle a constant and varied the spin mixing conductance in figure 5.10(b). In figure 5.10(b) The values are typical and from the shape of this curve compared to the spin hall angle, we cannot unravel one from the other. However, since G is nearly the same and a typical value, we will say that it is the spin hall angle that accounts for the difference in SHMR.

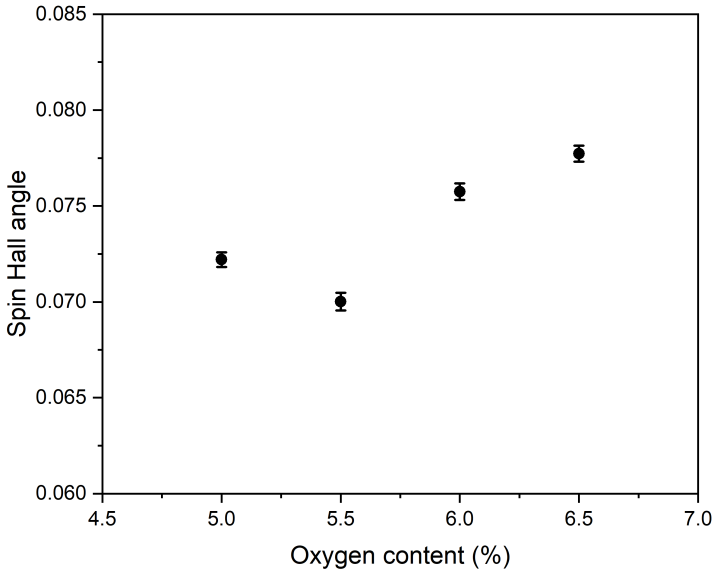

(a)

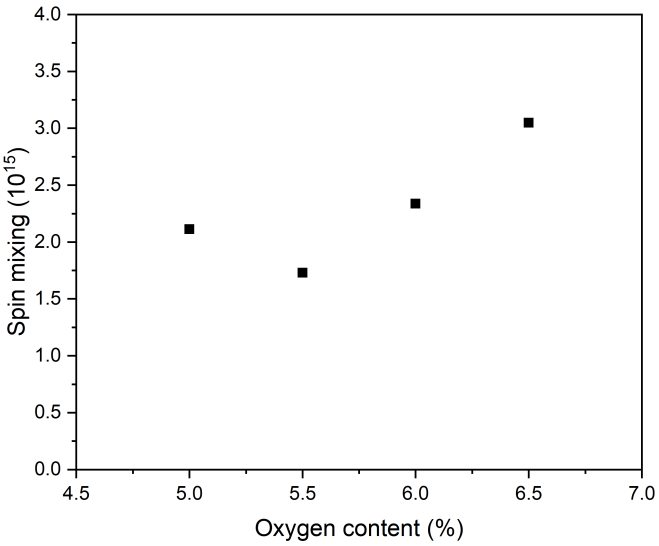

(b)

Figure 5.10: Spin Hall angle at room temperature as a function of different oxygen content in YIG (a). Spin mixing as a function of different oxygen content(b).

Figure 5.11 shows the spin Hall angle and spin diffusion length as function of SHMR at 150 K because if we look at figure 5.7(a) the interesting thing is that below 100 K every thing goes to be the same and above 100 K they separated, we want to know what the parameter makes the separation. It could be the spin Hall angle or spin diffusion length and we want to know one of them is more important than the other one.

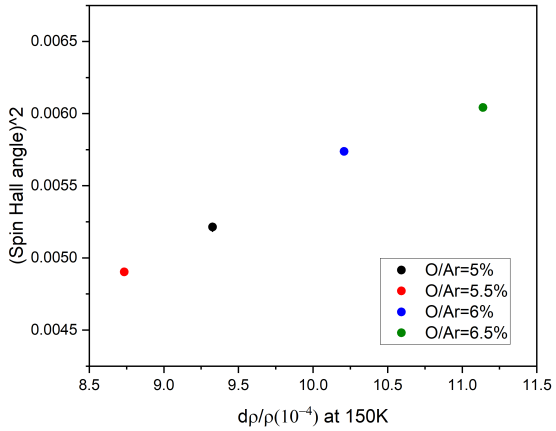

(a)

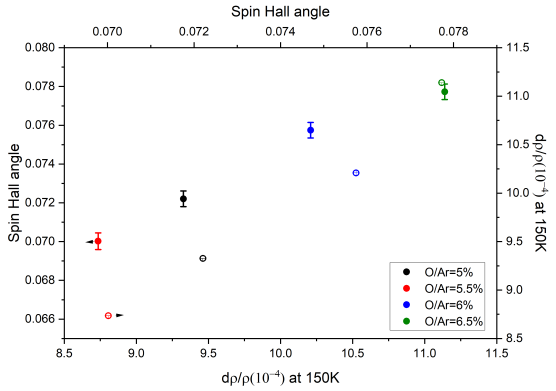

(b)

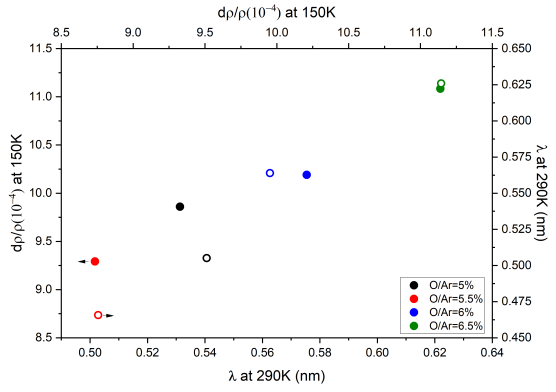

(c)

Figure 5.11: (a) (Spin Hall angle)^2 as a function of SHMR at 150 K. Spin Hall angle as a function of SHMR at 150 K (b). Spin diffusion length at room temperature as a function of SHMR at 150 K (c).

5.4 Field-dependent magnetoresistance

There are three orientations we used to measure the MR. First, the perpendicular orientation, where the applied field is perpendicular to the plane of the sample, in this orientation the field is out of the plane of the sample 5.12. Second, the transverse orientation, where the field is perpendicular to the charge current but oriented in the plane of the sample 5.14. Third, the longitudinal orientation, where the applied field is parallel to charge current 5.16.

The MR in figure 5.12 is composed of two parts, one from the YIG which saturates at a few hundred mT and the high field part which is negative at low temperatures and changing sign as temperature is increased.

For the high field data, 2nm of Pt on YIG is positive at all temperatures but if doped with small amounts of Fe at the interface with YIG, it is negative at low temperatures changing to positive at about 50K [159], it looks very similar to these results.

Now we look at low field as we see from figures (b,d,f,and h) which shows us there is some evdence. Our data shows out of plane anisotropy (very difficult to measure this by magnetometry) very strong in 5% data but present in all samples at low temperatures becomes strongly asymmetric at low temperatures.

In figure 5.12, when B $>$ 1 T thin Pt on its own has a positive MR at all temperatures [159] and in the presence of either YIG or magnetic impurities [159] has the behaviour seen here: negative MR at low temperatures changing to positive above 100 K.

B $<$ 1 T the MR now reveals that a perpendicular anisotropy is present in the YIG that is temperature dependent. This effect is rarely seen in M(H,T) data due to the difficulty of seeing a small signal above the background of the paramagnetic GGG. Both of these are indications of magnetic proximity in the Pt.

Though there is a contribution from the SHMR, the AMR and the coercive behaviour of the MR indicate that the Pt is magnetic.

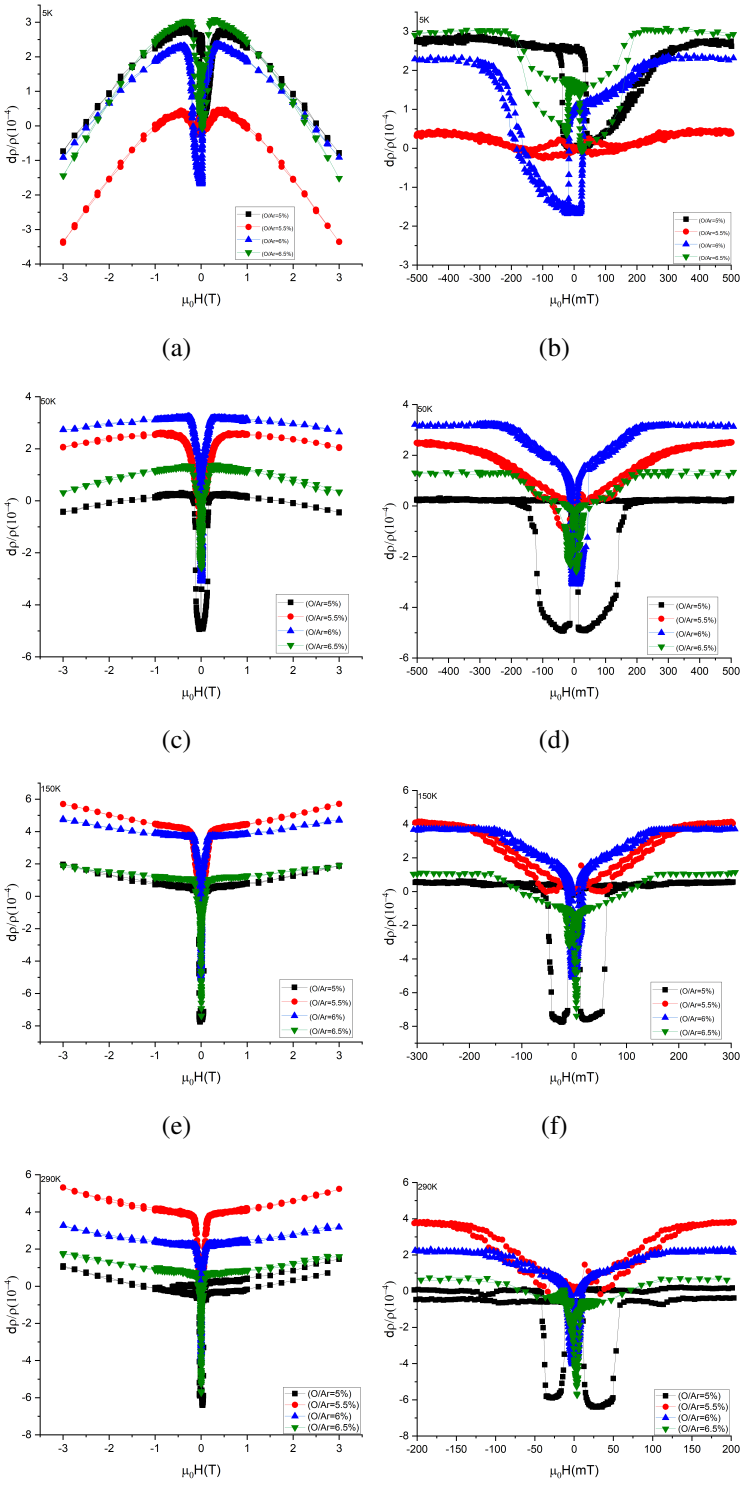

Figure 5.12: The perpendicular magnetoresistance for 2 nm Pt on 40 nm YIG plotted as a function of applied magnetic field at different temperature.

The coercive field (H_c) for all orientations were measuring by measuring the difference field between the two peaks at low fields and it is shown in figure 5.13(a) for the perpendicular orientation , figure 5.15(a) for the transverse orientation, and for the longitudinal orientation in figure 5.17(a). The saturation field (H_s) was measured for all orientations from the saturation at low fields. Figure 5.13(b) is shown the saturation field for the perpendicular orientation, the saturation field for the longitudinal orientation is shown in figure 5.17(b), and figure 5.15(b) for the for the transverse orientation.

More clearly shown in Fig 5.13, there is a distinct difference between the 5% and 5.5% samples compared to the others which correlates with the downturn in M(T) from chapter 4.

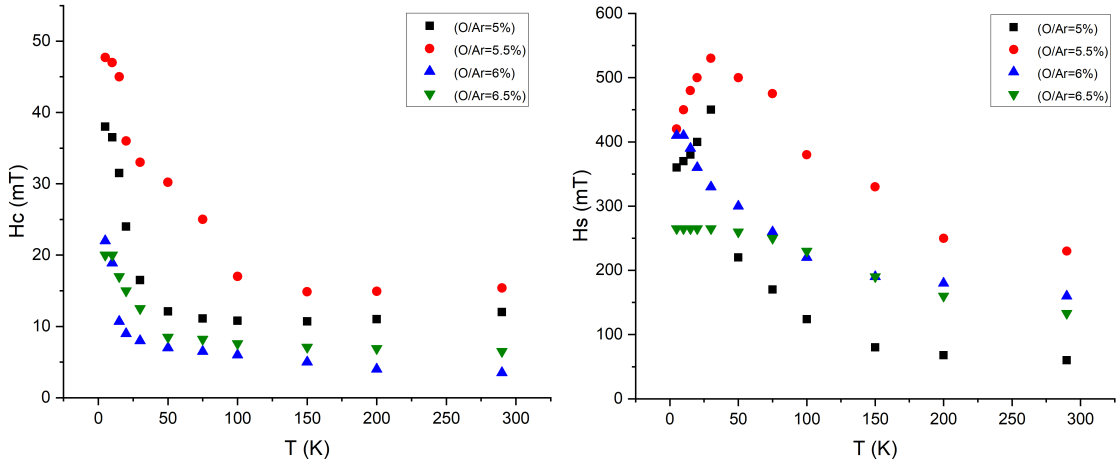

(a) (b)

Figure 5.13: The coercive field (H_c) as a function of temperature for 2 nm Pt deposited on 40 nm YIG with different oxygen content (a) and the saturation field (H_s) as a function of temperature, where the applied field is perpendicular to the charge current and the field is oriented out the plane of the sample.

Figure 5.14 and figure 5.15 show what we would expect to see. The longitudinal and transverse data show that the strange behaviour in figure 5.12 (b,d,f,and h) is due to the perpendicular anisotropy in YIG and is not seen in thick YIG.

Figure 5.16 shows The longitudinal magnetoresistance for 2 nm Pt on 40 nm YIG plotted as a function of applied magnetic field at different temperature. Figure 5.17 shows the coercive field (H_c) as a function of temperature for 2 nm Pt deposited on 40 nm YIG (a) and the saturation field (H_s) as a function of temperature, where the applied field is parallel to charge current and the field is oriented in the plane of the sample. The Oxygen content in YIG film was 6.5%.

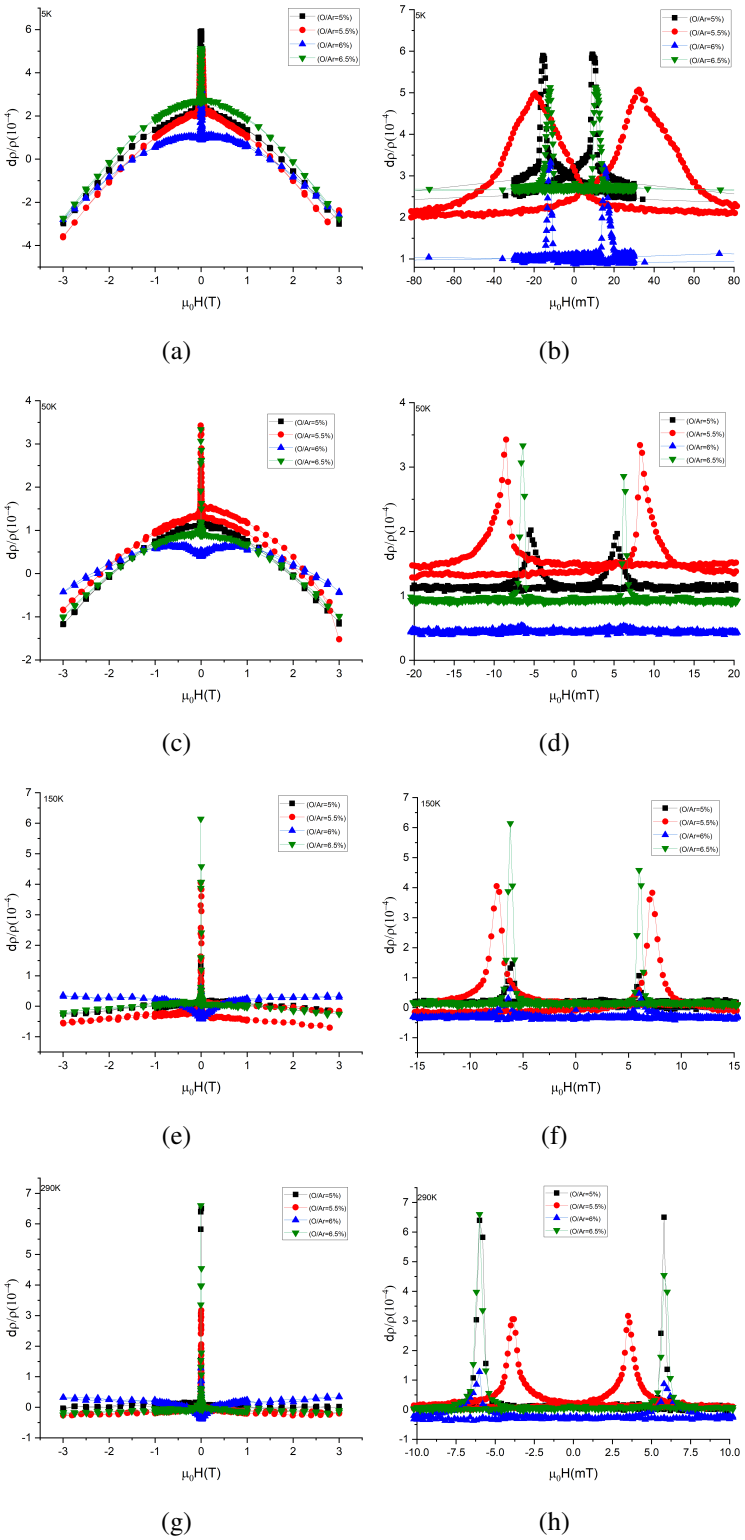

Figure 5.14: The transverse magnetoresistance for 2 nm Pt on 40 nm YIG plotted as a function of applied magnetic field at different temperature.

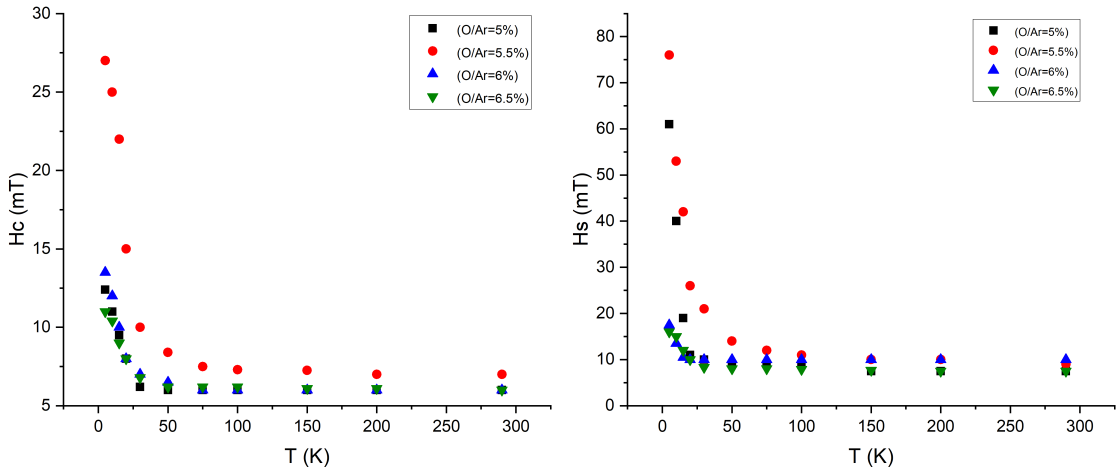

(a) (b)

Figure 5.15: The coercive field (H_c) as a function of temperature for 2 nm Pt deposited on 40 nm YIG with different oxygen content (a) and the saturation field (H_s) as a function of temperature, where the field is oriented in the plane of the sample.

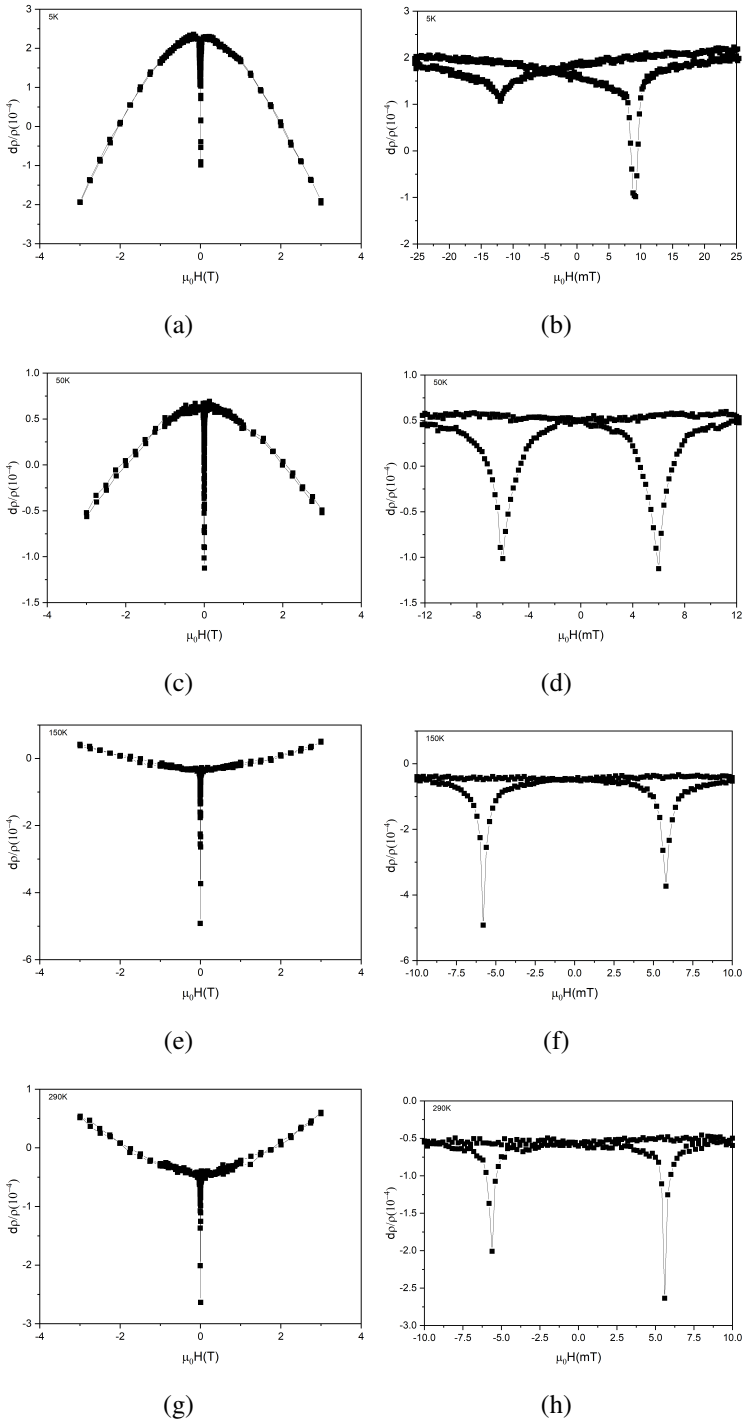

Figure 5.16: The longitudinal magnetoresistance for 2 nm Pt on 40 nm YIG plotted as a function of applied magnetic field at different temperature. (the Oxygen content in YIG film was 6.5%).

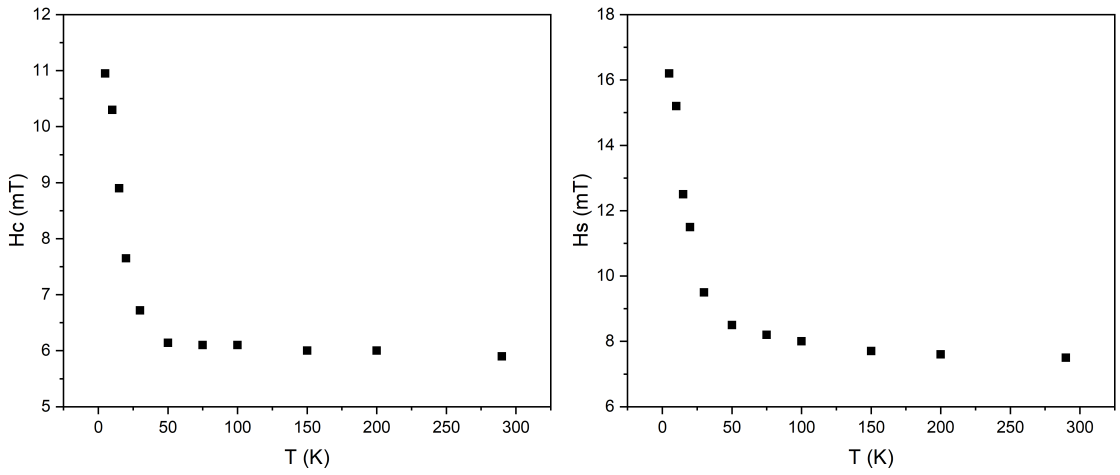

(a) (b)

Figure 5.17: The coercive field (H_c) as a function of temperature for 2 nm Pt deposited on 40 nm YIG (a) and the saturation field (H_s) as a function of temperature, where the applied field is parallel to charge current and the field is oriented in the plane of the sample.

Figure 5.18 enables us to measure the AMR. The AMR is caused by the spin-orbit interaction in ferromagnets and is usually positive when J (current density) is parallel to M (or H) and negative when J is perpendicular to M – this agrees with the data here. From the peak positions you can see there is no real anisotropy difference between the longitudinal and transverse directions.

Figure 5.19 shows the temperature dep of the AMR. It is unusual and more complicated than the AMR measured when the YIG is thick (170nm) which is monotonically increasing as T is lowered and disappears as a function of Pt thickness being much less than 1×10^{-4} for $t \sim 50$ nm [130].

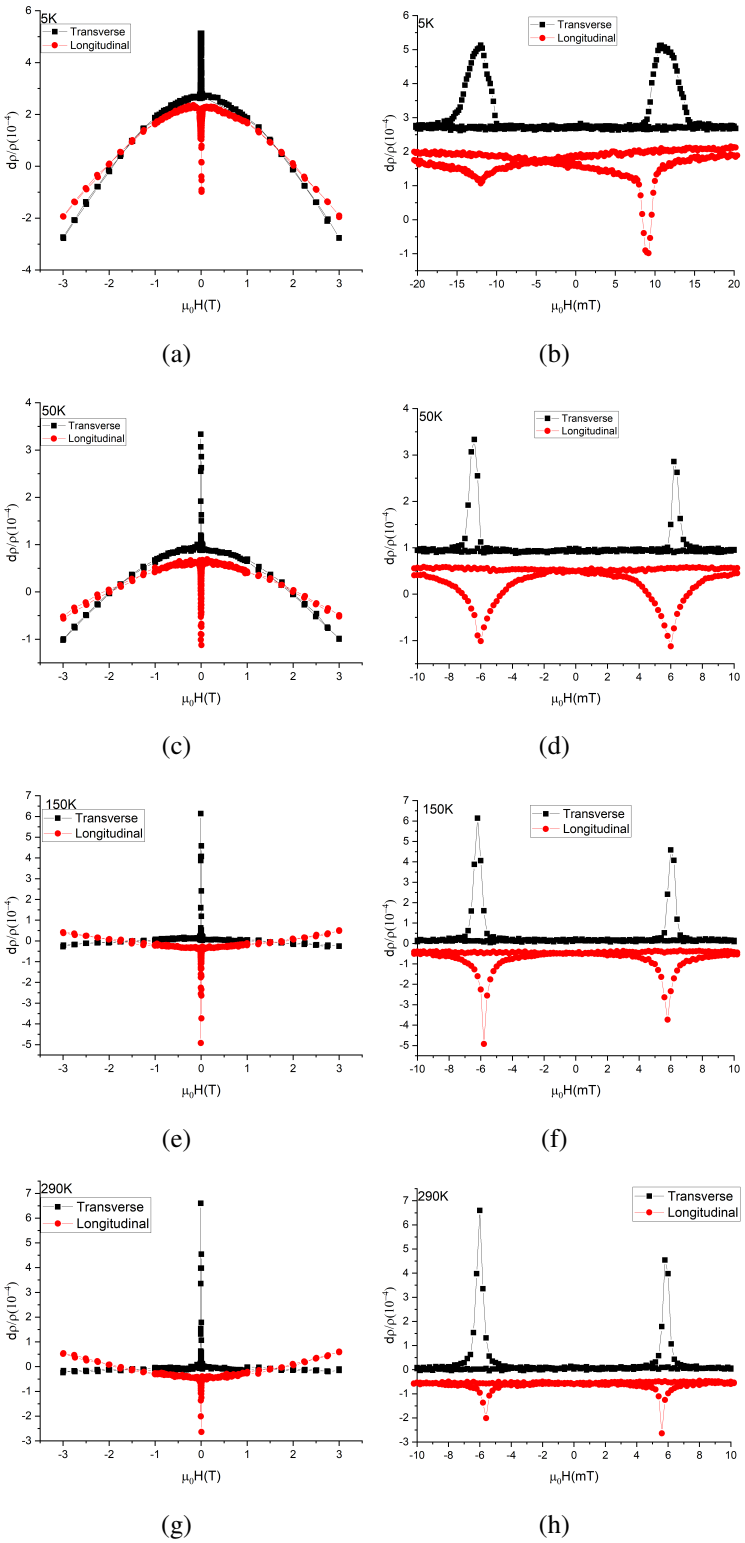

Figure 5.18: The longitudinal and transverse magnetoresistance for 2 nm Pt on 40 nm YIG plotted togather as a function of applied magnetic field at different temperature.

Figure 5.19 shows the MR from figure 5.18. The MR is the difference between the black peaks (transverse) and the red peaks (longitudinal) at low field. At low temperatures in figure 5.19 we see additional MR which could be due to the magnetic proximity effect in Pt at low temperatures.

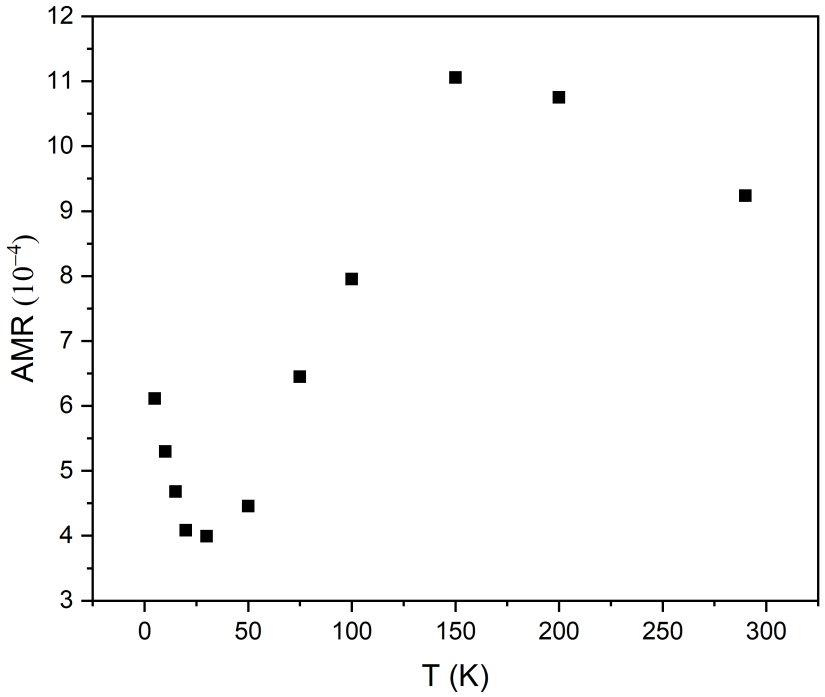

Figure 5.19: The MR from figure 5.18. The AMR is the difference between the black peaks (transverse) and the red peaks (longitudinal) at low field.

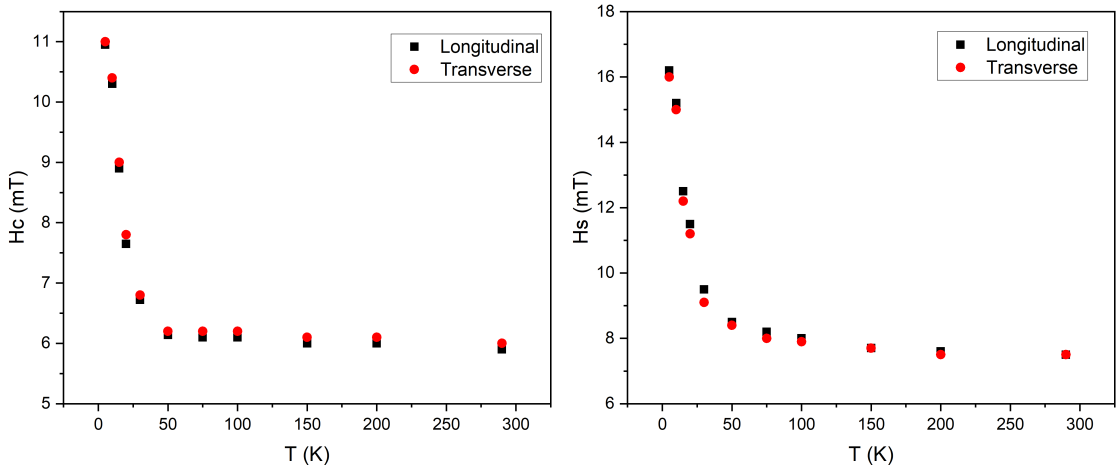

(a) (b)

Figure 5.20: The coercive field (H_c) as a function of temperature for 2 nm Pt deposited on 40 nm YIG (a) and the saturation field (H_s) as a function of temperature, for longitudinal and transverse orientations.

This data in figuer 5.21 shows that the high field region, beyond the saturation of YIG, is the same in all orientations. That is surprising because if this were due to WL we would expect the perpendicuar orientation to be much larger than the other two.

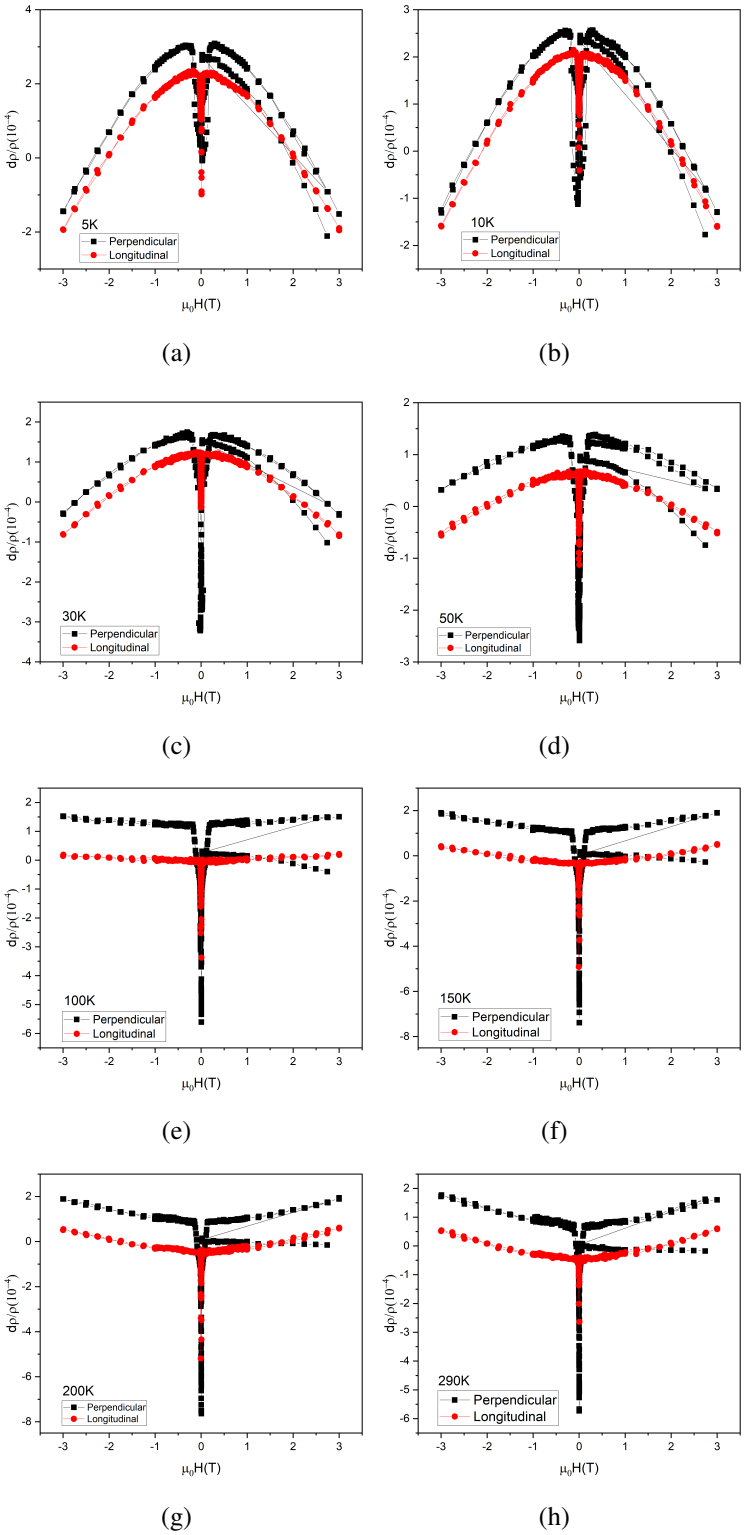

Figure 5.21: The longitudinal and perpendicular magnetoresistance for 2 nm Pt on 40 nm YIG plotted togather as a function of applied magnetic field at different temperature.

5.5 Conclusion

In this chapter, Pt was study by using the XRR, Bede fit was used to fit the XRR data to see the structural of our films. Also, AFM used to work out the thicknesses of Pt wires. Our results for Pt on YIG films confirmed that the thickness of Pt about 19-22 Å and the roughness about 4-5 Å.

The resistivity of Pt on YIG can be changed if the YIG has different oxygen contents. This is not fully understand but it could be due to the different oxygen contents in the YIG that may affect on the YIG/Pt inteface. We had a good fit for SHMR data. We did the fit in two different ways, the first way was we kept the spin mixing conductance constant, the other way was we kept the spin Hall angle a constant and varied the spin mixing conductance.

From the study on SHMR we have found very high values of the spin Hall angle, about 7% compared to the average value for Pt on YIG of 4%.

We have measured the MR in three different orientations. First, the perpendicular orientation, where the applied field is perpendicular to the plane of the sample, in this orientation the field is out of the plane of the sample. Second, the transverse orientation, where the field is perpendicular to the charge current but oriented in the plane of the sample. Third, the longitudinal orientation, where the applied field is parallel to charge current. We found the MR in all three orientations. At low temperatures, we found additional MR which could be due to the magnetic proximity effect in Pt at low temperatures. Also, we found that the different Oxygen contents in YIG films can be effect on interface between the YIG and Pt. There is a distinct difference between the 5% and 5.5% samples compared to the others which correlates with the downturn in M(T) from chapter 4.

CHAPTER 6

Conclusions and future work

6.1 Conclusions

The deposition of thin YIG films utilised GGG and YAG substrates at various oxygen contents to determine their appropriateness with regards to lattice strain at the YIG phase interface. Deposition onto YAG substrates was found to result in the YIG phase experiencing heightened lattice strain. The strain results from the two phases having mismatched lattices. Meanwhile, deposition onto GGG substrates resulted in thin YIG films with significantly reduced lattice strain. The various oxygen contents during sputtering was found to have a significant bearing on the composition of YIG when using films of GGG. For instance, we have a good quality YIG films on GGG when the oxygen contents was $\sim 6\%$, structural and magnetic properties are similar to those of bulk YIG.

The current study has demonstrated how on-axis RF magnetron sputtering can be used to grow nm-thick YIG films of excellent quality in a way that is replicable and achieves the features demanded of YIG. Magnetic, structural and SHMR measurements confirm that the resulting product is comparable to those produced using on- and off-axis sputtering and PLD. YIG films of nm thickness are suitable for use in a wide range of applications such as spin transfer torque, SHMR, spin pumping and magnonics.

Extensive analysis of the YIG films' morphology and crystallinity confirm that there is a 111 crystalline orientation and a 1-3 Å RMS surface roughness. Furthermore, YIG's lattice constant is similar to the bulk value (12.376 Å). Incorporating into the interface a Gd-mixed YIG layer achieves a x-ray reflectivity curve of annealed YIG that offers a good fit (GOF = 0.05). XRR data fitting confirms that the GGG and YIG densities have less than 1% divergence from the bulk values. It is during annealing at 850 °C that the interdiffusion layer forms.

Magnetometry was employed to provide a detailed assessment of the magnetic properties afforded by YIG with a 111-oriented GGG and YAG substrates. The GGG in conjunction with a heightened saturation field at room temperature results in Gd^{3+} ions that are responsible for achieving paramagnetism. This paramagnetism makes it

difficult to measure YIG's magnetic moment when the temperature is relatively low. At a temperature of 295 K, the saturation magnetisation of YIG films is 140 emu/cc, whilst the coercivity is just 0.30 ± 0.05 Oe. Having ascertained the saturation magnetic moment's thickness dependence, it is possible to verify that the interface's dead layer. The dead layer can thickness can be changed with changing the Oxygen contents as we see from VSM results and Bede fit as well. The problem with the original growth of YIG in our lab where a large downturn in M(T) was found has been overcome by adjusting the concentration of oxygen during growth. At 6% and 6.5% oxygen the magnetisation agrees with the bulk value and there is no downturn at low temperatures.

The process for growing YIG is the primary achievement resulting from the current study. The method has been devised in a way that ensures that consistent samples can be produced repeatedly, all of which serve as high quality material. From the analysis it is possible to confirm that the YIG produced can be applied to gauge the identical SHMR effect as that resulting from LPE. The same method has been applied in the empirical literature with regards to spin investigations. As such, the insight gained from the existing body of knowledge has contributed to advances in the growing of YIG, feeding through to research into spin currents relating to SHMR as well as alternative effects. YIG serves as a ferrimagnetic insulator and is therefore able to be applied in research into matters other than SHMR. From the study on SHMR we have found very high values of the spin Hall angle, about 7% compared to the average value for Pt on YIG of 4%. By standardising the method, it will be possible to replicate it in conventional condensed matter laboratories, thereby enabling greater scale to be achieved whilst simultaneously driving down the cost of conducting such research.

It is now known that the method employed when preparing the YIG interface has a significant bearing on magneto-transport in the bilayers of YIG and platinum. Resistivity as a function of temperature is at its lowest when the temperature is also low and this indicates a further contribution to weak localisation.

6.2 Future work

The findings of the current study effectively provide the groundwork for future research into growth optimisation and technically advanced approaches concerning bilayer YIG-based structures and YIG films that are RF sputtered.

Further research could conceivably help to refine the YIG process. Various experiments could be conducted to help better understand the stoichiometry such as STEM mapping in high resolution and XPS. There is certainly a need to enhance our understanding of the magnetisation qualities and there are gaps in our knowledge of thin film downturn. It is thought that the YIG elements and substrate diffuse over the interface but this has not yet been confirmed and nor is it known to what extent this occurs. Similarly, research is required to clarify the specific elements that combine and the depth to which they penetrate neighbouring materials. It is possible that utilising high-resolution STEM mapping could help to observe greater detail regarding the chemical composition over the interface. Measures of the bulk sample are ill-suited to examining a YIG film's bottom layer and, therefore, further research is necessary to apply a sensitive magnetometry approach to better understand the magnetic qualities of the bottom layer. PNR can be used to explore the magnetic 'dead' layer and it is believed that this dead layer is the result of a GdIG layer. There is also a need to further examine the NM and YIG interface. Chemical analysis can be conducted by TEM.

It is possible that changing the annealing temperature, applying a diffusion barrier to separate YIG and GGG, or utilising annealed GGG could result in films being produced that are of a superior quality. Future research should also investigate the use of off-axis sputtering with substrates of YAG and GGG when depositing YIG films. Magnetometry has been used extensively to help establish YIG's magnetic qualities. Further research is required whereby MFM is employed to micro-analyse the magnetic structure and provide detailed insight into the sample's inhomogeneous distribution of magnetisation because it is possible that this is associated with the results for SHMR.

We need to try off-axis sputtering to produce thin films of better quality. Different substrate to try and induce perpendicular anisotropy as that is probably useful for devices.

Thin YIG films play vital roles in magnonics and spintronics where minimal damping is required. Calculating the damping of the films will help to establish whether or not the damping is similar to that of bulk YIG. FMR could be employed to gauge the degree of damping in conjunction with an antenna of spectra under microwave.

REFERENCES

[1] J. D. Adam, L. E. Davis, G. F. Dionne, E. F. Schloemann, and S. N. Stitzer, "Ferrite devices and materials," *IEEE Transactions on Microwave Theory and Techniques*, vol. 50, no. 3, pp. 721–737, 2002.

[2] D. Bahadur, "Current trends in applications of magnetic ceramic materials," *Bulletin of Materials Science*, vol. 15, no. 5, pp. 431–439, 1992.

[3] E. Mallmann, A. Sombra, J. Goes, and P. Fechine, "Yttrium iron garnet: properties and applications review," in *Solid State Phenomena*, vol. 202, pp. 65–96, Trans Tech Publ, 2013.

[4] S. Geller and M. Gilleo, "Structure and ferrimagnetism of yttrium and rare-earth–iron garnets," *Acta Crystallographica*, vol. 10, no. 3, pp. 239–239, 1957.

[5] C. Vittoria and N. Wilsey, "Magnetostatic wave propagation losses in an anisotropic insulator," *Journal of Applied Physics*, vol. 45, no. 1, pp. 414–420, 1974.

[6] O. d'Allivy Kelly, A. Anane, R. Bernard, J. Ben Youssef, C. Hahn, A. H. Molpeceres, C. Carrétéro, E. Jacquet, C. Deranlot, P. Bortolotti, *et al.*, "Inverse spin hall effect in nanometer-thick yttrium iron garnet/pt system," *Applied Physics Letters*, vol. 103, no. 8, p. 082408, 2013.

[7] F. Bloch, "Zur theorie des ferromagnetismus," *Zeitschrift für Physik*, vol. 61, no. 3-4, pp. 206–219, 1930.

[8] A. V. Chumak, V. I. Vasyuchka, A. A. Serga, and B. Hillebrands, "Magnon spintronics," *Nature Physics*, vol. 11, no. 6, pp. 453–461, 2015.

[9] A. V. Chumak, A. A. Serga, and B. Hillebrands, "Magnon transistor for all-magnon data processing," *Nature communications*, vol. 5, no. 1, pp. 1–8, 2014.

[10] R. L. Stamps, S. Breitkreutz, J. Åkerman, A. V. Chumak, Y. Otani, G. E. Bauer, J.-U. Thiele, M. Bowen, S. A. Majetich, M. Kläui, *et al.*, "The 2014 magnetism roadmap," *Journal of Physics D: Applied Physics*, vol. 47, no. 33, p. 333001, 2014.

[11] P. Pirro, T. Brächer, A. Chumak, B. Lägel, C. Dubs, O. Surzhenko, P. Görnert, B. Leven, and B. Hillebrands, "Spin-wave excitation and propagation in microstructured waveguides of yttrium iron garnet/pt bilayers," *Applied Physics Letters*, vol. 104, no. 1, p. 012402, 2014.

[12] C. Hahn, V. Naletov, G. De Loubens, O. Klein, O. d'Allivy Kelly, A. Anane, R. Bernard, E. Jacquet, P. Bortolotti, V. Cros, *et al.*, "Measurement of the intrinsic damping constant in individual nanodisks of y3fe5o12 and y3fe5o12— pt," *Applied Physics Letters*, vol. 104, no. 15, p. 152410, 2014.

[13] N. F. Mott, "The electrical conductivity of transition metals," *Proceedings of the Royal Society of London. Series A-Mathematical and Physical Sciences*, vol. 153, no. 880, pp. 699–717, 1936.

[14] N. F. Mott, "The resistance and thermoelectric properties of the transition metals," *Proceedings of the Royal Society of London. Series A-Mathematical and Physical Sciences*, vol. 156, no. 888, pp. 368–382, 1936.

[15] M. N. Baibich, J. M. Broto, A. Fert, F. N. Van Dau, F. Petroff, P. Etienne, G. Creuzet, A. Friederich, and J. Chazelas, "Giant magnetoresistance of (001) fe/(001) cr magnetic superlattices," *Physical review letters*, vol. 61, no. 21, p. 2472, 1988.

[16] G. Binasch, P. Grünberg, F. Saurenbach, and W. Zinn, "Enhanced magnetoresistance in layered magnetic structures with antiferromagnetic interlayer exchange," *Physical review B*, vol. 39, no. 7, p. 4828, 1989.

[17] e. U. Hartmann, *Magnetic multilayers and giant magnetoresistance*, vol. 37. Springer-Verlag Berlin Heidelberg, 2000.

[18] H. S. E. Hirota and e. K. Inomata, *Giant magneto-resistance devices*, vol. 40. Springer-Verlag Berlin Heidelberg, 2002.

[19] J. Daughton, J. Brown, E. Chen, R. Beech, A. Pohm, and W. Kude, "Magnetic field sensors using gmr multilayer," *IEEE Transactions on magnetics*, vol. 30, no. 6, pp. 4608–4610, 1994.

[20] G. A. Prinz, "Magnetoelectronics," *Science*, vol. 282, no. 5394, pp. 1660–1663, 1998.

[21] M. Julliere, "Tunneling between ferromagnetic films," *Physics letters A*, vol. 54, no. 3, pp. 225–226, 1975.

[22] T. Miyazaki and N. Tezuka, "Giant magnetic tunneling effect in fe/al2o3/fe junction," *Journal of magnetism and magnetic materials*, vol. 139, no. 3, pp. 94–97, 1995.

[23] J. C. Slonczewski *et al.*, "Current-driven excitation of magnetic multilayers," *Journal of Magnetism and Magnetic Materials*, vol. 159, no. 1, p. L1, 1996.

[24] L. Berger, "Emission of spin waves by a magnetic multilayer traversed by a current," *Physical Review B*, vol. 54, no. 13, p. 9353, 1996.

[25] J. Slaughter, R. Dave, M. DeHerrera, M. Durlam, B. Engel, J. Janesky, N. Rizzo, and S. Tehrani, "Fundamentals of mram technology," *Journal of superconductivity*, vol. 15, no. 1, pp. 19–25, 2002.

[26] T. M. Maffitt, J. K. DeBrosse, J. Gabric, E. T. Gow, M. C. Lamorey, J. S. Parenteau, D. R. Willmott, M. A. Wood, and W. J. Gallagher, "Design considerations for mram," *IBM Journal of Research and Development*, vol. 50, no. 1, pp. 25–39, 2006.

[27] J. Katine, F. Albert, R. Buhrman, E. Myers, and D. Ralph, "Current-driven magnetization reversal and spin-wave excitations in co/cu/co pillars," *Physical review letters*, vol. 84, no. 14, p. 3149, 2000.

[28] S. S. Parkin, M. Hayashi, and L. Thomas, "Magnetic domain-wall racetrack memory," *Science*, vol. 320, no. 5873, pp. 190–194, 2008.

[29] S. Datta and B. Das, "Electronic analog of the electro-optic modulator," *Applied Physics Letters*, vol. 56, no. 7, pp. 665–667, 1990.

[30] H. C. Koo, J. H. Kwon, J. Eom, J. Chang, S. H. Han, and M. Johnson, "Control of spin precession in a spin-injected field effect transistor," *Science*, vol. 325, no. 5947, pp. 1515–1518, 2009.

[31] C. Betthausen, T. Dollinger, H. Saarikoski, V. Kolkovsky, G. Karczewski, T. Wojtowicz, K. Richter, and D. Weiss, "Spin-transistor action via tunable landau-zener transitions," *Science*, vol. 337, no. 6092, pp. 324–327, 2012.

[32] M. Kostylev, A. Serga, T. Schneider, B. Leven, and B. Hillebrands, "Spin-wave logical gates," *Applied Physics Letters*, vol. 87, no. 15, pp. 1–3, 2005.

[33] A. Serga, A. Chumak, and B. Hillebrands, "Yig magnonics," *Journal of Physics D: Applied Physics*, vol. 43, no. 26, p. 264002, 2010.

[34] V. Kruglyak, S. Demokritov, and D. Grundler, "Magnonics," *Journal of Physics D: Applied Physics*, vol. 43, no. 26, p. 264001, 2010.

[35] T. Schneider, A. A. Serga, B. Leven, B. Hillebrands, R. L. Stamps, and M. P. Kostylev, "Realization of spin-wave logic gates," *Applied Physics Letters*, vol. 92, no. 2, p. 022505, 2008.

[36] A. Khitun, M. Bao, and K. L. Wang, "Magnonic logic circuits," *Journal of Physics D: Applied Physics*, vol. 43, no. 26, p. 264005, 2010.

[37] T. Brächer, F. Heussner, P. Pirro, T. Fischer, M. Geilen, B. Heinz, B. Lägel, A. Serga, and B. Hillebrands, "Time-and power-dependent operation of a parametric spin-wave amplifier," *Applied Physics Letters*, vol. 105, no. 23, p. 232409, 2014.

[38] B. Lenk, H. Ulrichs, F. Garbs, and M. Münzenberg, "The building blocks of magnonics," *Physics Reports*, vol. 507, no. 4-5, pp. 107–136, 2011.

[39] V. E. Demidov, S. Urazhdin, and S. O. Demokritov, "Direct observation and mapping of spin waves emitted by spin-torque nano-oscillators," *Nature materials*, vol. 9, no. 12, pp. 984–988, 2010.

[40] M. Madami, S. Bonetti, G. Consolo, S. Tacchi, G. Carlotti, G. Gubbiotti, F. Mancoff, M. A. Yar, and J. Åkerman, "Direct observation of a propagating spin wave induced by spin-transfer torque," *Nature nanotechnology*, vol. 6, no. 10, p. 635, 2011.

[41] V. E. Demidov, S. Urazhdin, H. Ulrichs, V. Tiberkevich, A. Slavin, D. Baither, G. Schmitz, and S. O. Demokritov, "Magnetic nano-oscillator driven by pure spin current," *Nature materials*, vol. 11, no. 12, pp. 1028–1031, 2012.

[42] Y. Tserkovnyak, A. Brataas, and G. E. Bauer, "Enhanced gilbert damping in thin ferromagnetic films," *Physical review letters*, vol. 88, no. 11, p. 117601, 2002.

[43] M. Costache, M. Sladkov, S. Watts, C. Van Der Wal, and B. Van Wees, "Electrical detection of spin pumping due to the precessing magnetization of a single ferromagnet," *Physical review letters*, vol. 97, no. 21, pp. 1–4, 2006.

[44] J. Hirsch, "Spin hall effect," *Physical review letters*, vol. 83, no. 9, p. 1834, 1999.

[45] E. Saitoh, M. Ueda, H. Miyajima, and G. Tatara, "Conversion of spin current into charge current at room temperature: Inverse spin-hall effect," *Applied physics letters*, vol. 88, no. 18, p. 182509, 2006.

[46] S. Zhang, "Spin hall effect in the presence of spin diffusion," *Physical review letters*, vol. 85, no. 2, p. 393, 2000.

[47] Y. Kajiwara, K. Harii, S. Takahashi, J.-i. Ohe, K. Uchida, M. Mizuguchi, H. Umezawa, H. Kawai, K. Ando, K. Takanashi, *et al.*, "Transmission of electrical signals by spin-wave interconversion in a magnetic insulator," *Nature*, vol. 464, no. 7286, pp. 262–266, 2010.

[48] J. C. Slonczewski, "Initiation of spin-transfer torque by thermal transport from magnons," *Physical Review B*, vol. 82, no. 5, pp. 1–11, 2010.

[49] K.-i. Uchida, J. Xiao, H. Adachi, J.-i. Ohe, S. Takahashi, J. Ieda, T. Ota, Y. Kajiwara, H. Umezawa, H. Kawai, *et al.*, "Spin seebeck insulator," *Nature materials*, vol. 9, no. 11, pp. 894–897, 2010.

[50] A. G. Gurevich and G. A. Melkov, *Magnetization oscillations and waves*. CRC press, 1996.

[51] K.-i. Uchida, T. Kikkawa, A. Miura, J. Shiomi, and E. Saitoh, "Quantitative temperature dependence of longitudinal spin seebeck effect at high temperatures," *Physical Review X*, vol. 4, no. 4, pp. 1–9, 2014.

[52] X. Jia, K. Liu, K. Xia, and G. E. Bauer, "Spin transfer torque on magnetic insulators," *EPL (Europhysics Letters)*, vol. 96, no. 1, p. 17005, 2011.

[53] C. Du, H. Wang, F. Yang, and P. C. Hammel, "Systematic variation of spin-orbit coupling with d-orbital filling: Large inverse spin hall effect in 3 d transition metals," *Physical Review B*, vol. 90, no. 14, pp. 1–5, 2014.

[54] H. Jin, S. R. Boona, Z. Yang, R. C. Myers, and J. P. Heremans, "Effect of the magnon dispersion on the longitudinal spin seebeck effect in yttrium iron garnets," *Physical Review B*, vol. 92, no. 5, p. 054436, 2015.

[55] D. Sanders and D. Walton, "Effect of magnon-phonon thermal relaxation on heat transport by magnons," *Physical Review B*, vol. 15, no. 3, p. 1489, 1977.

[56] T. Kikkawa, K.-i. Uchida, S. Daimon, Z. Qiu, Y. Shiomi, and E. Saitoh, "Critical suppression of spin seebeck effect by magnetic fields," *Physical Review B*, vol. 92, no. 6, pp. 1–9, 2015.

[57] H. Wang, C. Du, Y. Pu, R. Adur, P. C. Hammel, and F. Yang, "Scaling of spin hall angle in 3d, 4d, and 5d metals from y 3 fe 5 o 12/metal spin pumping," *Physical review letters*, vol. 112, no. 19, pp. 1–5, 2014.

[58] C. Du, H. Wang, Y. Pu, T. Meyer, P. Woodward, F. Yang, and P. Hammel, "Probing the spin pumping mechanism: Exchange coupling with exponential decay in y 3 fe 5 o 12/barrier/pt heterostructures," *Physical review letters*, vol. 111, no. 24, pp. 1–5, 2013.

[59] C. Du, H. Wang, F. Yang, and P. C. Hammel, "Enhancement of pure spin currents in spin pumping y 3 fe 5 o 12/cu/metal trilayers through spin conductance matching," *Physical Review Applied*, vol. 1, no. 4, 2014.

[60] H. Wang, C. Du, P. Chris Hammel, and F. Yang, "Spin current and inverse spin hall effect in ferromagnetic metals probed by y3fe5o12-based spin pumping," *Applied Physics Letters*, vol. 104, no. 20, 2014.

[61] T. Chiba, G. E. Bauer, and S. Takahashi, "Spin torque transistor revisited," *Applied Physics Letters*, vol. 102, no. 19, 2013.

[62] M. Jungfleisch, V. Lauer, R. Neb, A. Chumak, and B. Hillebrands, "Improvement of the yttrium iron garnet/platinum interface for spin pumping-based applications," *Applied Physics Letters*, vol. 103, no. 2, pp. 2011–2015, 2013.

[63] Y. Sun, H. Chang, M. Kabatek, Y.-Y. Song, Z. Wang, M. Jantz, W. Schneider, M. Wu, E. Montoya, B. Kardasz, *et al.*, "Damping in yttrium iron garnet nanoscale films capped by platinum," *Physical Review Letters*, vol. 111, no. 10, 2013.

[64] S. Rezende, R. Rodríguez-Suárez, M. Soares, L. Vilela-Leão, D. Ley Domínguez, and A. Azevedo, "Enhanced spin pumping damping in yttrium iron garnet/pt bilayers," *Applied Physics Letters*, vol. 102, no. 1, pp. 1–4, 2013.

[65] Y. Sun, Y.-Y. Song, H. Chang, M. Kabatek, M. Jantz, W. Schneider, M. Wu, H. Schultheiss, and A. Hoffmann, "Growth and ferromagnetic resonance properties of nanometer-thick yttrium iron garnet films," *Applied Physics Letters*, vol. 101, no. 15, p. 082405, 2012.

[66] N. Kumar, D. Misra, N. Venkataramani, S. Prasad, and R. Krishnan, "Magnetic properties of pulsed laser ablated yig thin films on different substrates," *Journal of Magnetism and Magnetic Materials*, vol. 272, pp. E899–E900, 2004.

[67] E. Popova, N. Keller, F. Gendron, M. Guyot, M.-C. Brianso, Y. Dumond, and M. Tessier, "Structure and magnetic properties of yttrium–iron–garnet thin films prepared by laser deposition," *Journal of Applied Physics*, vol. 90, no. 3, pp. 1422–1428, 2001.

[68] N. Sokolov, V. Fedorov, A. Korovin, S. Suturin, D. Baranov, S. Gastev, B. Krichevtsov, K. Y. Maksimova, A. Grunin, V. Bursian, *et al.*, "Thin yttrium iron garnet films grown by pulsed laser deposition: Crystal structure, static, and dynamic magnetic properties," *Journal of Applied Physics*, vol. 119, no. 2, 2016.

[69] M. Haidar, M. Ranjbar, M. Balinsky, R. Dumas, S. Khartsev, and J. Åkerman, "Thickness-and temperature-dependent magnetodynamic properties of yttrium iron garnet thin films," *Journal of Applied Physics*, vol. 117, no. 17, 2015.

[70] L. Lutsev, A. Korovin, V. Bursian, S. Gastev, V. Fedorov, S. Suturin, and N. Sokolov, "Low-relaxation spin waves in laser-molecular-beam epitaxy grown nanosized yttrium iron garnet films," *Applied Physics Letters*, vol. 108, no. 18, 2016.

[71] A. Kaveev, V. Bursian, S. Gastev, B. Krichevtsov, S. Suturin, M. Volkov, and N. Sokolov, "Laser mbe-grown yttrium iron garnet films on gan: characterization of the crystal structure and magnetic properties," *Materials Research Express*, vol. 3, no. 7, 2016.

[72] C. Hauser, T. Richter, N. Homonnay, C. Eisenschmidt, M. Qaid, H. Deniz, D. Hesse, M. Sawicki, S. G. Ebbinghaus, and G. Schmidt, "Yttrium iron garnet thin films with very low damping obtained by recrystallization of amorphous material," *Scientific reports*, vol. 6, pp. 1–13, 2016.

[73] J. Lustikova, Y. Shiomi, Z. Qiu, T. Kikkawa, R. Iguchi, K. Uchida, and E. Saitoh, "Spin current generation from sputtered y3fe5o12 films," *Journal of Applied Physics*, vol. 116, no. 15, p. 153902, 2014.

[74] H. Wang, C. Du, Y. Pu, R. Adur, P. Hammel, and F. Yang, "Large spin pumping from epitaxial y 3 fe 5 o 12 thin films to pt and w layers," *Physical Review B*, vol. 88, no. 10, pp. 1–5, 2013.

[75] Y.-M. Kang, S.-H. Wee, S.-I. Baik, S.-G. Min, S.-C. Yu, S.-H. Moon, Y.-W. Kim, and S.-I. Yoo, "Magnetic properties of yig (y 3 fe 5 o 12) thin films prepared by the post annealing of amorphous films deposited by rf-magnetron sputtering," *Journal of applied physics*, vol. 97, no. 10, p. 10A319, 2005.

[76] T. Liu, H. Chang, V. Vlaminck, Y. Sun, M. Kabatek, A. Hoffmann, L. Deng, and M. Wu, "Ferromagnetic resonance of sputtered yttrium iron garnet nanometer films," *Journal of Applied Physics*, vol. 115, no. 17, pp. 2014–2017, 2014.

[77] H. Nakayama, M. Althammer, Y.-T. Chen, K. Uchida, Y. Kajiwara, D. Kikuchi, T. Ohtani, S. Geprägs, M. Opel, S. Takahashi, R. Gross, G. E. W. Bauer, S. T. B. Goennenwein, and E. Saitoh, "Spin hall magnetoresistance induced by a nonequilibrium proximity effect," *Phys. Rev. Lett.*, vol. 110, p. 206601, May 2013.

[78] Y.-T. Chen, S. Takahashi, H. Nakayama, M. Althammer, S. T. B. Goennenwein, E. Saitoh, and G. E. W. Bauer, "Theory of spin hall magnetoresistance (smr) and related phenomena," *J. Phys. Condens. Matter*, vol. 28, no. 10, p. 103004, 2016.

[79] C. O. Avci, K. Garello, A. Ghosh, M. Gabureac, S. F. Alvarado, and P. Gambardella, "Unidirectional spin hall magnetoresistance in ferromagnet/normal metal bilayers," *Nat Phys*, vol. 11, pp. 570–575, July 2015.

[80] R. Iguchi, K. Sato, D. Hirobe, S. Daimon, and E. Saitoh, "Effect of spin hall magnetoresistance on spin pumping measurements in insulating magnet/metal systems," *Appl. Phys. Express*, vol. 7, p. 013003, Dec 2014.

[81] S. Wang, L. Zou, X. Zhang, J. Cai, S. Wang, B. Shen, and J. Sun, "Spin seebeck effect and spin hall magnetoresistance at high temperatures for a pt/yttrium iron garnet hybrid structure," *Nanoscale*, vol. 7, pp. 17812–17819, 2015.

[82] M. Althammer, S. Meyer, H. Nakayama, M. Schreier, S. Altmannshofer, M. Weiler, H. Huebl, S. Geprägs, M. Opel, R. Gross, D. Meier, C. Klewe, T. Kuschel, J.-M. Schmalhorst, G. Reiss, L. Shen, A. Gupta, Y.-T. Chen, G. E. W. Bauer, E. Saitoh, and S. T. B. Goennenwein, "Quantitative study of the spin hall magnetoresistance in ferromagnetic insulator/normal metal hybrids," *Phys. Rev. B*, vol. 87, p. 224401, Jun 2013.

[83] J. H. Han, Y. Y. Wang, Q. H. Yang, G. Y. Wang, F. Pan, and C. Song, "Spin hall magnetoresistance in nb/y3fe5o12 hybrids," *Phys. Status Solidi Rapid Res. Lett.*, vol. 9, no. 6, pp. 371–374, 2015.

[84] D. Jiles, *Introduction to magnetism and magnetic materials*. CRC press, 2015.

[85] R. C. O'handley, *Modern magnetic materials: principles and applications*. Wiley, 2000.

[86] F. Bertaut and F. Forrat, "Structure of ferrimagnetic rare-earth ferrites," *CR Acad. Sci*, vol. 242, p. 382, 1956.

[87] P. Wigen, R. McMichael, and C. Jayaprakash, "Route to chaos in the magnetic garnets," *Journal of magnetism and magnetic materials*, vol. 84, no. 3, pp. 237–246, 1990.

[88] A. Prabhakar and D. D. Stancil, *Spin waves: Theory and applications*, vol. 5. Springer, 2009.

[89] M. Sparks, *Ferromagnetic-relaxation theory*. McGraw-Hill, 1964.

[90] M. Jungfleisch, *Wellenvektoraufgelöste Brillouin-Lichtstreuspektroskopie an nichtlinearen Spinwellen*. PhD thesis, Diplomarbeit, Technische Universität Kaiserslautern, 2009.

[91] M. Gilleo and S. Geller, "Magnetic and crystallographic properties of substituted yttrium-iron garnet, 3 y 2 o 3· x m 2 o 3·(5- x) fe 2 o 3," *Physical Review*, vol. 110, no. 1, p. 73, 1958.

[92] Z. Celinski and B. Heinrich, "Ferromagnetic resonance linewidth of fe ultrathin films grown on a bcc cu substrate," *Journal of Applied Physics*, vol. 70, no. 10, pp. 5935–5937, 1991.

[93] K. Fuchs, "The conductivity of thin metallic films according to the electron theory of metals," in *Mathematical Proceedings of the Cambridge Philosophical Society*, vol. 34, pp. 100–108, Cambridge University Press, 1938.

[94] J. D. Jackson, "Classical electrodynamics 3rd edition," *Cited on*, 1998.

[95] I. Grant and W. Phillips, *Electromagnetism*. Manchester Physics Series, Wiley, 1991.

[96] e. E. S. Katsuaki Sato, *Spintronics for next generation innovative devices*. Wiley Online Library, 2015.

[97] S. Maekawa, S. Valenzuela, E. Saitoh, and T. Kimura, *Spin Current*. Series on Semiconductor Science and Technology, OUP Oxford, 2012.

[98] I. Žutić, J. Fabian, and S. D. Sarma, "Spintronics: Fundamentals and applications," *Reviews of modern physics*, vol. 76, no. 2, p. 323, 2004.

[99] R. . J. Elliott, "Theory of the effect of spin-orbit coupling on magnetic resonance in some semiconductors," *Physical Review*, vol. 96, no. 2, p. 266, 1954.

[100] Y. Yafet and V. Jaccarino, "Nuclear spin relaxation in transition metals; core polarization," *Physical Review*, vol. 133, no. 6A, p. A1630, 1964.

[101] M. Onbasli, A. Kehlberger, D. H. Kim, G. Jakob, M. Kläui, A. V. Chumak, B. Hillebrands, and C. A. Ross, "Pulsed laser deposition of epitaxial yttrium iron garnet films with low gilbert damping and bulk-like magnetization," *Apl Materials*, vol. 2, no. 10, p. 106102, 2014.

[102] H. Chang, P. Li, W. Zhang, T. Liu, A. Hoffmann, L. Deng, and M. Wu, "Nanometer-thick yttrium iron garnet films with extremely low damping," *IEEE Magnetics Letters*, vol. 5, pp. 1–4, 2014.

[103] M. Zwierzycki, Y. Tserkovnyak, P. J. Kelly, A. Brataas, and G. E. Bauer, "First-principles study of magnetization relaxation enhancement and spin transfer in thin magnetic films," *Physical Review B*, vol. 71, no. 6, p. 064420, 2005.

[104] Y.-T. Chen, S. Takahashi, H. Nakayama, M. Althammer, S. T. Goennenwein, E. Saitoh, and G. E. Bauer, "Theory of spin hall magnetoresistance," *Physical Review B*, vol. 87, no. 14, p. 144411, 2013.

[105] H. Nakayama, M. Althammer, Y.-T. Chen, K.-i. Uchida, Y. Kajiwara, D. Kikuchi, T. Ohtani, S. Geprägs, M. Opel, S. Takahashi, *et al.*, "Spin hall magnetoresistance induced by a nonequilibrium proximity effect," *Physical review letters*, vol. 110, no. 20, p. 206601, 2013.

[106] E. H. Hall *et al.*, "On a new action of the magnet on electric currents," *American Journal of Mathematics*, vol. 2, no. 3, pp. 287–292, 1879.

[107] J. Hook, "He hall," *Solid State Physics Second Edition John Wiley & Sons Ltd*, p. 160, 1991.

[108] C. Hurd, "Hall effect in metal and alloys. plenum press," *New York*, 1972.

[109] e. S. P. Helmut Kronmuller, *Handbook of Magnetism and Advanced Magnetic Materials. Wiley-Blackwell,*. 2007.

[110] M. I. D'Yakonov and V. Perel, "Possibility of orienting electron spins with current," *JETPL*, vol. 13, p. 467, 1971.

[111] M. I. Dyakonov and V. Perel, "Current-induced spin orientation of electrons in semiconductors," *Physics Letters A*, vol. 35, no. 6, pp. 459–460, 1971.

[112] N. Stern, S. Ghosh, G. Xiang, M. Zhu, N. Samarth, and D. Awschalom, "Current-induced polarization and the spin hall effect at room temperature," *Physical review letters*, vol. 97, no. 12, pp. 1–4, 2006.

[113] Y. K. Kato, R. C. Myers, A. C. Gossard, and D. D. Awschalom, "Observation of the spin hall effect in semiconductors," *science*, vol. 306, no. 5703, pp. 1910–1913, 2004.

[114] J. Wunderlich, B. Kaestner, J. Sinova, and T. Jungwirth, "Experimental observation of the spin-hall effect in a two-dimensional spin-orbit coupled semiconductor system," *Physical review letters*, vol. 94, no. 4, pp. 1–4, 2005.

[115] V. Sih, R. Myers, Y. Kato, W. Lau, A. Gossard, and D. Awschalom, "Spatial imaging of the spin hall effect and current-induced polarization in two-dimensional electron gases," *Nature Physics*, vol. 1, no. 1, pp. 31–35, 2005.

[116] S. O. Valenzuela and M. Tinkham, "Direct electronic measurement of the spin hall effect," *Nature*, vol. 442, no. 7099, pp. 176–179, 2006.

[117] T. Kimura, Y. Otani, T. Sato, S. Takahashi, and S. Maekawa, "Room-temperature reversible spin hall effect," *Physical review letters*, vol. 98, no. 15, pp. 1–4, 2007.

[118] T. Tanaka, H. Kontani, M. Naito, T. Naito, D. S. Hirashima, K. Yamada, and J. Inoue, "Intrinsic spin hall effect and orbital hall effect in 4 d and 5 d transition metals," *Physical Review B*, vol. 77, no. 16, pp. 1–16, 2008.

[119] R. Winkler, S. Papadakis, E. De Poortere, and M. Shayegan, *Spin-Orbit Coupling in Two-Dimensional Electron and Hole Systems*, vol. 41. Springer, 2003.

[120] G. Vignale, "Ten years of spin hall effect," *Journal of superconductivity and novel magnetism*, vol. 23, no. 1, pp. 3–10, 2010.

[121] A. Mitra, *Structural and magnetic properties of YIG thin films and interfacial origin of magnetisation suppression*. PhD thesis, University of Leeds, 2017.

[122] R. Karplus and J. Luttinger, "Hall effect in ferromagnetics," *Physical Review*, vol. 95, no. 5, pp. 1154–1160, 1954.

[123] L. Berger, "Side-jump mechanism for the hall effect of ferromagnets," *Physical Review B*, vol. 2, no. 11, pp. 4559–4566, 1970.

[124] N. Mott and H. Massey, "The theory of atomic collisions. international series of monographs on physics. international series of monographs on physics (oxford, england), oxford; 3rd edition (november 1965)," 1965.

[125] L. D. Landau and E. M. Lifshitz, *Quantum mechanics: non-relativistic theory*, vol. 3. WILEY-VCH, 1964.

[126] S. Lyo and T. Holstein, "Side-jump mechanism for ferromagnetic hall effect," *Physical Review Letters*, vol. 29, no. 7, pp. 423–425, 1972.

[127] S. Takahashi and S. Maekawa, "Spin current, spin accumulation and spin hall effect," *Science and Technology of Advanced Materials*, vol. 9, no. 1, p. 014105, 2008.

[128] K. Ando, S. Takahashi, J. Ieda, Y. Kajiwara, H. Nakayama, T. Yoshino, K. Harii, Y. Fujikawa, M. Matsuo, S. Maekawa, *et al.*, "Inverse spin-hall effect induced by spin pumping in metallic system," *Journal of applied physics*, vol. 109, no. 10, p. 103913, 2011.

[129] S. R. Marmion, *Comparison of spin Hall magnetoresistance temperature dependence in YIG/metal systems*. PhD thesis, University of Leeds, 2016.

[130] S. Alotibi, B. J. Hickey, G. Teobaldi, M. Ali, J. Barker, E. Poli, D. D. O'Regan, Q. Ramasse, G. Burnell, J. Patchett, *et al.*, "Enhanced spin–orbit coupling in heavy metals via molecular coupling," *ACS Applied Materials & Interfaces*, vol. 13, no. 4, pp. 5228–5234, 2021.

[131] E. H. Sondheimer, "The mean free path of electrons in metals," *Advances in physics*, vol. 1, no. 1, p. 1, 1952.

[132] D. Schumacher, "New evidence for the validity of the fuchs-sondheimer theory," *Thin Solid Films*, vol. 152, no. 3, pp. 499–510, 1987.

[133] J. Dugdale, "Structures and properties of solids," *The Electrical Properties of Metals and Alloys*, vol. 5, 1977.

[134] A. Mayadas and M. Shatzkes, "Electrical-resistivity model for polycrystalline films: the case of arbitrary reflection at external surfaces," *Physical review B*, vol. 1, no. 4, p. 1382, 1970.

[135] J. M. Ziman and J. M. Ziman, *Electrons and phonons: the theory of transport phenomena in solids*. Oxford university press, 1960.

[136] M. Kohler, "Zur magnetischen widerstandsänderung reiner metalle," *Annalen der Physik*, vol. 424, no. 1-2, pp. 211–218, 1938.

[137] M.-T. Béal-Monod and R. Weiner, "Negative magnetoresistivity in dilute alloys," *Physical Review*, vol. 170, no. 2, p. 552, 1968.

[138] H. Wang, C. Du, P. C. Hammel, and F. Yang, "Strain-tunable magnetocrystalline anisotropy in epitaxial y 3 fe 5 o 12 thin films," *Physical Review B*, vol. 89, no. 13, p. 134404, 2014.

[139] H. Arend and J. Hulliger, *Crystal Growth in Science and Technology*. Springer US, 2012.

[140] F. Miller, A. Vandome, and M. John, *Czochralski Process*. VDM Publishing, 2010.

[141] R. F. Bryan, "Handbook of crystal growth. vol. 3: Thin films and epitaxy," *J. Appl. Crystallogr.*, vol. 30, p. 419, Jun 1997.

[142] S. Kostić, Z. Ž. Lazarević, V. Radojević, A. Milutinović, M. Romčević, N. Ž. Romčević, and A. Valčić, "Study of structural and optical properties of yag and nd:yag single crystals," *Materials Research Bulletin*, vol. 63, pp. 80–87, 3 2015.

[143] K. Wasa, M. Kitabatake, and H. Adachi, *Thin film materials technology: sputtering of control compound materials*. William Andrew, 2004.

[144] D. Windover, E. Barnat, J. Kim, M. Nielsen, T. Lu, A. Kumar, H. Bakhru, C. Jin, and S. Lee, "Thin film density determination by multiple radiation energy dispersive x-ray reflectivity," *International Centre for Diffraction Data, Advances in X-ray Analysis*, vol. 42, pp. 590–600, 2000.

[145] J. Als-Nielsen and D. McMorrow, *Elements of modern X-ray physics*. John Wiley & Sons, 2001.

[146] H. Kiessig, "Untersuchungen zur totalreflexion von röntgenstrahlen," *Annalen der Physik*, vol. 402, no. 6, pp. 715–768, 1931.

[147] U. Pietsch, V. Holy, and T. Baumbach, *High-resolution X-ray scattering: from thin films to lateral nanostructures*. Springer Science & Business Media, 2004.

[148] D. Bowen and B. Tanner, "Characterization of engineering surfaces by grazing-incidence x-ray reflectivity," *Nanotechnology*, vol. 4, no. 4, p. 175, 1993.

[149] L. G. Parratt, "Surface studies of solids by total reflection of x-rays," *Physical review*, vol. 95, no. 2, p. 359, 1954.

[150] N. Porter, *Magnetoresistance in n-type Silicon*. PhD thesis, University of Leeds, 2010.

[151] G. Aviv, "Squids-superconducting quantum interference devices," *Department of Physics, Ben-Gurion University of the Negev, PO Box 653, Be'er-Sheva 84105, Israel*, 2008.

[152] C. Graham, "High-sensitivity magnetization measurements," *Journal of Materials Sciences and Technology*, no. 2, pp. 97–101, 2000.

[153] J. Clarke and A. I. Braginski, *The SQUID Handbook*. Wiley VCH, 2005.

[154] G. Binnig, C. F. Quate, and C. Gerber, "Atomic force microscope," *Physical review letters*, vol. 56, no. 9, pp. 930–933, 1986.

[155] A. San Paulo and R. Garcia, "Unifying theory of tapping-mode atomic-force microscopy," *Physical Review B*, vol. 66, no. 4, p. 041406, 2002.

[156] R. Garcıa and R. Perez, "Dynamic atomic force microscopy methods," *Surface science reports*, vol. 47, no. 6-8, pp. 197–301, 2002.

[157] N. Jalili and K. Laxminarayana, "A review of atomic force microscopy imaging systems: application to molecular metrology and biological sciences," *Mechatronics*, vol. 14, no. 8, pp. 907–945, 2004.

[158] S. M. A. Alghamdi, *Tuneable magnetic properties of 3D transition metals using carbon allotropes*. PhD thesis, University of Leeds, 2019.

[159] A. L. Westerman, *Extrinsic spin-orbit scattering in thin films*. PhD thesis, University of Leeds, 2019.

[160] H. Nakayama, M. Althammer, Y. Chen, K. Uchida, Y. Kajiwara, D. Kikuchi, T. Ohtani, M. O. S. T. R. G. G. B. S. G. Geprags, S, and E. Saitoh, "Spin hall magnetoresistance induced by a nonequilibrium proximity effect," *Phys. Rev. Lett*, vol. 110, p. 206601, 2013.

[161] B. Miao, S. Huang, D. Qu, and C. Chien, "Physical origins of the new magnetoresistance in pt/yig," *Physical review letters*, vol. 112, no. 23, p. 236601, 2014.

[162] B. Bhoi, N. Venkataramani, R. Aiyar, and S. Prasad, "Fmr and magnetic studies on polycrystalline yig thin films deposited using pulsed laser," *IEEE transactions on magnetics*, vol. 49, no. 3, pp. 990–994, 2013.

[163] H. Nelson, "Liquid-phase epitaxy—its role in crystal growth technology," *Journal of Crystal Growth*, vol. 27, pp. 1–5, 1974.

[164] W. Tolksdorf, H. Dammann, E. Pross, B. Strocka, H. Tolle, and P. Willich, "Growth of yttrium iron garnet multi-layers by liquid phase epitaxy for single mode magneto-optic waveguides," *Journal of crystal growth*, vol. 83, no. 1, pp. 15–22, 1987.

[165] T. Aichele, A. Lorenz, R. Hergt, and P. Görnert, "Garnet layers prepared by liquid phase epitaxy for microwave and magneto-optical applications–a review," *Crystal Research and Technology: Journal of Experimental and Industrial Crystallography*, vol. 38, no. 7-8, pp. 575–587, 2003.

[166] R. Karim, S. Oliver, and C. Vittoria, "Laser ablation deposition of yig films on semiconductor and amorphous substrates," *IEEE Transactions on Magnetics*, vol. 31, no. 6, pp. 3485–3487, 1995.

[167] A. Sposito, T. May-Smith, G. Stenning, P. De Groot, and R. Eason, "Pulsed laser deposition of high-quality μm-thick yig films on yag," *Optical Materials Express*, vol. 3, no. 5, pp. 624–632, 2013.

[168] P. Dorsey, S. Bushnell, R. Seed, and C. Vittoria, "Epitaxial yttrium iron garnet films grown by pulsed laser deposition," *Journal of Applied Physics*, vol. 74, no. 2, pp. 1242–1246, 1993.

[169] A. M. Zaki, H. J. Blythe, S. M. Heald, A. M. Fox, and G. A. Gehring, "Growth of high quality yttrium iron garnet films using standard pulsed laser deposition technique," *Journal of Magnetism and Magnetic Materials*, vol. 453, pp. 254–257, 2018.

[170] B. Heinrich, C. Burrowes, E. Montoya, B. Kardasz, E. Girt, Y.-Y. Song, Y. Sun, and M. Wu, "Spin pumping at the magnetic insulator (yig)/normal metal (au) interfaces," *Physical review letters*, vol. 107, no. 6, p. 066604, 2011.

[171] Q.-H. Yang, H.-W. Zhang, Q.-Y. Wen, and Y.-L. Liu, "Effects of off-stoichiometry and density on the magnetic and magneto-optical properties of yttrium iron garnet films by magnetron sputtering method," *Journal of Applied Physics*, vol. 108, no. 7, p. 073901, 2010.

[172] M. Mansour, M. Roumie, B. A. Samad, H. Basma, and M. Korek, "Rbs and xrd characterization of yttrium iron garnet thin films," in *Journal of Physics: Conference Series*, vol. 592, p. 012138, IOP Publishing, 2015.

[173] A. Mitra, O. Cespedes, Q. Ramasse, M. Ali, S. Marmion, M. Ward, R. Brydson, C. Kinane, J. Cooper, S. Langridge, *et al.*, "Interfacial origin of the magnetisation suppression of thin film yttrium iron garnet," *Scientific reports*, vol. 7, no. 1, pp. 1–8, 2017.

[174] M. Aldosary, J. Li, C. Tang, Y. Xu, J.-G. Zheng, K. N. Bozhilov, and J. Shi, "Platinum/yttrium iron garnet inverted structures for spin current transport," *Applied Physics Letters*, vol. 108, no. 24, p. 242401, 2016.

[175] S. Wolf, D. Awschalom, R. Buhrman, J. Daughton, v. S. von Molnár, M. Roukes, A. Y. Chtchelkanova, and D. Treger, "Spintronics: a spin-based electronics vision for the future," *science*, vol. 294, no. 5546, pp. 1488–1495, 2001.

[176] H. Ohno, M. D. Stiles, and B. Dieny, "Spintronics," *Proceedings of the IEEE. Institute of Electrical and Electronics Engineers*, vol. 104, no. 10, p. 1782, 2016.

[177] A. Brataas, "Insulating magnets control neighbor's conduction," *Physics*, vol. 6, p. 56, 2013.

[178] Y. Tserkovnyak, A. Brataas, G. E. Bauer, and B. I. Halperin, "Nonlocal magnetization dynamics in ferromagnetic heterostructures," *Reviews of Modern Physics*, vol. 77, no. 4, p. 1375, 2005.

[179] M. Weiler, M. Althammer, M. Schreier, J. Lotze, M. Pernpeintner, S. Meyer, H. Huebl, R. Gross, A. Kamra, J. Xiao, *et al.*, "Experimental test of the spin mixing interface conductivity concept," *Physical review letters*, vol. 111, no. 17, p. 176601, 2013.

[180] C. Hahn, G. De Loubens, O. Klein, M. Viret, V. V. Naletov, and J. B. Youssef, "Comparative measurements of inverse spin hall effects and magnetoresistance in yig/pt and yig/ta," *Physical Review B*, vol. 87, no. 17, p. 174417, 2013.

[181] N. Vlietstra, J. Shan, V. Castel, B. Van Wees, and J. B. Youssef, "Spin-hall magnetoresistance in platinum on yttrium iron garnet: Dependence on platinum thickness and in-plane/out-of-plane magnetization," *Physical Review B*, vol. 87, no. 18, p. 184421, 2013.

[182] N. Vlietstra, J. Shan, V. Castel, J. Ben Youssef, G. Bauer, and B. Van Wees, "Exchange magnetic field torques in yig/pt bilayers observed by the spin-hall magnetoresistance," *Applied Physics Letters*, vol. 103, no. 3, p. 032401, 2013.

[183] M. Althammer, S. Meyer, H. Nakayama, M. Schreier, S. Altmannshofer, M. Weiler, H. Huebl, S. Geprägs, M. Opel, R. Gross, *et al.*, "Quantitative study of the spin hall magnetoresistance in ferromagnetic insulator/normal metal hybrids," *Physical Review B*, vol. 87, no. 22, p. 224401, 2013.

[184] M. Isasa, A. Bedoya-Pinto, S. Vélez, F. Golmar, F. Sánchez, L. E. Hueso, J. Fontcuberta, and F. Casanova, "Spin hall magnetoresistance at pt/cofe2o4 interfaces and texture effects," *Applied Physics Letters*, vol. 105, no. 14, p. 142402, 2014.

[185] S. Meyer, M. Althammer, S. Geprägs, M. Opel, R. Gross, and S. T. Goennenwein, "Temperature dependent spin transport properties of platinum inferred from spin hall magnetoresistance measurements," *Applied Physics Letters*, vol. 104, no. 24, p. 242411, 2014.

[186] S. Marmion, M. Ali, M. McLaren, D. Williams, and B. Hickey, "Temperature dependence of spin hall magnetoresistance in thin yig/pt films," *Physical Review B*, vol. 89, no. 22, p. 220404, 2014.

[187] K.-i. Uchida, Z. Qiu, T. Kikkawa, R. Iguchi, and E. Saitoh, "Spin hall magnetoresistance at high temperatures," *Applied Physics Letters*, vol. 106, no. 5, p. 052405, 2015.

[188] S. Geprägs, A. Kehlberger, F. Della Coletta, Z. Qiu, E.-J. Guo, T. Schulz, C. Mix, S. Meyer, A. Kamra, M. Althammer, *et al.*, "Origin of the spin seebeck effect in compensated ferrimagnets," *Nature communications*, vol. 7, no. 1, pp. 1–6, 2016.

[189] M. Schreier, N. Roschewsky, E. Dobler, S. Meyer, H. Huebl, R. Gross, and S. T. Goennenwein, "Current heating induced spin seebeck effect," *Applied Physics Letters*, vol. 103, no. 24, p. 242404, 2013.

[190] J. Flipse, F. Dejene, D. Wagenaar, G. Bauer, J. B. Youssef, and B. Van Wees, "Observation of the spin peltier effect for magnetic insulators," *Physical review letters*, vol. 113, no. 2, p. 027601, 2014.

[191] E. Villamor, M. Isasa, S. Vélez, A. Bedoya-Pinto, P. Vavassori, L. E. Hueso, F. S. Bergeret, and F. Casanova, "Modulation of pure spin currents with a ferromagnetic insulator," *Physical Review B*, vol. 91, no. 2, p. 020403, 2015.

[192] F. Dejene, N. Vlietstra, D. Luc, X. Waintal, J. B. Youssef, and B. Van Wees, "Control of spin current by a magnetic yig substrate in nife/al nonlocal spin valves," *Physical Review B*, vol. 91, no. 10, p. 100404, 2015.

[193] L. Cornelissen, J. Liu, R. Duine, J. B. Youssef, and B. Van Wees, "Long-distance transport of magnon spin information in a magnetic insulator at room temperature," *Nature Physics*, vol. 11, no. 12, pp. 1022–1026, 2015.

[194] S. S.-L. Zhang and S. Zhang, "Magnon mediated electric current drag across a ferromagnetic insulator layer," *Physical review letters*, vol. 109, no. 9, p. 096603, 2012.

[195] S. S.-L. Zhang and S. Zhang, "Spin convertance at magnetic interfaces," *Physical Review B*, vol. 86, no. 21, p. 214424, 2012.

[196] S. A. Bender, R. A. Duine, and Y. Tserkovnyak, "Electronic pumping of quasiequilibrium bose-einstein-condensed magnons," *Physical review letters*, vol. 108, no. 24, p. 246601, 2012.

[197] S. T. Goennenwein, R. Schlitz, M. Pernpeintner, K. Ganzhorn, M. Althammer, R. Gross, and H. Huebl, "Non-local magnetoresistance in yig/pt nanostructures," *Applied Physics Letters*, vol. 107, no. 17, p. 172405, 2015.

[198] L. Cornelissen and B. Van Wees, "Magnetic field dependence of the magnon spin diffusion length in the magnetic insulator yttrium iron garnet," *Physical Review B*, vol. 93, no. 2, p. 020403, 2016.

[199] A. Hoffmann, "Spin hall effects in metals," *IEEE transactions on magnetics*, vol. 49, no. 10, pp. 5172–5193, 2013.

[200] H. Xiang, E. Kan, M.-H. Whangbo, C. Lee, S.-H. Wei, and X. Gong, "Single-ion anisotropy, dzyaloshinskii-moriya interaction, and negative magnetoresistance of the spin-1 2 pyrochlore r 2 v 2 o 7," *Physical Review B*, vol. 83, no. 17, p. 174402, 2011.

[201] A. Fert and O. Jaoul, "Left-right asymmetry in the scattering of electrons by magnetic impurities, and a hall effect," *Physical Review Letters*, vol. 28, no. 5, p. 303, 1972.

[202] Y. Lu, J. Cai, H. Pan, and L. Sun, "Ultrasensitive anomalous hall effect in sio2/fe-pt/sio2 sandwich structure films," *Applied Physics Letters*, vol. 100, no. 2, p. 022404, 2012.

[203] F. Wilhelm, P. Poulopoulos, G. Ceballos, H. Wende, K. Baberschke, P. Srivastava, D. Benea, H. Ebert, M. Angelakeris, N. Flevaris, *et al.*, "Layer-resolved magnetic moments in ni/pt multilayers," *Physical review letters*, vol. 85, no. 2, p. 413, 2000.

[204] J. Loram, R. White, and A. Grassie, "Spin-fluctuation effects in the resistivity of dilute pt fe alloys," *Physical Review B*, vol. 5, no. 9, p. 3659, 1972.

[205] S. Shimizu, K. S. Takahashi, T. Hatano, M. Kawasaki, Y. Tokura, and Y. Iwasa, "Electrically tunable anomalous hall effect in pt thin films," *Physical review letters*, vol. 111, no. 21, p. 216803, 2013.

[206] V. Volkov, V. Levashov, V. Matveev, and V. Berezin, "Peculiarities of the extraordinary hall effect of planar arrays fe nanoparticles embedded in an ultrathin pt film," *Applied Physics Letters*, vol. 91, no. 26, p. 262511, 2007.

[207] G. Swallow, G. Williams, A. Grassie, and J. Loram, "Magnetoresistance of a dilute ptfe alloy," *Journal of Physics F: Metal Physics*, vol. 1, no. 4, p. 511, 1971.

[208] S. Geprägs, S. Meyer, S. Altmannshofer, M. Opel, F. Wilhelm, A. Rogalev, R. Gross, and S. T. Goennenwein, "Investigation of induced pt magnetic polarization in pt/y3fe5o12 bilayers," *Applied Physics Letters*, vol. 101, no. 26, p. 262407, 2012.

[209] T. Kikkawa, M. Suzuki, J. Okabayashi, K.-i. Uchida, D. Kikuchi, Z. Qiu, and E. Saitoh, "Detection of induced paramagnetic moments in pt on y 3 fe 5 o 12 via x-ray magnetic circular dichroism," *Physical Review B*, vol. 95, no. 21, p. 214416, 2017.

[210] S.-Y. Huang, X. Fan, D. Qu, Y. Chen, W. Wang, J. Wu, T. Chen, J. Xiao, and C. Chien, "Transport magnetic proximity effects in platinum," *Physical review letters*, vol. 109, no. 10, p. 107204, 2012.

[211] W. Zhang, M. B. Jungfleisch, W. Jiang, Y. Liu, J. E. Pearson, S. G. Te Velthuis, A. Hoffmann, F. Freimuth, and Y. Mokrousov, "Reduced spin-hall effects from magnetic proximity," *Physical Review B*, vol. 91, no. 11, p. 115316, 2015.

[212] Y. Shiomi, T. Ohtani, S. Iguchi, T. Sasaki, Z. Qiu, H. Nakayama, K. Uchida, and E. Saitoh, "Interface-dependent magnetotransport properties for thin pt films on ferrimagnetic y3fe5o12," *Applied Physics Letters*, vol. 104, no. 24, p. 242406, 2014.

[213] T. Shang, Q. Zhan, L. Ma, H. Yang, Z. Zuo, Y. Xie, H. Li, L. Liu, B. Wang, Y. Wu, *et al.*, "Pure spin-hall magnetoresistance in rh/y 3 fe 5 o 12 hybrid," *Scientific reports*, vol. 5, no. 1, pp. 1–7, 2015.

[214] Y. Lu, Y. Choi, C. Ortega, X. Cheng, J. Cai, S. Huang, L. Sun, and C. Chien, "Pt magnetic polarization on y 3 fe 5 o 12 and magnetotransport characteristics," *Physical review letters*, vol. 110, no. 14, p. 147207, 2013.

[215] Y. Lu, J. Cai, S. Huang, D. Qu, B. Miao, and C. Chien, "Hybrid magnetoresistance in the proximity of a ferromagnet," *Physical Review B*, vol. 87, no. 22, p. 220409, 2013.

[216] S. Barnes and S. Maekawa, "Generalization of faraday's law to include nonconservative spin forces," *Physical review letters*, vol. 98, no. 24, p. 246601, 2007.

[217] X. Tao, Q. Liu, B. Miao, R. Yu, Z. Feng, L. Sun, B. You, J. Du, K. Chen, S. Zhang, *et al.*, "Self-consistent determination of spin hall angle and spin diffusion length in pt and pd: The role of the interface spin loss," *Science advances*, vol. 4, no. 6, p. eaat1670, 2018.

[218] K. D. Belashchenko, A. A. Kovalev, and M. van Schilfgaarde, "Theory of spin loss at metallic interfaces," *Physical review letters*, vol. 117, no. 20, p. 207204, 2016.

[219] Z. Qiu, K. Ando, K. Uchida, Y. Kajiwara, R. Takahashi, H. Nakayama, T. An, Y. Fujikawa, and E. Saitoh, "Spin mixing conductance at a well-controlled platinum/yttrium iron garnet interface," *Applied Physics Letters*, vol. 103, no. 9, p. 092404, 2013.

[220] Z. Qiu, D. Hou, K. Uchida, and E. Saitoh, "Influence of interface condition on spin-seebeck effects," *Journal of Physics D: Applied Physics*, vol. 48, no. 16, p. 164013, 2015.

[221] C. Burrowes, B. Heinrich, B. Kardasz, E. Montoya, E. Girt, Y. Sun, Y.-Y. Song, and M. Wu, "Enhanced spin pumping at yttrium iron garnet/au interfaces," *Applied Physics Letters*, vol. 100, no. 9, p. 092403, 2012.

[222] H. Chang, T. Liu, D. Reifsnyder Hickey, P. P. Janantha, K. A. Mkhoyan, and M. Wu, "Sputtering growth of y3fe5o12/pt bilayers and spin transfer at y3fe5o12/pt interfaces," *APL Materials*, vol. 5, no. 12, p. 126104, 2017.

[223] H. Wang, C. Du, P. C. Hammel, and F. Yang, "Spin transport in antiferromagnetic insulators mediated by magnetic correlations," *Physical Review B*, vol. 91, no. 22, p. 220410, 2015.

[224] H. Wang, C. Du, P. C. Hammel, and F. Yang, "Antiferromagnonic spin transport from y 3 fe 5 o 12 into nio," *Physical review letters*, vol. 113, no. 9, p. 097202, 2014.

[225] Y.-M. Hung, C. Hahn, H. Chang, M. Wu, H. Ohldag, and A. D. Kent, "Spin transport in antiferromagnetic nio and magnetoresistance in y3fe5o12/nio/pt structures," *AIP Advances*, vol. 7, no. 5, p. 055903, 2017.

[226] L. Jin, K. Jia, D. Zhang, B. Liu, H. Meng, X. Tang, Z. Zhong, and H. Zhang, "Effect of interfacial roughness spin scattering on the spin current transport in yig/nio/pt heterostructures," *ACS applied materials & interfaces*, vol. 11, no. 38, pp. 35458–35467, 2019.

[227] A. Prakash, J. Brangham, F. Yang, and J. P. Heremans, "Spin seebeck effect through antiferromagnetic nio," *Physical Review B*, vol. 94, no. 1, p. 014427, 2016.

[228] L. Baldrati, C. Schneider, T. Niizeki, R. Ramos, J. Cramer, A. Ross, E. Saitoh, and M. Kläui, "Spin transport in multilayer systems with fully epitaxial nio thin films," *Physical Review B*, vol. 98, no. 1, p. 014409, 2018.

[229] J. Holanda, D. Maior, O. Alves Santos, L. Vilela-Leão, J. Mendes, A. Azevedo, R. Rodríguez-Suárez, and S. Rezende, "Spin seebeck effect in the antiferromagnet nickel oxide at room temperature," *Applied Physics Letters*, vol. 111, no. 17, p. 172405, 2017.

[230] D. Kikuchi, M. Ishida, K. Uchida, Z. Qiu, T. Murakami, and E. Saitoh, "Enhancement of spin-seebeck effect by inserting ultra-thin fe70cu30 interlayer," *Applied Physics Letters*, vol. 106, no. 8, p. 082401, 2015.

[231] T. Tashiro, R. Takahashi, Y. Kajiwara, K. Ando, H. Nakayama, T. Yoshino, D. Kikuchi, and E. Saitoh, "Thickness dependence of spin pumping at yig/pt interface," in *Spintronics V*, vol. 8461, p. 846106, International Society for Optics and Photonics, 2012.

[232] D. Hou, Z. Qiu, K. Harii, Y. Kajiwara, K.-C. Uchida, Y. Fujikawa, H. Nakayama, T. Yoshino, T. An, K. Ando, *et al.*, "Interface induced inverse spin hall effect in bismuth/permalloy bilayer," *Applied Physics Letters*, vol. 101, no. 4, p. 042403, 2012.

[233] A. Brataas, Y. V. Nazarov, and G. E. Bauer, "Finite-element theory of transport in ferromagnet–normal metal systems," *Physical Review Letters*, vol. 84, no. 11, p. 2481, 2000.

[234] S. S.-L. Zhang and G. Vignale, "Nonlocal anomalous hall effect," *Physical review letters*, vol. 116, no. 13, p. 136601, 2016.

[235] Y. Yang, B. Wu, K. Yao, S. Shannigrahi, B. Zong, and Y. Wu, "Investigation of magnetic proximity effect in ta/yig bilayer hall bar structure," *Journal of Applied Physics*, vol. 115, no. 17, p. 17C509, 2014.

[236] T. Lin, C. Tang, and J. Shi, "Induced magneto-transport properties at palladium/yttrium iron garnet interface," *Applied Physics Letters*, vol. 103, no. 13, p. 132407, 2013.

[237] T. Lin, C. Tang, H. M. Alyahayaei, and J. Shi, "Experimental investigation of the nature of the magnetoresistance effects in pd-yig hybrid structures," *Physical review letters*, vol. 113, no. 3, p. 037203, 2014.

[238] V. L. Grigoryan, W. Guo, G. E. Bauer, J. Xiao, *et al.*, "Intrinsic magnetoresistance in metal films on ferromagnetic insulators," *Physical Review B*, vol. 90, no. 16, p. 161412, 2014.

[239] I. M. Miron, K. Garello, G. Gaudin, P.-J. Zermatten, M. V. Costache, S. Auffret, S. Bandiera, B. Rodmacq, A. Schuhl, and P. Gambardella, "Perpendicular switching of a single ferromagnetic layer induced by in-plane current injection," *Nature*, vol. 476, no. 7359, pp. 189–193, 2011.

[240] K. Garello, I. M. Miron, C. O. Avci, F. Freimuth, Y. Mokrousov, S. Blügel, S. Auffret, O. Boulle, G. Gaudin, and P. Gambardella, "Symmetry and magnitude of spin–orbit torques in ferromagnetic heterostructures," *Nature nanotechnology*, vol. 8, no. 8, pp. 587–593, 2013.

[241] G. Allen, S. Manipatruni, D. E. Nikonov, M. Doczy, and I. A. Young, "Experimental demonstration of the coexistence of spin hall and rashba effects in β-tantalum/ferromagnet bilayers," *Physical Review B*, vol. 91, no. 14, p. 144412, 2015.

[242] S. Huang, W. Wang, S. Lee, J. Kwo, and C. Chien, "Intrinsic spin-dependent thermal transport," *Physical review letters*, vol. 107, no. 21, p. 216604, 2011.

[243] B. Miao, S. Huang, D. Qu, and C. Chien, "Inverse spin hall effect in a ferromagnetic metal," *Physical review letters*, vol. 111, no. 6, p. 066602, 2013.

[244] H. Hoffmann and J. Vancea, "Critical assessment of thickness-dependent conductivity of thin metal films," *Thin Solid Films*, vol. 85, pp. 147–167, Nov 1981.

[245] C. R. Tellier, A. J. Tosser, and C. Boutrit, "The mayadas-shatzkes conduction model treated as a fuchs-sondheimer model," *Thin Solid Films*, vol. 44, pp. 201–208, Jul 1977.

[246] P. Wissmann and H. Finzel, *Electrical Resistivity of Thin Metal Films*. No. no. 223 in Electrical resistivity of thin metal films, Springer, 2007.

[247] K. Fuchs, "The conductivity of thin metallic films according to the electron theory of metals," *Math. Proc. Cambridge.*, vol. 34, pp. 100–108, Jan 1938.

[248] E. H. Sondheimer, "The mean free path of electrons in metals," *Adv. Phys.*, vol. 1, pp. 1–42, Jan 1952.

[249] C. R. Pichard, M. Bedda, V. I. Vatamanyuk, A. J. Tosser, and C. R. Tellier, "Alternative analytical forms of the fuchs-sondheimer function," *J. Mater. Sci.*, vol. 20, no. 11, p. 4185, 1985.

[250] J. Kondo, "Resistance minimum in dilute magnetic alloys," *Progr. Theor. Exp. Phys.*, vol. 32, pp. 37–49, Mar 1964.

[251] J. Kondo, "Effect of Ordinary Scattering on Exchange Scattering from Magnetic Impurity in Metals," *Phys. Rev.*, vol. 169, pp. 437–440, May 1968.

[252] V. Bogomolov, E. Kolla, and Y. Kumzerov, "One-dimensional effects in low-temperature conductivity of ultrathin metallic filaments," *Solid State Commun*, vol. 46, pp. 383 – 384, May 1983.

[253] B. Kramer and A. MacKinnon, "Localization: theory and experiment," *Rep. Prog. Phys.*, vol. 56, p. 1469, Dec 1993.

[254] B. Altshuler, D. Khmel'Nitzkii, A. Larkin, and P. Lee, "Magnetoresistance and hall effect in a disordered two-dimensional electron gas," *Physical Review B*, vol. 22, no. 11, p. 5142, 1980.

[255] S. Hikami, A. I. Larkin, and Y. Nagaoka, "Spin-orbit interaction and magnetoresistance in the two dimensional random system," *Progress of Theoretical Physics*, vol. 63, no. 2, pp. 707–710, 1980.

[256] F. D. Czeschka, L. Dreher, M. S. Brandt, M. Weiler, M. Althammer, I.-M. Imort, G. Reiss, A. Thomas, W. Schoch, W. Limmer, *et al.*, "Scaling behavior of the spin pumping effect in ferromagnet-platinum bilayers," *Physical review letters*, vol. 107, no. 4, p. 046601, 2011.

[257] S. Meyer, M. Althammer, S. Geprägs, M. Opel, R. Gross, and S. T. B. Goennenwein, "Temperature dependent spin transport properties of platinum inferred from spin Hall magnetoresistance measurements," *Appl. Phys. Lett.*, vol. 104, p. 242411, June 2014.

[258] Y. M. Lu, Y. Choi, C. M. Ortega, X. M. Cheng, J. W. Cai, S. Y. Huang, L. Sun, and C. L. Chien, "Pt magnetic polarization on yig and magnetotransport characteristics," *Phys. Rev. Lett.*, vol. 110, p. 147207, Apr 2013.